

Towards Anion Photoelectron Spectroscopy of Complexes and Clusters

I certify that the substance of this thesis has not previously been submitted for any degree or diploma and is not currently being submitted for any degree or diploma.

I certify that, to the best of my knowledge, any help received in preparing this thesis, and sources used, have been acknowledged in the thesis.

Robert LaMacchia, November 2008

Abstract

A Time of Flight Mass Spectrometer coupled with a Photoelectron Spectrometer has been constructed for anion photoelectron spectroscopy. An intimate understanding of the components and their purpose in experiment is presented. Various components in the apparatus have required both design and construction, and where appropriate the specific details are included. An ultra high vacuum level of 10^{-9} torr has been obtained inside the apparatus using two different pumping regimes, and they are also detailed. This vacuum is currently protected by a home-built safety system which monitors variables that the pumping apparatus depends on, and isolates the pumps from the chamber proper when an error is found. Preliminary results from recent testing are also provided, which suggest that the capability of the apparatus to determine an anionic mass spectrum is near optimum.

Gas phase anion complexes, consisting of hydrogen sulfide bonded to the halide anions fluoride and chloride have been explored by *ab initio* methods in order to predict their photoelectron spectra. These will be compared with experimental results when the apparatus is complete. Optimised geometries have been calculated for both the anion and neutral clusters in accompaniment with their fragments, permitting calculation of both electronic stabilisation energies as well as cluster formation enthalpies. The stability of the fluoride cluster in both anion and neutral form is found to be greater than that of the analogous chlorine system. For both halogens, the neutral is found to be considerably less stable than the corresponding anion. The optimised structures have served as the basis to construct portions of both cluster's multidimensional potential surfaces to be used for

future full photoelectron spectra predictions. Constructed three dimensional potential surfaces have been used to critique theory and basis set levels. For the fluorine cluster, both DFT and MP2 studies have effectively portrayed the influence of dimensional variation using a Dunning's double zeta basis set. The surfaces obtained for the chlorine cluster have suggested higher basis sets are required for a successful full analysis. Highly resolved one dimensional slices have also been constructed for four of the six possible dimensions in each cluster. Using the intermolecular stretching mode's potential energy slice, vibrational wavefunctions for both anion and neutral clusters of both fluorine and chlorine have been calculated. The neutral and anion wavefunctions have been compared to determine overlap, which in turn reflected the probability of transition from anion to neutral state upon photodetachment. Vibrational temperatures nominally accessed in supersonic expansions have been accounted for to reflect relative populations in the clusters, which allowed for thermal calibration of the transitions. For the fluoride cluster, the most intense detachment for both basis sets and levels of theory span $2 \leftarrow 0$ through to $4 \leftarrow 0$, with negligible transition from the anion's 'hotband' $v=1$. In the case of the chlorine, the hot band transitions spanning $6 \leftarrow 1$ through $8 \leftarrow 1$ have been found most intense for the MP2 level of theory using both basis sets.

Acknowledgements

As with any undertaking of this magnitude there are always many people to thank:

First and foremost I must thank my supervisor Dr. Duncan Wild. He has motivated, encouraged, befriended and bantered with me all year; I have enjoyed every moment.

To the workshop staff: Nigel Hamilton, Andrew Sawyer, Damien Bainbridge and Trevor Franklin. You have all been uniquely helpful throughout the construction of the TOF-PES; working at an unparalleled efficiency with forever helpful ideas and intuitions.

Many thanks are extended to A/Profs Graham Chandler and Dylan Jayatilaka: your fruitful discussions and answers to my questions have motivated me no end. I am indebted to you for helping me grasp the conceptually trying field of theoretical chemistry.

I must collectively thank the Wild, McKinley and Saunders groups for their companionship and formatting wisdom throughout the late nights.

To my family: Thank you for your understanding and words of comfort and concern. My brother Frank, I thank for trying to teach me not to make the same mistakes as you, but helping me nonetheless when I inevitably did.

And last I thank Nicole – my motivator extraordinaire. Without your support I wouldn't have even got close.

Table of Contents

1	Introduction and Theory	1
1.1	Introduction	1
1.2	Potential Energy Surfaces	3
1.3	The Solvation Experiments	5
1.3.1	Solute-Solvent Interactions	5
1.3.2	e ⁻ Solvation	9
1.4	Dipole Bound Anions	10
1.5	Metallic Systems	12
1.5.1	Metals and Metal-Oxides	12
1.5.2	Novel Clusters	14
1.6	Multiply Charged Anions (MCAs)	15
1.7	Gas Phase Halide Solvation	18
2	The TOF-PES	23
2.1	General Considerations	24
2.1.1	Vacuum System	24
2.1.2	Safety System Programming	29
2.2	Gas Mixing Station	32
2.3	The Source Chamber	33
2.4	Extraction Chamber	36
2.5	Beam Focusing and Detection Schemes	38
2.6	Laser	41
2.7	Pulsing Methods	41
2.8	Detectors	44
2.9	The Construction	47
2.10	Net Progress	51
3	<i>ab Initio</i> Calculations	52
3.1	Computational Methods	52
3.2	Cluster Geometries, NBO analyses and Energies	60
3.2.1	FH...SH	60
3.2.2	Cl...HSH	65
3.3	Four Dimensional Potential Energy Scans	66
3.3.1	FH...SH	66
3.3.2	Cl...HSH	70
3.4	One Dimensional Potential Energy Slices	72
3.4.1	FH...SH	72
3.4.2	Cl...HSH	75
3.5	Predicted Spectra	77
3.5.1	FH...SH	77
3.5.2	Cl...HSH	82
4	Conclusions and Future Work	87
5	Appendix	88
5.1	Anion Photoelectron Data Tables	88
5.2	TOF-PES Safety System	91

5.3	UNIX dataextraction.sh Script.....	99
6	References:	100

List of Tables and Figures

Figure 1– Sample surfaces detailing potential energy dependence on example variable R.	4
Figure 2 – The stabilisation energy plateaus with the number of solvent molecules.	6
Figure 3 – Potential energy surface detailing electron affinities and dissociation energies of a solvated anion and neutral.	7
Figure 4 – Three possible forms of ionisation: a) ionisation of a cation, b) a neutral and c) an anion from ref. 56	16
Figure 5 – Adapted from ref. 56: potential energy vs. R (cluster – excess charge distance) for the photoionisation and photodetachment processes.	17
Figure 6- Schematic of Wild lab TOF-PES	24
Figure 7 - Flow diagram showing the safety system which monitors the TOF-PES	31
Figure 8– Schematic of pulsed nozzle	34
Figure 9 - Time of flight plates and X-Y deflection plates electrically isolated via ceramic tubes.	37
Figure 10- Einzel lens stack from side and front profile. Note the three segments and ceramic posts to electrically isolate assembly	39
Figure 11 – Qualitative description of the pulsing scheme employed in the TOF-PES to manipulate and analyse mass selected clusters	43
Figure 12 – Side and front view of ion detector mounted to a vertical adjustment stage. All units given are in mm.	45
Figure 13 -Front and side view of photoelectron detector on 8’’ blank flange. Units are in mm unless otherwise stated	45
Figure 14 – Voltage divider set up for the microchannel plate detectors	47
Figure 15 – Schematic of apparatus scaffolding. Darker print indicates Dexion, with fairer print showing chamber flanges and positioning	48
Figure 16 – Before and after comparison of internal component of ‘Diffstak’ diffusion Pump	49
Figure 17 – Einzel lens chamber correction scheme.	50
Figure 18 – Mass spectrum obtained for methyl iodide with argon buffering gas	51
Figure 19 – Optimised geometries of clusters under study: a) fluorine and b)	55

chlorine with five of the six variables c) and d) that affect the potential energy. Dihedral angle not shown for clarity	
Figure 20 – a) neutral compared to b) anion potential surface for the intermolecular distance versus dihedral angle of FH...SH at the MP2/pVTZ level of theory	68
Figure 21 – Improvement in potential surface achieved in going from using the a) pVDZ basis set to b) pVTZ for the FH...SH system	69
Figure 22 – Comparing the quality of neutral Cl...HSH potential surfaces produced from a) cc-pVTZ and b) cc-pVDZ basis sets	71
Figure 23 – One dimensional slices of the FH...SH ⁻ hypersurface illustrating a) aHFS and b) aFSH effects	73
Figure 24 – Dihedral angle affects the energy of the FH...SH system less in the a) anion as opposed to b) neutral	74
Figure 25 – One dimensional slices of the ClH...SH hypersurface illustrating a) aHSCI and b) aSCIH effects	76
Figure 26 – One dimensional potential energy slices for FH...SH system at MP2/pVTZ level of theory, with vibrational wavefunctions in the inset	79
Figure 27 – One dimensional potential energy slices for the FH...SH cluster at the MP2/pVTZ level of theory	80
Figure 28 – Predicted photoelectron system for FH...SH using a) pVTZ and b) pVDZ basis sets	81
Figure 29 – One dimensional potential energy slices for Cl...HSH system at MP2/pVTZ level of theory, with vibrational wavefunctions in the inset	84
Figure 30 – One dimensional potential energy slices for the Cl...HSH cluster at the MP2/pVTZ level of theory	85
Figure 31 – Predicted photoelectron system for Cl...HSH using a) pVDZ and b) pVTZ basis sets	86
Table 1 – Geometry and energetic data of clusters and their fragments	62
Table 2 – NBO analyses quantifying hydrogen bond formation	63
Table 3 – Spectral data to be experimentally verified	64
Table A1: Solvation clusters studied using anion photoelectron spectroscopy	88
Table A2 – Select examples of dipole bound anions	89

Table A3 – Anionic metal and semiconductor clusters studied using anion photoelectron spectroscopy	89
--	----

1 Introduction and Theory

1.1 Introduction

A complete knowledge of how chemical reactions and processes take place remains a fundamental goal central to the study of chemistry. It is interesting to note that while technologies aim to exploit matter to its fullest capacity, there remain fundamental curiosities concerned with how such processes and properties come to pass. To investigate such questions at their root, it is paramount that the most simple and small scale processes be well understood. Spectroscopy, as a generic tool, offers various methods and tools to explore these understandings. A spectroscopic technique that specifically probes the intermolecular interaction is anion photoelectron spectroscopy of complexes and clusters. It has been the central goal of this project to construct a Time of Flight Mass Spectrometer coupled to a Photoelectron Spectrometer (TOF-PES) to be used for such spectroscopy.

The particular benefit of photoelectron spectroscopy is that it probes the neutral complex or cluster's potential energy surface at a region predetermined by the geometry of the anion.¹ As will be shown in sections 1.3-1.7 this feature can make photoelectron spectroscopy particularly useful in modern materials research and improving the understanding of the intermediary phase between gaseous and condensed states of matter. Regarding this latter topic, the hydration of simple anions proves to be fascinating due to the balance of ion-solvent electrostatic interactions versus solvent-solvent interactions at play.² While there is a considerable body of work using various spectroscopic techniques

on the halide-water complex $[X^{\cdot-}\dots H_2O]$ and clusters $[X^{\cdot-}\dots (H_2O)_n]$, relatively little is known about the analogous halide-hydrogen sulfide systems $[X^{\cdot-}\dots (H_2S)_n]$. A key motivation therefore behind this thesis has been the completion of *ab initio* calculations in order to predict results to be obtained from the instrument in future work. This complex also serves as an ideal probe of the potential surface for the elementary reaction:



in much the same way that recent work on particular ‘benchmark reactions’ have been performed.³

Considering that this project has two foci, this introduction offers two main components. The first component deals largely with the theory behind the experiments at play, as well as how the apparatus functions and acquires photoelectron spectra. These basic understandings shall then be built upon by presenting some different varieties of anion photoelectron spectroscopy which can be achieved by using slight variants on machine set up, accompanied by their unique capabilities. Considering that the apparatus constructed for this project is in its infancy, this shall act as a worthwhile means of presenting possible experimental directions which may be realised in future work.

The second component of this introduction focuses on the microsolvation of halide anions as well as the theoretical considerations required to predict photoelectron spectra of such complexes. The motivation behind the choice of the cluster considered is to compare the solvation of the halides by water and hydrogen sulfide and thereby explore differences observed for the second row hydrides.

1.2 *Potential Energy Surfaces*

In order to appreciate the types of experiments performed and the results obtained from them, it must be realised that the photoelectrons detected are derived from discrete levels on a multidimensional potential energy surface, unique to the cluster being probed. A cluster here is defined as two, or more, non-bonded species interacting in some way. Factors such as bond lengths, bond angles and intermolecular distances are all independently important in determining the exact nature of the potential surface, which of course reflects the interactions at play. For n such variables in a particular system there exists an n -dimensional potential energy surface. On this surface, there can be minima and maxima corresponding to the most and least energetically favourable states that the cluster in question can occupy. Owing to the fact that nuclei can vibrate and molecules can rotate, within this potential energy surface there are a multitude of discrete rotational and vibrational states which a particular cluster can occupy depending on the energy of the system.⁴ A one-dimensional slice of a possible potential surface is given in Figure 1. With this understanding that chemical species exist within discrete states on a potential energy surface, the process of photodetachment from anion to a neutral cluster can be envisioned as the transition from the lower energy anion's surface to that of the neutral. The energy afforded by the laser launches the cluster onto the neutral surface. The difference in energy between the neutral and anion at the geometry of the anion is known as the vertical detachment energy (VDE). This VDE does not necessarily correspond to a discrete level on the neutral's potential energy surface. The difference between the laser energy and the neutral vibrational energy levels accessed is transferred to the photodetached electron as kinetic energy (e^-KE):

$$e^-BE = h\nu - e^-KE \quad (1)$$

This electron binding energy is the same as the difference in energy between the neutral state accessed and the energy level of the anion from which photodetachment took place.

$$e^-BE = E(n) - E(a) \quad (2)$$

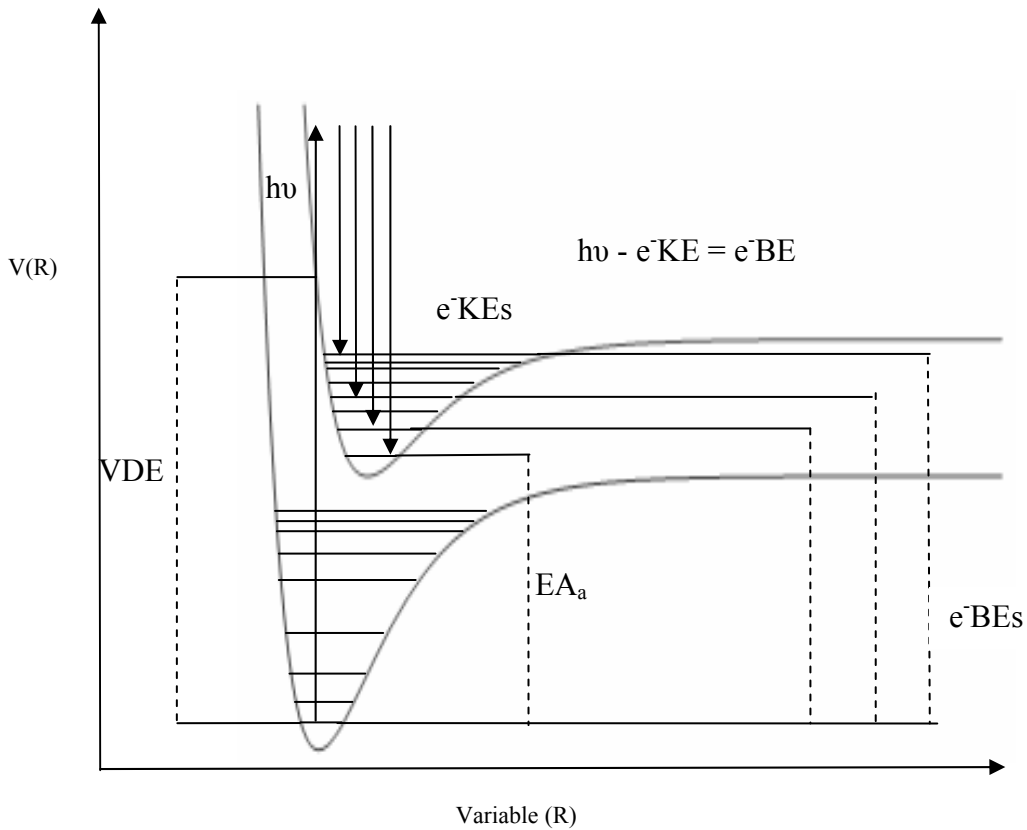


Figure 1– Sample surfaces detailing potential energy dependence on example variable R. Constant energy regions signify discrete vibrational energy levels. The lower surface is the anion, and the higher corresponds to the neutral

Equation (1) however offers this value in terms of experimental observables. The electron's kinetic energy is measured by determining the time taken for the photodetached electrons to traverse a flight tube of known distance. Using the known mass of an electron, the classical equation for kinetic energy can be applied:

$$E_{KE} = \frac{1}{2} m_e \left(\frac{s}{t} \right)^2 \quad (3)$$

The energy difference between both clusters in their lowest vibrational state is known as the adiabatic electron affinity (EA_a), and can equal the aforementioned electron binding energy if the optimised geometry of the anion and neutral do not vary considerably. This is because the factor that determines the neutral state occupied in photodetachment is vibrational wavefunction overlap.¹

1.3 The Solvation Experiments

1.3.1 Solute-Solvent Interactions

The application of anion photoelectron spectroscopy towards solvation was realised by virtue of the capability to selectively photoeject an electron from a specific cluster. For a given anion, the number of solvent molecules can be systematically increased and the energy change in the system monitored through the photoelectron spectra obtained. Its use in understanding solvation processes in anion clusters, initially depended on the comparable information afforded from thermochemical experiments such as high-pressure mass spectrometry,⁵⁻¹² flow tube measurements,¹³ ion cyclotron resonance spectrometry¹⁴ and tandem mass spectrometry.¹⁵ These experiments aimed to find equilibrium constants as a function of temperature for the rudimentary association reaction:



With the aid of van't Hoff plots, the enthalpy and entropy changes $\Delta H_{n,n+1}^\circ$ $\Delta S_{n,n+1}^\circ$ could also be calculated. The dissociation energy for $n+1 \rightarrow n$ solvent molecules is approximated by $-\Delta H_{n,n+1}^\circ = D[A^-(B)_n \dots B]$ with some empirically derived small correction in equating energy with enthalpy.¹⁶ In performing such experiments, the details of the ion-neutral interaction are observed by comparing the strength of interaction for clusters with differing molecular structure and size, degrees of hydrogen bonding, polarisability, dipole moments, etc. When the size of the cluster is varied by altering the number of solvent molecules interacting with a particular anion, the solvation shell can be defined. For some particular number of solvent molecules, a cluster's dissociation energy becomes particularly large, indicating unusual stability. Furthermore, as extra solvent molecules are added, the dissociation energy does not increase appreciably (i.e. it

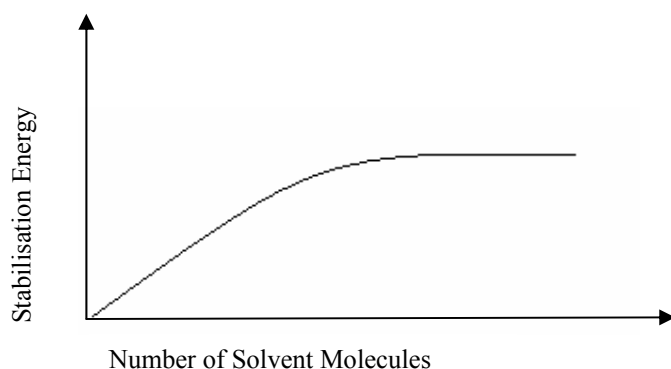


Figure 2 – The stabilisation energy plateaus with the number of solvent molecules. For example, see ref. 27 for $O^-(Rg)_n$

plateaus; see Figure 2) indicating a closed shell has formed and that the extra stabilisation imparted by further solvent molecules is hindered on account of the shielding this shell provides.

Photoelectron spectroscopy probes the ion-neutral interaction of solvated anions by virtue of their adiabatic electron affinities. For any negative cluster ion $A^-(B)_n$ and its corresponding neutral, $A(B)_n$, the following relationship holds:¹⁶

$$EA_a[A(B)_n] = EA_a[A] + \sum_{m=0}^{n-1} D[A^-(B)_m \dots B] - \sum_{m=0}^{n-1} D[A(B)_m \dots B] \quad (4)$$

Yet this can be more specifically applied to results realisable from anion photoelectron spectroscopy, as Figure 3 shows (for a *single* solvent molecule).

$$EA_a[A(B)_n] = EA_a[A(B)_{n-1}] + D[A^-(B)_{n-1} \dots B] - D[A(B)_{n-1} \dots B] \quad (5)$$

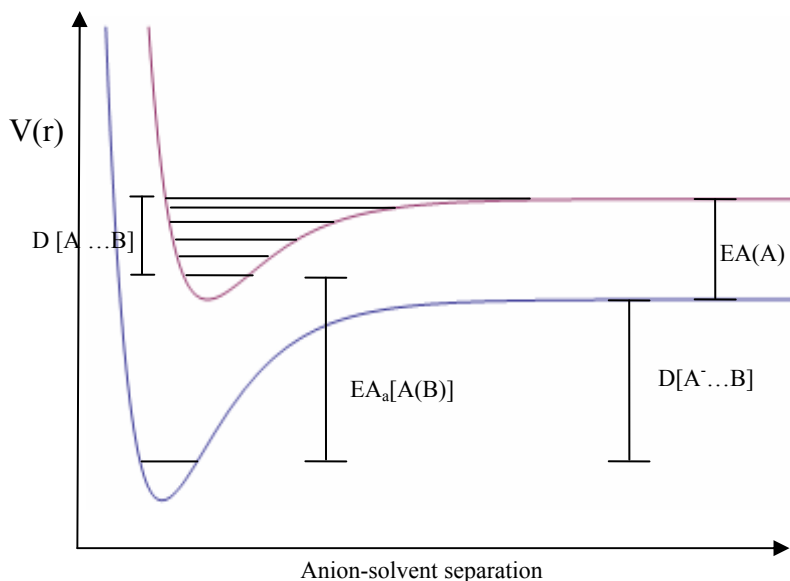


Figure 3 – Potential energy surface detailing electron affinities and dissociation energies of a solvated anion and a neutral species.

Where EA_a refers to the adiabatic electron affinity and D signifies the dissociation energy. The dissociation energy for the neutral is generally much smaller than the dissociation energy of the anion, and the following approximation can safely be made:¹⁷

$$D[A^-(B)_{n-1}\dots B] \approx EA_a[A(B)_n] - EA_a[A(B)_{n-1}] \quad (6)$$

Thus by mass selecting clusters in a stepwise fashion, the adiabatic electron affinity can be determined, which is then used to calculate both the absolute solvation energy as well as the energy imparted by each solvent molecule added. These methods were confirmed when anion photoelectron spectroscopy was applied to $H(NH_3)$, and the dissociation energy was found to be 0.36 eV.¹⁸ This value agreed with theoretical predictions, which had become the more prevalent method to compare against (i.e. as opposed to thermochemical data which is experimentally more difficult to obtain). To determine the species being solvated a useful method is to compare the obtained photoelectron spectrum with the respective naked ions, and the one which resembles a sub-ion of the cluster's spectrum is taken as the species on which the charge is localised. The signal will of course shift to higher electron binding energy due to solvation stabilisation. This shift may also be accompanied by vibrational features, signifying the amount of structural distortion the solvent has undergone. Having successfully realised these relationships, the field of photoelectron spectroscopy has grown with studies of numerous solvent-solute systems as Table A1 illustrates.

Solvent shells tend to occur largely when the number of solvent molecules is twelve, owing to the close packing icosahedral structure the solvent molecules form with the solute (or anion) at the centre. A peculiar result worth noting is that of $I(H_2O)_n$ where the first solvent shell contains six water molecules with the iodide residing on its surface. Rather than encapsulate the heavy halide into a cavity, the lowest energy structure

requires a network of hydrogen bonds acting as a single entity interacting with the iodide ion. Evidently, this property has proven to be characteristic of highly polar solvents,¹⁹ which has led to curiosity regarding solvated electrons, as discussed in the subsequent section. Scientific investigation into the hydrated clusters is expanded upon in section 1.7 due to its direct relevance to the cluster class under study in this work.

1.3.2 e⁻ Solvation

Many closed-shell, polar solvents do not accept electrons to form stable anions in the gas phase.¹⁶ Yet in the condensed phase, solvated electrons form readily – clearly, the many-body interactions between such polar molecules in the condensed phase are necessary to attach an excess electron. Anion photoelectron spectroscopy studies were conducted on the polar solvent ions that were found to exist in the gas phase, two of note are: (H₂O)_n⁻ where n = 2, 6, 7, 10 and all n > 10;²⁰ (NH₃)_n⁻ where onset occurs at n = 36 (41 for ND₃)²¹. In exploring the photoelectron spectra of these clusters, a relationship useful when comparing to the bulk state is¹⁹

$$VDE(n) = VDE(\infty) - \frac{e^2}{2R_s \left(1 + \frac{1}{D_{op}} - \frac{1}{D_s}\right) n^{\frac{1}{3}}} \quad (7)$$

Where R_s is the effective radius of a single solvent molecule; D_s is the static dielectric constant of the medium; D_{op} is the optical dielectric constant and VDE is the vertical detachment energy. Using this equation, the experimental detachment energies for the clusters can then be plotted against n^{-1/3} and the nature of the fit could be explored. For ammonia, only one set was observed; a set which shifted to higher binding energy with

cluster size as expected, which extrapolated to an intercept close to the known value of the vertical detachment energy of ammoniated electrons in the condensed phase.¹⁶ For water though, three distinct types of spectra were found as proven by three different linear fits to the aforementioned equation. For $n=2$, the spectrum was dominated by a low electron binding energy. The spectra of $n=6$ and 7 gave several relatively low electron binding energy peaks, and from $n=11$ to greater values, the spectra gave single broadened peaks that shift higher as n increased. The data does extrapolate to a value near the known photoemission threshold energy, but this is only when the data for $n > 10$ is taken, suggesting that clusters of this type assimilate the bulk hydrated electron, whilst those smaller species represent a different class of ion – the dipole bound anion (see section 1.4). Thus, it can be seen that the links being drawn between the bulk and both the molecular and cluster scale are not completely linear or straightforward. There are subtleties in this intermediary phase which require addressing. It is interesting to note that the results as stated above are not to be taken as dogma. Recent experiments have shown the limit for this transferral from dipole bound, to embryonic bulk are subject to change depending on experimental conditions.^{20,22} Considering the prolific advent of popularised ‘nanotechnologies’ to modern times, which in essence builds from cluster science, the scientific understanding at this scale must be refined and assured, so that the relationship between the macro-scale and nano- and cluster- scales can be better understood.

1.4 Dipole Bound Anions

As mentioned in the preceding section, anion photoelectron spectroscopy stumbled upon a new breed of ion. The initial discovery of CH_3CN^- ,²³ experimentally contradicting

theoretical results, followed by the subsequent discovery of the water dimer anion (whilst the monomer did not exist)²⁴⁻²⁶ contributed to the realisation that a threshold dipole moment needs to exist for the monomer of certain anions to form. The water monomer's was obviously too low, whilst the dimer has $\mu = 2.6 \text{ D}$ – a threshold of $\approx 2.5 \text{ D}$ has been loosely defined.²⁷ A key feature worth noting for these types of anions is that they exhibit very low, singular electron binding energies, signifying that the state is not particularly stable, and that the geometry between the anion and neutral is virtually unchanged. The electron is thought to attach by virtue of a weak electrostatic attraction to the positive 'pole' of a cluster in question, and because of this, it is clear that the binding energy should not be great. If the cluster possesses a large charge gradient, or a well pronounced electronegativity difference throughout a cluster, then there exists a significantly low electron density region whereby an excess electron can exist so as to stabilise the imbalance. Furthermore, this extremely diffuse electron lacks any distinct orbital character and is implicated to be the reason for negligible geometry change between the anion and neutral. Rather than completing or even occupying a valence shell in a molecular orbital as convention dictates, the dipole-bound model reports the excess electron as loosely associating to the molecular framework on account of a very weak electrostatic attraction. Table A2 lists a select number of dipole anions experimentally probed.²⁸ The discovery of the dipole bound anion has not only described a new type of charged species, it has also allowed for the development of computational models, in that its existence has ensured theoretical models accordingly consider the dipole moment of the complex or cluster in question when determining anionic states. Furthermore, the ability of low energy radiation to produce such anions has been applied to a biological

context. Due to the large dipoles associated with biologically relevant molecules, namely nucleobases in DNA, recent research has been focused on the interaction of low energy radiation with different nucleobases to determine any alterations in structure which may occur. In this way, the mechanisms by which low energy radiation disrupts the hydrogen bonding networks of DNA can be better understood.²⁹⁻³⁸

1.5 Metallic Systems

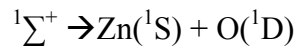
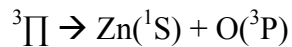
1.5.1 Metals and Metal-Oxides

Since its inception, anion photoelectron spectroscopy has been utilised to probe the electronic structure and transitions associated with the anion-neutral metallic systems. The only difference in apparatus to the gas phase experiments reported is in the source chamber where clusters are generated. As metal containing species are generally difficult to obtain as stable species in the gas phase, a suitable alternative was soon realised in laser ablation of a solid sample.¹⁶ The analysis of metallic species has largely dominated anion photoelectron spectroscopy's niche in the literature since this advance. The ease with which electronic assignments can be made for simple cluster systems has allowed for a full body of knowledge to be built. A sample of some of the systems explored to date is given in Table A3. To give but one example of the utility of photoelectron spectroscopy in resolving anomalous results, the ZnO³⁹ system is detailed. Zinc oxide has a closed d shell and therefore bonds primarily through its 4s and 4p orbitals, making it analogous to the alkaline earth metals with term symbol $1\Sigma^+$.^{40,41} The destination of the added electron is an antibonding orbital, which suggests that the dissociation energy of

the anion should be less than the neutral. Photoelectron studies have revealed the adiabatic electron affinity of zinc oxide, which, in conjunction with the literature values for the dissociation energy of neutral zinc oxide and the electron affinity of oxygen⁴²⁻⁴⁶ was used to determine the dissociation energy of the anion (2.24 eV) by the relationship analogous to that given in 1.3.1:

$$EA_a(\text{ZnO}) - EA(\text{O}) = D_0(\text{ZnO}^-) - D_0(\text{ZnO}) \quad (8)$$

This is odd though because it suggests that the dissociation energy of the anion is greater than that of the neutral, whilst intuition and computational studies suggest the vibrational frequencies of the anion are lower than the neutral's, and that the length of the zinc oxide bond in the anion is greater than in the neutral.³⁹ This anomaly was resolved through realisation that like the alkaline earth oxides, zinc oxide has a $^3\Pi$ first excited state, which is a mere 0.26 eV above the neutral's $^1\Sigma^+$ state. By considering the dissociation reactions of these two states and the atomic states to which they dissociate it was suggested that the value for the dissociation energy of the neutral zinc oxide, was most likely that of the ground state, $^1\Sigma^+$, to the $\text{Zn}(^1\text{S}) + \text{O}(^3\text{P})$ asymptote.



(Where the $\text{Zn}(^1\text{S}) + \text{O}(^1\text{D})$ state is 1.97 eV greater than the $\text{Zn}(^1\text{S}) + \text{O}(^3\text{P})$ asymptote)

By adding 1.97 eV to the quoted value, the dissociation energy to the $\text{O}(^1\text{D})$ state becomes 3.58 eV which is greater than that of the anion. Thus, the inequality becomes $D_0(\text{ZnO}^-) < D_0(\text{ZnO})$ which agrees with the other experimental results obtained from the photodetachment studies.

1.5.2 Novel Clusters

Theoretical chemists can suggest target clusters or supermolecules through energetic calculations which explore thermodynamic and electronic stabilities. Photoelectron spectroscopy can confirm or reject such conjectures, and if confirmation is achieved, then it may be worthwhile to attempt wide scale synthesis. This type of approach in accordance with earlier experiments on solvent systems, has led to the development of what are now considered magic number clusters.⁴⁷ The term stems from the unusual stability imparted on a cluster with some ‘magical’ number of solvent or clustering molecules. Whilst the digit may vary depending on the atom under investigation and its particular shell formation mechanism, twelve is a recurring digit in these studies, because it yields the geometrically stable icosahedron.⁴⁸ In the case of some clusters, it also corresponds to a closed valence shell. A recent example is that of Al_{13}^- , a 40 electron closed shell species⁴⁹ in which an aluminium central atom is the core of an icosahedron.⁵⁰ Its unusual stability is made clear by its inertness. As an example, consider etching experiments performed where aluminium anion clusters were attacked by oxygen leaving only one intact cluster: Al_{13}^- .⁵¹ The adiabatic electron affinity has been measured and is 3.6 eV,⁵² in many ways making it similar to a halide anion. This analogy has prompted research into its ionic bonding capabilities with the group I metals to form larger ionic frameworks.⁴⁸ This has been shown to be the case for CsAl_{13} by mass spectral and photoionisation experiments⁵³ and more recently for KAl_{13} ⁴⁸ and LiAl_{13} ⁵⁴ using photodetachment of the anion. Other studies have also explored copper doped magic aluminium clusters, e.g. CuAl_{13} , finding the copper to exchange for the aluminium in the centre of the icosahedral framework.⁴⁷ This exciting research topic can be seen as a clear

step towards the formation of nanoscale materials assembled out of magic number clusters.

1.6 Multiply Charged Anions (MCAs)

Recent apparatus development by Wang⁵⁵ has allowed for the production and analysis of MCAs through a novel alteration of the source chamber. The difficulty associated with generating doubly charged anions can be understood when considering the potential energy as a function of the distance between the monovalent anion and the second electron. Consider first when a cation and electron are in a close environment (analogous to a neutral molecule ionisation), the interaction is completely attractive owing to the electrostatics of opposite charges. The interaction between a neutral and electron (analogous to a conventional photodetachment experiment) is not as attractive, but is not repulsive. The final scenario is analogous to a second ionisation, but the two species are both negative and obviously repel. Thus, it can be seen that there exists a significant Coulombic barrier for the generation of a divalent anion. These three cases are illustrated in Figure 4.

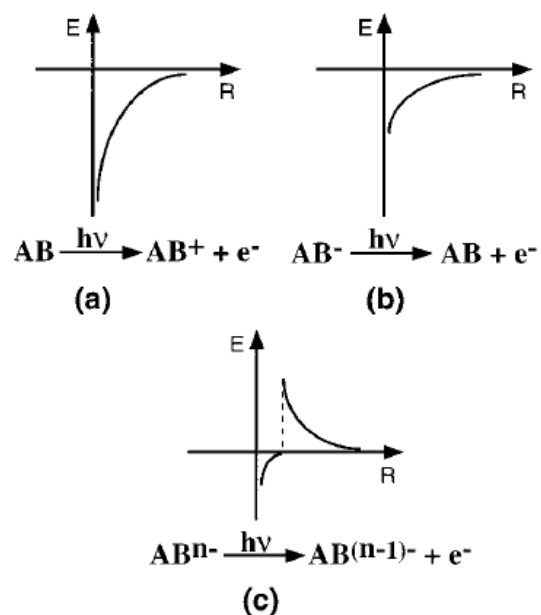
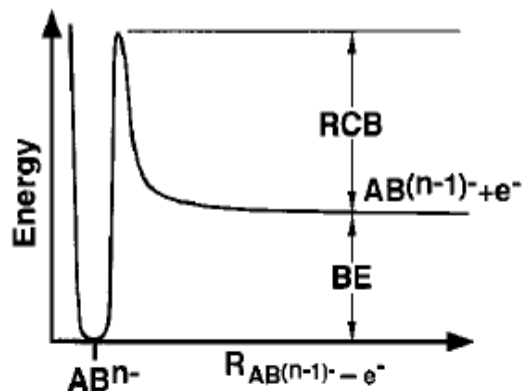
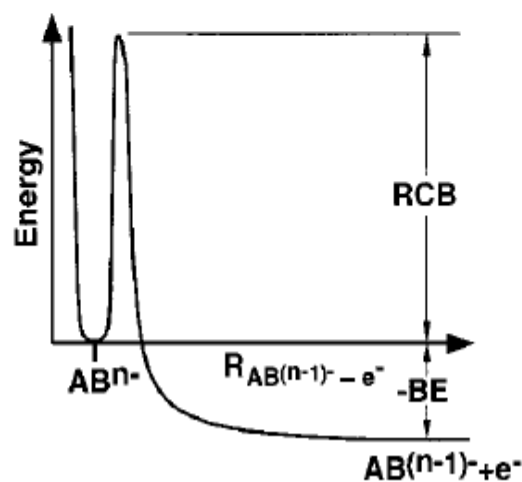


Figure 4 – Three possible forms of ionisation: a) ionisation of a cation, b) a neutral and c) an anion (from ref. 56)

This repulsive coulomb barrier (RCB) of Figure 4c makes for some interesting results when the divalent photodetachment is performed. It must be re-enforced here that equation (1), which is paramount to all of anion photoelectron spectroscopy cannot be violated.



(a)



(b)

Figure 5 – Adapted from ref. 56: Potential energy vs. R (cluster – excess charge distance) for the photoionisation and photodetachment processes. See in text

There are two scenarios worthy of mention in Figure 5. In the first instance (a), it can be seen that if a divalent anion can be generated and irradiated with light corresponding to its binding energy, it will not photodetach due to the RCB. What is interesting is that once the RCB+BE threshold energy has been reached, the kinetic energy will not reflect a near-threshold detachment. As the diagram shows, the energy is stored within the MCA until it reaches the maximum of the RCB, at which point it releases this potential energy as kinetic, and Einstein's law is not violated. Most fascinating is the second example

where the monovalent anion is actually more stable than the divalent, but the MCA can exist as a meta-stable state on account of the RCB preventing its escape. If the system is irradiated with an amount of energy equal or greater than the RCB, the kinetic energy of the electron will be greater than the incoming laser energy because of Equation 1. Both the repulsive coulomb barrier and negative binding energies have been experimentally determined by the Wang group.⁵⁷

The method used to produce the MCA's in the gas phase is not overly complex. The source chamber contains a syringe needle charged at a high negative voltage, so that when the solution phase species is sprayed into the system, it is highly energised and travels further through the machine than any neutrals or cations. These liquid droplets have the solvent evaporated off by virtue of traversing a heated capillary tube, leaving only the intended MCAs.⁵⁶ The obvious limitation in this technique is that only anions readily available in the solution phase can be investigated.

1.7 Gas Phase Halide Solvation

The cluster class to be probed in this work by *ab initio* methods are the halide hydrogen sulfide complexes: $[X\dots H_2S]^-$ where $X = Cl$ and F . Previous work has been undertaken on the analogous $[X\dots (H_2O)_n]^-$ clusters, utilising both Infrared (IR) and photoelectron spectroscopies (PES).⁵⁷ Recent work exploring the structure and IR spectra of the analogue $[X\dots (H_2S)_n]^-$ ($X = F$, $n = 1-6$; Cl and Br , $n = 1-4$)^{58,59} has recently been performed and is the key motivation for the work performed herein.

The investigation of the halogens solvated in the gas phase gives a molecular understanding of how anionic solute molecules interact with their surrounding solvent environment. The molecular understanding acts as a basis for all the data and information available regarding the bulk phase properties. However, there have been various difficulties associated with determining structures, energetics and interaction properties of these clusters. This difficulty stems from the energetic similarity between the anionic hydrogen bond and the hydrogen bonding network of water.⁶⁰ Initial experimental studies focussed on determining the onset of solvation shell closure by searching for peaks in the cluster ion distribution using high pressure mass spectrometry.⁶¹ The smoothness of these distributions, combined with theoretical predictions of two possible solvation modes for different halides:⁶² (internal and surface bound), shifted the focus of these experiments.

The question was posed as to whether the anion bonds at the surface of a hydrogen bound water cluster, or forms ionic hydrogen bonds with non-interacting solvating molecules. One of the earliest methods to answer this question was through anion photoelectron spectroscopy of the halide water clusters. It was thought that by investigating the electronic stabilisation energy of the clusters in a stepwise manner, a large difference in vertical detachment energy would be found for the increase of one solute molecule. However, the results did not achieve this due to the temperature variability from cluster to cluster allowing for a smooth progression of VDE as cluster size increased. This experimental anomaly revealed perhaps the most significant challenge – the need for cold

clusters. Irrespective of the global minimum for these clusters, if the temperature is too high, the Gibbs free energy will favour the entropically more stable internal solvation.^{57,63}

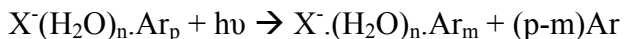
The solvated structure of the halide water clusters was deduced through infrared (IR) studies by exploiting the environmental sensitivity of the OH bond in water. In a water cluster there are essentially three types of possible OH vibration. The most familiar is the highest energy free OH oscillation not interacting with its environment at an energy of 3710 cm^{-1} . The second oscillation is that found in neutral water clusters,⁶⁴ corresponding to OH oscillators hydrogen bonding to other waters, with values near 3600 cm^{-1} .⁶⁵ The third type, which is the lowest in energy, is the ionic hydrogen bond. When an OH moiety interacts with an anionic halide the attraction causes an increase in the OH bond length as well as a reduction in the bond's force constant k , which produces a red shift in signal. The energy shift is dependent on both the halide and the number of water molecules interacting with the halide. This shift relative to the free OH oscillation can range from 135 cm^{-1} in $\text{I}^-(\text{H}_2\text{O})$ to 210 cm^{-1} in $\text{Cl}^-(\text{H}_2\text{O})$.

Initial studies in 1996 aimed at exploring the prominent modes through vibrational action spectroscopy.⁶⁶ This technique utilises a tuneable laser to scan through the IR range of frequencies, and the resulting excitation of OH modes leads to photoinduced water monomer evaporation which is detected by a mass spectrometer:



The aforementioned values were not obtained using this exact technique, as the water clusters cannot be sufficiently cooled to yield transitions from a minimal number of low

lying vibrational states. Furthermore, for the particularly stable $F^-(H_2O)_n$ clusters, excitation of the OH modes does not even induce evaporation. Following the technique pioneered by Okumura and Lee⁶⁷, Ayotte *et al*⁶⁵ found argon predissociation spectroscopy cooled the clusters sufficiently, and relies on the $X^-\dots Ar$ formation energy as opposed to more stable $X^-\dots(H_2O)$ analogue:



Using this technique, the presence of internal solvation in all fluoride clusters has been corroborated, in accompaniment with verification of the onset of internal solvation possible for iodide with three solvent molecules.⁶⁸ The exclusive nature of the fluoride for internal solvation at the trimeric level is understood through consideration of three body interactions. The fluoride anion donates electron density to the two water molecules that normally interact for the higher halides. Due to the smaller size of the fluoride, the like charge imparted on the two solvent molecules forces them apart and produces the experimentally observed internally solvated cluster.⁵⁷

A charge transfer state was also found in the fluoride water dimer at vibrationally excited states in the anion. The anion's potential with respect to the bridging proton's stretching mode (ν_{OH_b}) has a distinct 'shoulder' due to the attraction of the fluoride anion. It was predicted that the red shift for an oxygen bound H_b would be some 2000 cm^{-1} , yet the experimental value was much less suggesting charge transfer to the fluoride had taken place to give $FH \dots OH$.⁶⁹

In the halide hydrogen sulfide system, *ab initio* calculations have suggested charge transfer occurs for the dimer, trimer and tetramer's optimised structure at the MP2/aug-cc-pVDZ level of theory suggesting that the proton affinity ranking is: $F^- > OH^- > SH^- > Cl^-$ and so on for subsequent halides.⁵⁹ Interestingly, the interwater hydrogen bonded network is not broken for the trimer and tetramer unlike the water – fluoride clusters of this type. This is perhaps due to the fact that the $FH\dots SH^-$ acts as the core of the structure, not the halogen in isolation. Thus, the $FH\dots SH^-$ is internally solvated by subsequent hydrogen sulfides, which necessitates inter solvent hydrogen bonds due to the hydrogen rich SH and FH moieties. If viewed in the perspective of an internal $FH\dots SH^-$ core as Wild suggests, one can exclude the hydrogen bonds formed with these moieties, suggesting that for the tetramer and larger structures, intersolvent bonding does not ensue. It is noted that internally solvated fluoride clusters are also minima for the clusters 3-5. In the trimer which notes an internally solvated F^- , there is no inter solvent H-bonding, also analogous to the water system.

These aforementioned studies were aimed at probing the competition between ionic hydrogen bonding and the solvent-solvent networks. It is believed that further investigation into analogous systems will provide results that add to the completeness of our understanding of ionic solvation. Rather than focus on infrared predictions for stepwise clusters of the sulfide, as has been done by Wild *et. al*, this Honours project has focused on the prediction of the photoelectron spectra for the 1:1 dimers of the chloride and fluoride hydrogen sulfide complexes. It is believed that the difficulties encountered by Cheshnovsky *et al.*⁷⁰ in 1996, should not be as significant a problem in this work, due

to the experimental inclusion of high pressures of argon to adequately cool the clusters vibrationally.

2 The TOF-PES

Successful construction of the TOF-PES has demanded a rigorous understanding of its many components and how they function in the context of an experiment. In the event that structural problems occur, or problems with resolution are observed, it is this understanding and intimacy which allow the fault to be located and corrected as quickly and efficiently as possible. In order to convey this understanding as well as illuminate the details of successful experimental operation, an analysis of the machine's components and requirements is given in accompaniment with specific construction related difficulties, whose solution inherently depends on the preceding detail. The labelled schematic of the TOF-PES is given in Figure 6, and this is the central diagram of this section.

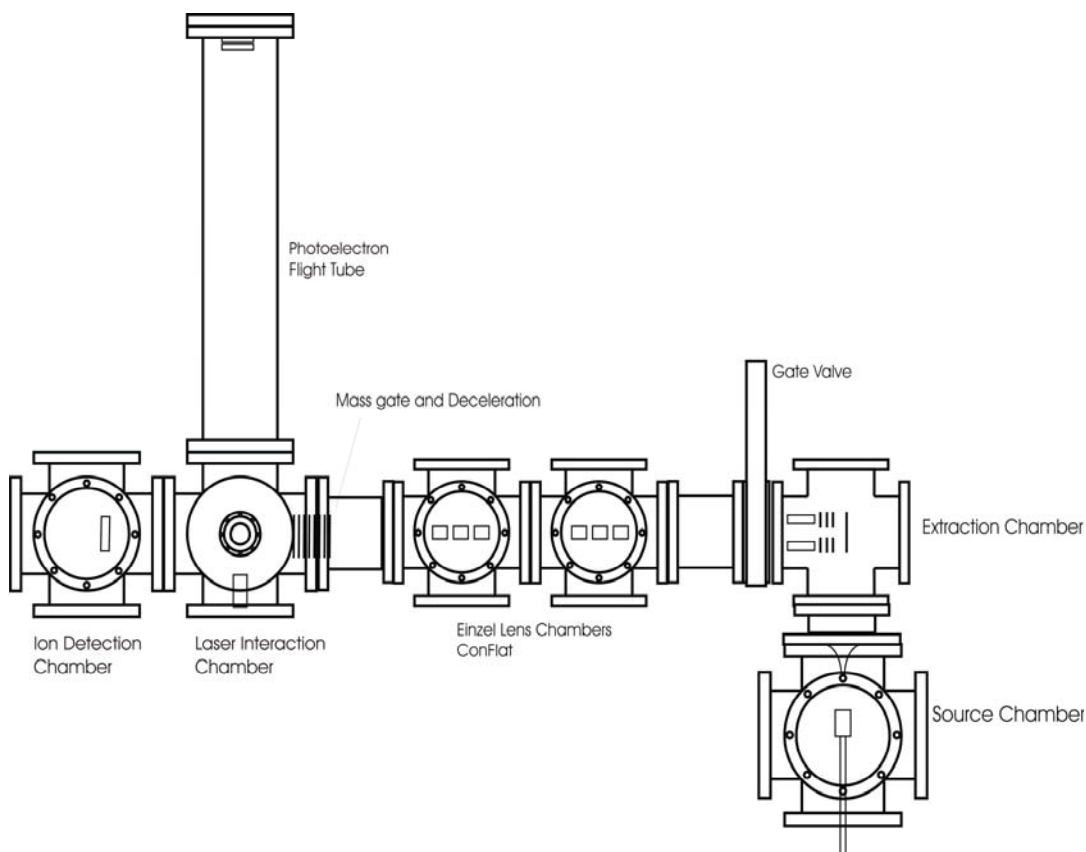


Figure 6- Schematic of the Wild lab TOF-PES

2.1 General Considerations

2.1.1 Vacuum System

In any instrument where charged molecular beams are steered and probed *via* electromagnetism, it is essential to maintain some level of vacuum. The presence of background gas inside an apparatus allows for molecular collisions with the cluster of interest, making it virtually impossible to control and steer said species any appreciable distance. Furthermore, background gases can also absorb any pulsed radiation before it reaches a desired target. The vacuum system that operates in the TOF-PES is provided by

two vacuum pump types – diffusion and turbomolecular. It should be noted however, that both pump types are backed by rotary pumps, which are required to provide a ‘roughing’ vacuum before the diffusion or turbo pumps can be powered on, as well as displace the throughput from these pumps when they are operational. Due to the different pumping regimes in the machine, these regions are isolated from each other by a manual gate valve, unless the machine is operational. In accord with the different pumping regimes are different flange connections to seal the machine from atmosphere: International Standardisation Organisation (ISO) and Conical Flat (CF) for diffusion and turbomolecular pumped regions, respectively). The ISO flanges are sealed by reusable VITON O-rings, which are copolymers of vinylidene fluoride and hexafluoropropylene, as opposed to non-reusable copper gaskets in the CF region. It should be noted that a better seal is achievable with copper gaskets, but considering that the source chamber needs frequent servicing, cost efficiency was considered of greater importance than the slight improvement CF connections would afford.

An E2M40 (Edwards 2 stage $40 \text{ m}^3 \cdot \text{h}^{-1}$ throughput) rotary pump backs the source and extraction chambers which each have a diffusion pump attached to their bottom inlet. This region of the TOF-PES is isolated from the rest of the machine by a manual gate valve (except when experiments are performed). The diffusion pumps can reach higher levels of vacuum than the rotary pumps, but they require a low pressure before operation (\sim mtorr). The purpose behind this can be understood when considering the design of a diffusion pump. The polyphenol (Santovac 5) diffusion pump oil is heated by a heating element thereby producing an oil vapour that ascends a central column inside the pump.

Upon reaching the highest point, the vapour is directed outwards towards the walls of the pump and down back to the oil reservoir. The large jet stream of oil collides with background gases, forcing them down into the sump where it recondenses and the trapped gases are ejected through the outlet. This process necessitates a low working pressure to ensure that the mean free path of the vapour is at least the length from the central column to the outer wall of the diffusion pump.⁷¹ In this way, there is a reduced chance of the oil vapour colliding with background gas and being forced into the source chamber. More generally, diffusion pump oil should not be exposed to atmosphere when at high temperature as the oil will oxidise or 'crack'. This is not as important a consideration when using silicone oil or Santovac5, but it can have disastrous effects for hydrocarbon oils.

The other type of vacuum system operating is turbomolecular pumping. This method makes use of specifically engineered turbines spinning at rapid speeds, which are designed so that gas molecules colliding from inside the apparatus are directed downwards out of the chamber to the fore pump (an E2M5 – Edwards 2 stage rotary operating at $5 \text{ m}^3 \cdot \text{hr}^{-1}$), whereas gas molecules colliding into the turbine from the fore line side are reflected back down. Both turbo pumps require oil for lubrication of moving parts and cooling water to prevent overheating. There are two turbo pumps operating, the larger of the two operating at 1000 Hz, and the smaller at 600 Hz.

Cooling water is an essential component for the proper function of both diffusion and turbomolecular pumps, as well as a necessity in cooling apparatus when experiments are

run. There are three water lines in use, all of which first pass through filters that require regular changing. The first line cools both diffusion pumps, and passes through 1/2" tubing to ensure a flow rate greater than 3 L.min⁻¹ as required. The second line cools both turbomolecular pumps and passes through 1/4" tubing to allow a lower flow rate of 1 L.min⁻¹. These two lines have taps incorporated into them to allow for a filter bypass when filter change is required, so that the pumps can remain operational during the temporary period required for filter change. The third line cools both the rhenium filaments and electromagnet (see section 2.3 and 2.5) which are only in use during experiments.

For the turbomolecular pumps, cooling water acts as a heat dissipating fluid on account of the moving parts generating energy therein. The diffusion pumps require water for two reasons: most obviously it allows the oil vapour to cool down and condense so that it can be recycled at the heating element. The second major purpose is to cool the background gases which enter the body of the diffusion pump. By slowing the background gas down, the vapourised oil can better fan it down into the outlet, as opposed to colliding in and then out of the main body; or worse, forcing oil vapour into the source and/or extraction chamber. The use of a liquid nitrogen trap serves as an even better background gas coolant, and is operational in the Speedivac diffusion pump attached to the extraction chamber.

It is not a simple task to reach high levels of vacuum (<10⁻⁶ torr) or ultra high vacuum (< 10⁻⁸ torr) due to the quality of seals required. Furthermore, the greater the volume inside

the machine, or the more chambers an experimentalist utilises, the more problematic reaching high vacuum becomes due to the sheer volume of air to be displaced as well as the number of leak-prone contact points offered by connecting chambers. Thus, even with as many vacuum pumps as has been employed for the TOF-PES, there were problems that needed correction in both the turbomolecular and diffusion pumped regions. The method utilised to 'leak test' a vacuum system works on the very basic principle of pressure gradients. By attaching a helium mass spectrometer to the fore line of one of the pumps, and spraying a fine nozzle jet of helium around the outside of each individual joint in the machine, one can determine leaks based on the intensity of signal achieved by the helium tuned mass spectrometer.

The first significant leak was found on Einzel lens 1 chamber connection to tubular adaptor two. In order to mount the brass cylindrical Einzel lens assembly into the chamber, a stainless steel plate with a central annulus had to be welded onto the end of the chamber, acting as the attachment region (with three points of connection) for the Einzel lens assembly. In this process, the weld of the five way chamber had to be expanded slightly to properly attach the Einzel lens. It was found that this expansion was slightly too great, resulting in a crack in the weld. The flaw was not noticed at the time of initial modification, but was easily welded closed after confirming the presence via testing.

The subsequent second and third leaks were both artefacts of the poly methyl methacrylate (pMMA) ISO flange implemented in the source chamber to view the

rhodium filaments in working order. The first and indeed most devastating leak was due to one single human hair lodged onto a VITON O-ring when sealing the chamber. This extremely small imperfection produced leaks that exceeded the signal capacity of the leak detector. Upon removal of the hair the problem is no more, but it serves as an impressive affirmation of the importance of extreme cleanliness when constructing the chambers.

The second minor leak was due to a structural flaw in the workshop fabricated pMMA flange, which like the human hair did not allow for a perfect seal. A light treatment with emery paper and subsequent polishing removed this flaw, and has allowed for 10^{-8} Torr to be reached in this chamber. To reinforce the quality of vacuum in these chambers, note that at the ultra high vacuum reached in the CF region the mean free path of an atom is approximately 50 km.⁷¹

2.1.2 Safety System Programming

In order to maintain extremely high levels of vacuum, it is important that all potential hazards be modified and eliminated where possible. To combat the possibility of vacuum failure and/or chamber contamination a safety system has been developed incorporating a programmable microchip (PICAXE). The flow diagram in Figure 7 illustrates the core purposes of the safety program written in 'Basic' programming (code in Appendix). In essence, it ensures that if any vacuum related component in the apparatus becomes faulty, the problem will be identified and the power turned off. However, the program has subtlety, in that it has separate checking routines for the two different vacuum regions of the apparatus. The program loops about checking the pressure gauges in the machine (ion

gauges), and on the backing rotary pumps (Pirani gauges) for both regions. Accompanying this, the ISO side has the temperature of the diffusion pump's heating switches and water flow switches monitored. In this way, the TOF-PES is protected against oil vapour entering the main chambers because of poor cooling. If any of these variables exceed threshold values (converted to voltages to allow the PIXAXE chip to read them as inputs), then depending on the area of the fault, an 'off' subroutine is accessed within the program. In these respective 'DiffOff' and 'TurbOff' subroutines, the program monitors the region which has not malfunctioned, whilst waiting fifteen minutes to remove power to the backing pumps and close the solenoid valves which connect the pump to the fore line. This delay ensures that there is not a large pressure difference between the backing rotary and the recently turned off diffusion or turbomolecular pumped chambers, by first allowing the pressure inside the chambers to gradually rise prior to the backing rotary pumps powering down. If the opposite vacuum region does fail before this user specified time frame, a second subroutine is invoked – 'AllOff', where the aforementioned process occurs simultaneously for both sections of the apparatus.

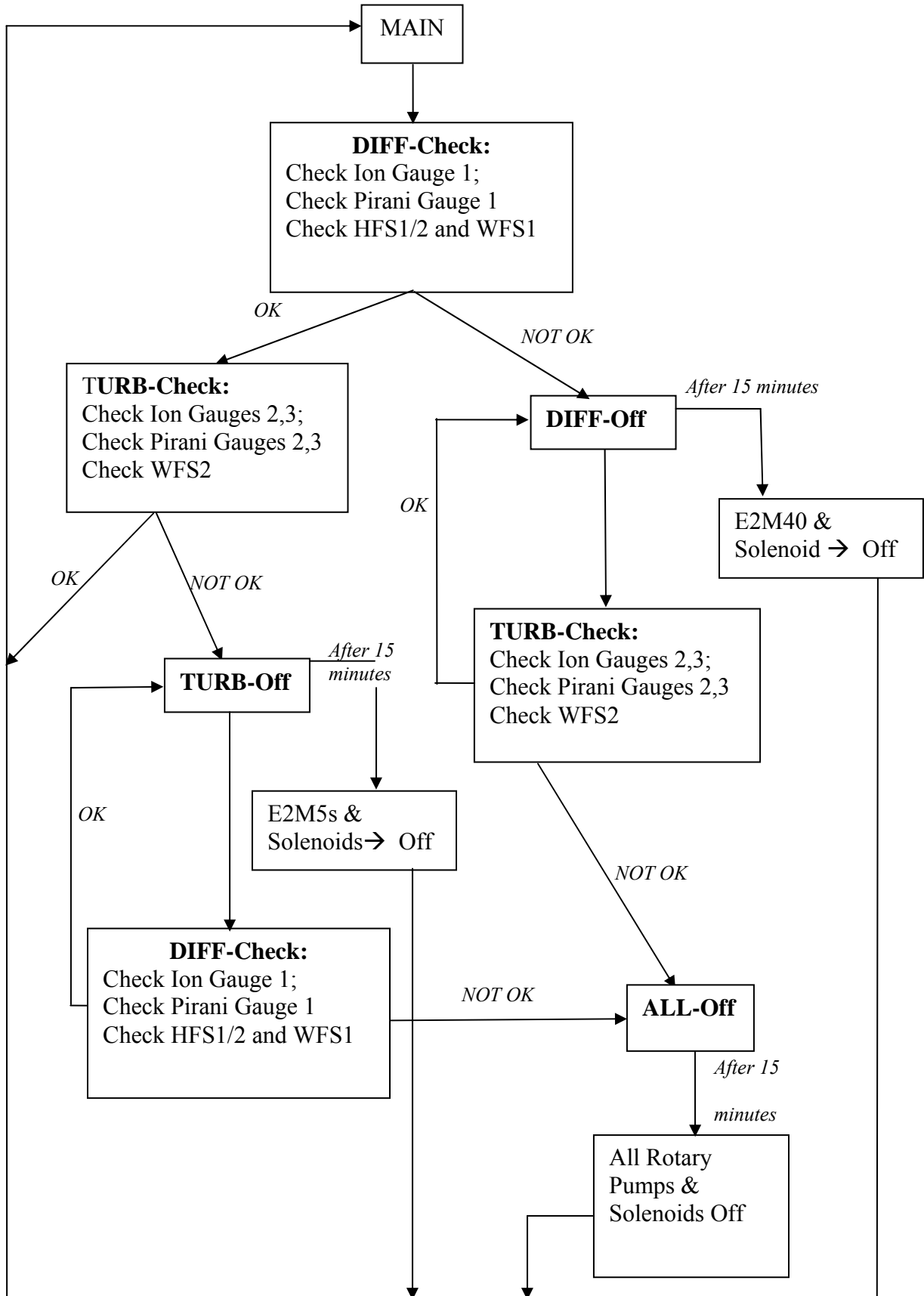


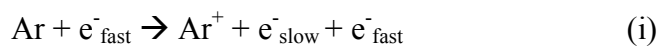
Figure 7 - Flow diagram showing the safety system which monitors the TOF-PES

2.2 Gas Mixing Station

The gas mixing station (GMS) is the starting point of any experiment performed in the TOF-PES. It has four main entry points for reaction and/or buffer gases/liquids – three gas lines and one liquid sample vial which is used for volatile liquid samples not readily available in the gas phase. To ensure the successful vaporisation of liquid samples, as well as to ensure the purity of the gases pumped into the apparatus, a rotary pump is connected to evacuate the GMS. This reduced pressure above the liquid sample ensures the vapour pressure of the liquid required for evaporation is less, forcing the liquid sample into the gas phase. A liquid nitrogen ‘trap’ has been incorporated into the rough vacuum line, to ensure that oil from the rotary pump cannot enter the GMS. Rotary pump oil can be drawn out of the pump if there is lower pressure outside of the rotary pump than inside. While it is the utility of vacuum pump oil to have extremely low vapour pressures, prolonged use of a vacuum pump may lead to significant oil vapour entering the gas mixing station without a liquid nitrogen trap in place.

For the actual experiment to be undertaken that is hoped to corroborate the theoretical predictions (see section 3), it is worth noting how the cluster shall be formed utilising the GMS. The method of cluster formation utilises NF_3 as a source of F^- and CCl_4 as a source of Cl^- . A chemical like CCl_4 requires the sample vial of the GMS as it is not readily available in the gas phase. The second gas phase species is H_2S , and the third is Ar. The Ar is used for two reasons – firstly as a cooling buffer gas in the same way as it is used in vibrational action predissociation spectroscopy (see section 1.7). The second purpose is to produce slow e^- which have a better attachment cross section with both NF_3 and CCl_4 .

to produce their respective anions.⁷² The basic reaction scheme for the fluoride cluster formation would be:



2.3 The Source Chamber

The source chamber is pivotal in the production of charged clusters, which are subsequently extracted so that only anions are detected. The gas mixture produced in the GMS is connected to inside of the source chamber, contained inside paraformaldehyde tubing against a barrier, which is triggered open via the ‘pulsed nozzle driver’. While the electronics controlling this device are quite advanced, the workings of the nozzle can be understood by some core electronics principles with the aid of *Figure 8*. A poppet and spring inside of an armature, which is inside a coil, block the flow of gas. By pulsing the coil with a current, a magnetic field is induced, which provides the magnetic armature a force upwards further into the coil, allowing the spring to compress, and also allowing the flow of gas into the source chamber. When the current is pulsed off, the spring then releases its stored potential energy, and in conjunction with a buffer spring on the other side of the armature, ensures that the assembly slides back over the exit port, disallowing further gas flow. Two variables are controlled by the user: pulse width and pulse energy. If the current is maintained, the armature is held inside the coil longer making the width of the gas pulse increase. Similarly, by increasing the current applied to the coil, the

acceleration due to the increased magnetic force ensures the gas enters the source chamber more vigorously (i.e. the pulse has greater energy).

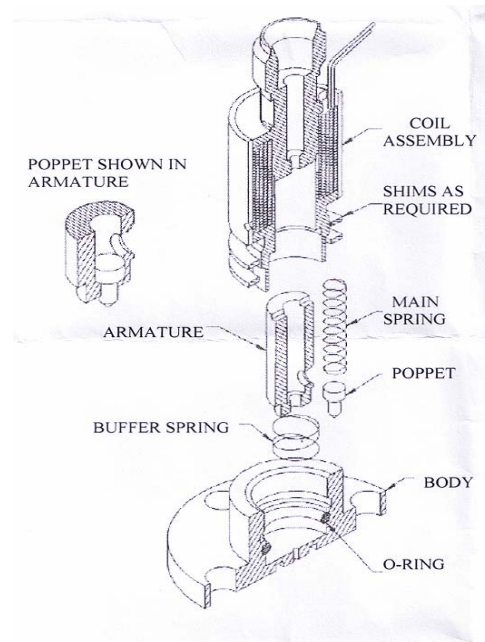


Figure 8– Schematic of pulsed nozzle from ref. 73

The next logical components inside the source chamber are the electron filaments which allow for the production of charged clusters. A high voltage and high current is passed through thin, short lengths of Rhenium wire leading to thermionic emission of electrons. The conventional choice filament is thoriated iridium, but as the work conducted in this apparatus relies heavily on halide clusters, and considering thoriated iridium has a poor resistance to halide attack, Rhenium has been found to be a suitable alternative.⁷⁴ The filaments run parallel to each other, with the region between them containing the gas pulse. In order to focus this thermionic emission on the gas expansion, there lies a highly negative isolated floating potential barrier on the outside region of both filaments, so that any electrons ejected outward from the expansion can be repulsed into the focusing

region. This arrangement is a type of electrostatic lens known as a Wehnelt's lens. Due to the heat generated by these filaments, and in the interest of maintaining their life, the ensemble is water cooled by the water circulation system.

The final component in the source chamber is the conical skimmer. While the gas nozzle driver's purpose is to provide a sharp jet of laminar gas flow into the chamber, it must be remembered that the source chamber is conventionally at high to ultra high vacuum, and it is the nature of the gas to expand in all directions. The conical skimmer therefore acts as collimator on account of the thin (1 mm or 3 mm) orifice which the gas must pass through in order to reach the extraction chamber. The conical shape can be viewed as a means to maintain the integrity of the gas expansion. If the orifice was flat as opposed to curved, any non-passing gas molecules would be reflected into the gas expansion. The high angle of reflection that the skimmer provides ensures that these gaseous species are not redirected into the expansion, but forced elsewhere to be evacuated by the vacuum system. The key purpose of such collimation is translational cooling of the clusters pumped into the source. Temperature can be defined as the degree of random motion of molecules⁴ which is quenched in two degrees of freedom synergistically by both the supersonic expansion of the gas nozzle and the conical skimmer.

It is worth noting here, the reason why it is the desire of many gas phase spectroscopists to ensure that the gases pulsed into an apparatus are 'cold'. The 'warmer' such samples are, the more freedom the samples have to access more quantum states, which can lead to crowded and complicated spectra that are difficult to interpret. The key methods utilised

in the TOF-PES to produce cold samples involve the pulsed nozzle driver in conjunction with the conical skimmer for translational cooling. The second method is the use of a buffer gas (e.g. argon) to ensure vibrational cooling.⁵⁷ The choice of a heavy non-reactive gas ensures that it can better absorb vibrational energy from preformed clusters through inelastic collisions. The use of a buffer gas is essential in removing ‘hot-bands’ which are transitions from the anionic state with vibrational energy higher than the zero point energy. By doing this, the spectrum is easier to interpret as vibrational progressions come from one state of the anion. Whilst the buffer gas may not necessarily remove hot bands totally, it has been shown to have a significant effect in deconvoluting spectra.⁷⁵

2.4 Extraction Chamber

After exiting the source chamber, the gas phase clusters are then redirected down the flight tube of the apparatus, due to the perpendicular deflection allowed by the extraction plates. These are five stainless steel plates (three of which are active in the extraction) as shown in Figure 9, three of which have annuli to allow for the passage of the anion beam. The second from last plate is pulsed with a high negative voltage, the middle a lesser negative voltage and the fourth and fifth plate are at ground potential. This setup ensures that only anions can traverse the time of flight tube, as any cations formed in the expansion will be deflected to rightmost plate, while neutrals are unaffected and continue through to the wall of the chamber. The question could be posed as to why there are three plates, as opposed to say one, which could still redirect the path of a molecular beam? As evidenced by the original papers of Wiley and McLaren in 1955,⁷⁶ the three plate system allows for better space resolution, controlled by altering the ratio of voltages between

plates one and two. In this way, any anions with imperfect linearity of momentum from the pulsed expansion can be corrected for at the very first stage of the mass spectral time of flight.

The subsequent component in the extraction chamber is the X-Y deflection plates, which simply steers the beam by virtue of two parallel charged plates which produce electric

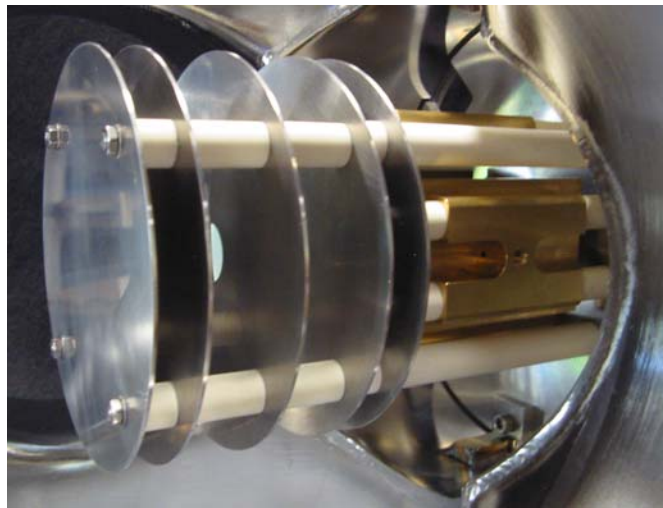


Figure 9 - Time of flight plates and X-Y deflection plates electrically isolated via ceramic tubes. Note the back plate is for structural purposes, not beam deflection.

fields perpendicular to the flight of the beam. A design feature worth noting in this extraction and deflection system is the use of ceramic tubes to electrically isolate the extraction plates and X-Y deflection. Throughout the whole ensemble are four stainless steel threads which hold the assembly together. Surrounding each thread is an equivalent length of ceramic tubing, ensuring that the thread does not make contact to all the plates except the left most one in the Figure 9. Another set of ceramic spacer tubes are also used, which dictate the spacing between the plates. This is the ceramic that is visible in

the picture, and is not composed of one singular unit, but five individual sections for each section. This assembly can therefore have high voltage pulsed to the third and fourth plates of the assembly, and due to no path of contact between electrical conductors, they each hold their individual voltage.

2.5 Beam Focusing and Detection Schemes

In order to attain a high mass spectral resolution, the most obvious method is to increase the length of the flight tube. It is intuitive that the spread in times will be greater for particles/clusters traversing a longer flight tube at some fixed but different velocity (due to difference in mass). While this approach can increase the mass spectral resolution, it will actually reduce the intensity of the ion signal due to Coulomb repulsion of like charged species. To combat this problem, electrostatic lenses (or Einzel lenses) can be used to refocus a charged molecular beam. There are two Einzel lenses within the apparatus, and they are essentially brass cylinders mounted on a stainless steel frame (electrically isolated by ceramic rods) with three segments (see Figure 10). The outer two are held at ground potential, while the central component is held at a high negative potential. This type of lens is completely analogous to a classical optical lens, in that it can focus an anionic beam onto a fine point on account of the repulsive force the central component of the Einzel stack imparts on the beam. Here the ceramic insulators are used to isolate the lens from the mounting frame, which is welded into the inner surface of the flange connection, making it at ground potential. The use of two lenses in series is not completely necessary, but is considered a preventative tool against the beam focusing

before detection and then repelling outwards prematurely. Their operating voltages range between 0 and -3 kV.



Figure 10- Einzel lens stack from side and front profile. Note the three segments and ceramic posts to electrically isolate the assembly

The other assemblies used in the TOF-PES to improve the signal of the detached photoelectrons are the mass gate and deceleration located after the final Einzel lens and before the laser interaction chamber. It improves the relative photoelectron signal by slowing down the charged beam, which reduces Doppler broadening and therefore allows for a more consistent e^-KE distribution, especially for electrons which are photodetached with different initial trajectories. The mass gate and deceleration stack look quite similar to the extraction plates, and work on similar principles. The first two annuli make up the mass gate and are maintained at a high negative potential that prevents the charged beam from reaching the ion detector at the end of the time of flight tube. Depending on the cluster being probed, the mass gate is pulsed to ground potential at a specific time,

allowing the passage of this ion. Simultaneous to this pulse is a lower negative pulse to a plate after the gate. This second plate, or the first deceleration, is connected to the next plate via a 100 k Ω resistor that steps down the voltage. This set up is repeated for the next seven plates, making a deceleration stack that gradually reduces the kinetic energy of the beam. Notice that the ceramic tubes are incorporated, again to ensure that the subsequent plates are electrically isolated.

In order to focus the detached photoelectrons to the detector perpendicular to the plane of motion of the charged beam, a magnetic bottle assembly is used.⁷⁷ While there are many different, and better resolving photoelectron focussing systems (such as zero electron kinetic energy photoelectron spectroscopy and slow electron velocity imaging), this assembly in conjunction with the mass gate/deceleration lenses, as well as the ultrahigh vacuum achieved in these chambers, should give resolution on the order of 1 eV or better, based on other systems using a similar magnetic bottle setup.⁷⁷ The solenoid coil wound about the photoelectron flight tube is also protected by a μ metal shielding tube that blocks out the earth's magnetic field. This lack of interference from the earth's weak magnetic field produces a better quality bottleneck magnetic field array, ensuring a better quality signal than without. The copper electromagnet is pulsed to ensure that a particularly high magnetic field value is reached, which accordingly produces a significant amount of heat. For this reason, the assembly comes with a water cooling setup which is operational at present (see 2.1). It is only needed when experiments are performed, and therefore runs on the water line common to the source chamber's filament cooling system.

2.6 Laser

A 1064 nm Nd-YAG laser is to be used for photodetachment,⁷⁸ by generating the fourth harmonic of 266 nm through the use of two optical harmonic generators in series. Then, by using two dichroic mirrors, the laser beam can filter out the 1064 nm and focus the beam back into the correct direction. Directing the light into the machine requires the use of two mirrors and one lens: the first mirror directs the light underneath the laser chamber, while the second (mirror mounted onto a 'bread board' incorporated into the Dexion) redirects the pulse upwards through the quartz mirror at the bottom entry port of the laser interaction chamber. Quartz (not glass) must be used as it does not absorb UV radiation. The lens, like the mirrors, can have its position varied by virtue of the many mirror mount ports on the breadboard. It can therefore be adjusted to focus the beam into the very centre of the laser interaction chamber, providing the best perpendicular crossing with a mass selected cluster. The entrance ports have graphite painted matt-black baffles incorporated into them to reduce continuous reflection of stray light. The uppermost port of the laser interaction chamber also has a quartz mirror and baffle assembly, but with a 30° angle of inflection, as opposed to flat. This way, any reflected light will be absorbed by the baffles at the exit port, instead of being redirected back to the laser.

2.7 Pulsing Methods

While the discussion thus far has given a compartmentalised view of the TOF-PES, it is essential that the apparatus as a whole entity be understood, which demands that a qualitative view of the pulsing sequences be explored. The focussing, extraction and

improved resolution schemes are not all continuously operational. To ensure that particular components of the molecular beam be extracted and examined, a basic pulsing motif is presented and shown in Figure 11. Obviously this begins with the pulsed nozzle driver, which operates at 10 Hz with controllable pulse width and pulse energy. Utilising two DG535 timing boxes, this acts as t_0 for all subsequent pulses. Upon passing through the conical skimmer into the extraction chamber, the extraction plates are pulsed to a high negative voltage. However, both the timing and the voltage magnitude cannot be controlled by the same device. A timing box was made by the electronics workshop, which receives two inputs: a high voltage and a timing pulse, which the circuitry converts to a pulsed high negative voltage signal. The DG535s cannot be used in isolation as they can only reach voltages of c.f. 5 V, yet the magnitudes required are kV. The Einzel lenses are electrostatic lenses, and therefore do not need to vary in time. The next timing components are the mass gate and deceleration plates,⁷⁷ with the deceleration pulse almost immediately after the mass gate. The mass gate is pulsed from negative potential to ground, while the deceleration is pulsed from ground to a voltage less than that of the energy of the beam, in order to slow it down rather than completely repel it. The next pulse in the logical flow of the experiment is the laser pulse, yet it actually occurs slightly before the mass gate as it must traverse some distance before making it to the centre of the laser interaction chamber. Immediately after the laser has interacted with the mass selected cluster, the strong electromagnet and solenoid ‘magnetic bottle’ assembly is pulsed so as to collect the photodetached electrons.

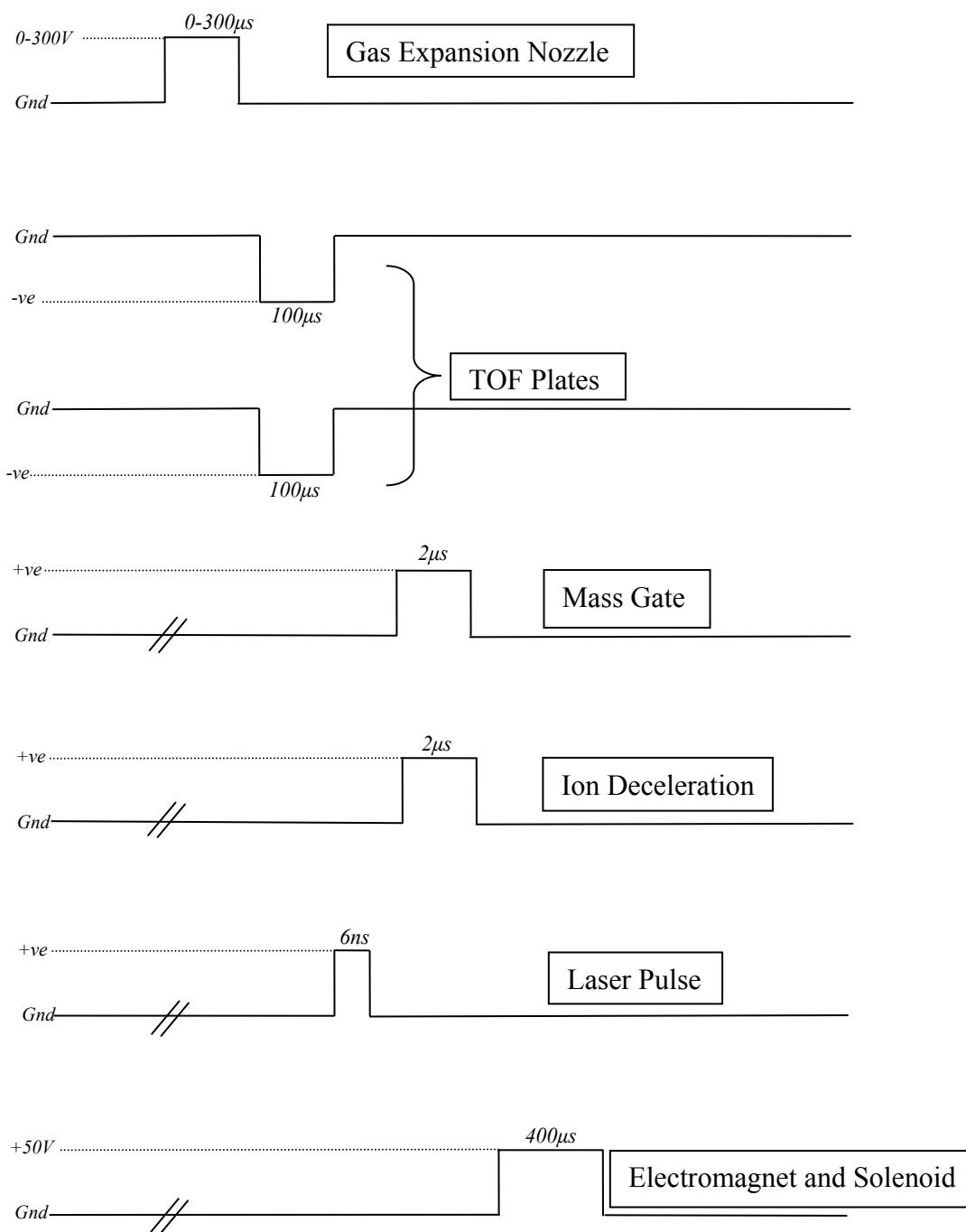


Figure 11 – Qualitative description of the pulsing scheme employed in the TOF-PES to manipulate and analyse mass selected clusters

The pulse width is somewhat longer to ensure that the all photoelectrons are subject to the same magnetic field. In order to ensure the highest quality photoelectron and mass spectrum, such pulsing sequences need to be adhered to, so that the cluster under investigation is properly mass selected, ionised, and the resulting electrons detected.

Given here are seven timing related parameters that are controlled by the experimenter. Accompanying these parameters are the actual voltages applied to the extraction plates, Einzel lenses and deceleration plates. The emphasis here is that the optimisation process to obtain a signal is sometimes tedious. Furthermore, one cannot ever be certain that the most optimum parameters are in use, because there are different sets of variables which provide sufficient quality. It is not the goal of the spectroscopist to obtain the most perfect set of variables, as long as they allow for the recording of spectra with acceptable signal to noise ratios.

2.8 Detectors

There are two detectors implemented in the TOF-PES – one for ion detection and the other for photoelectrons. They are both chevron microchannel plate detectors that have a positive bias to attract the negative ions/electrons. The ion detector is mounted onto a translation device so that the signal's optimum location can be found. To ensure that no torque acts on this detector, rather than have the proboscis of the translation device enter the apparatus from one of the side flanges, it enters from the uppermost flange. The design used by the workshop in the construction is given in Figure 12.

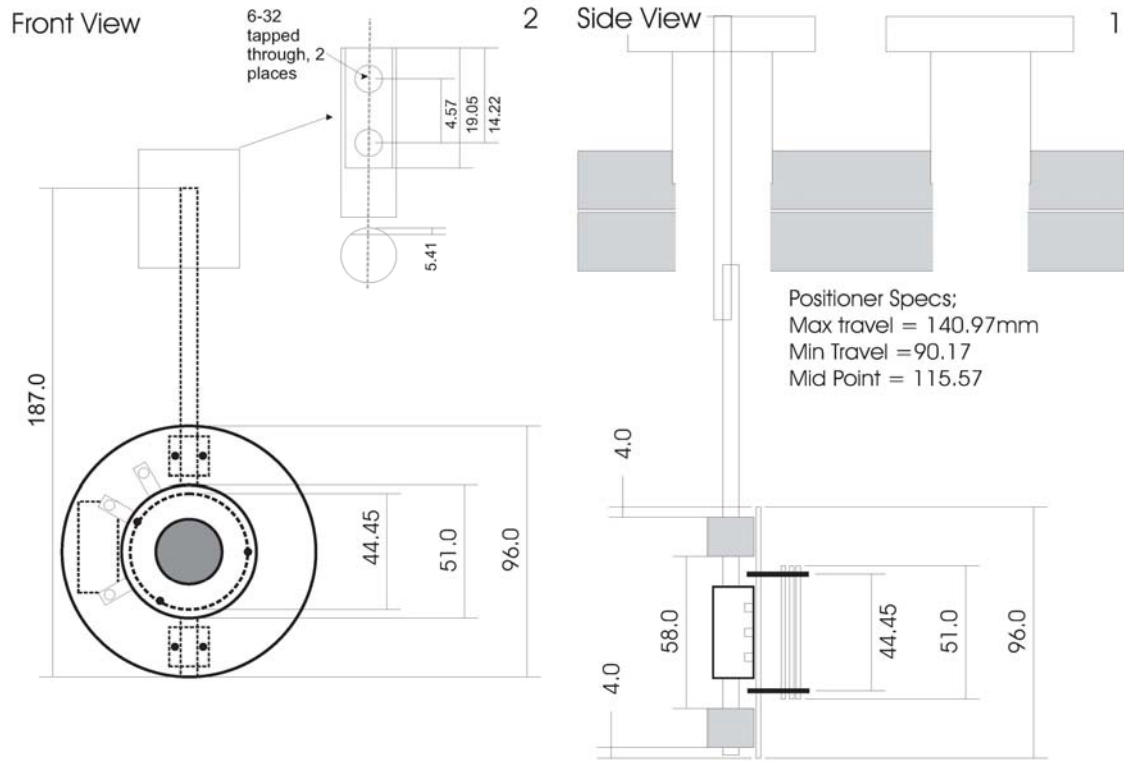


Figure 12 – Side and front view of ion detector mounted to a vertical adjustment stage. All units given are in mm.

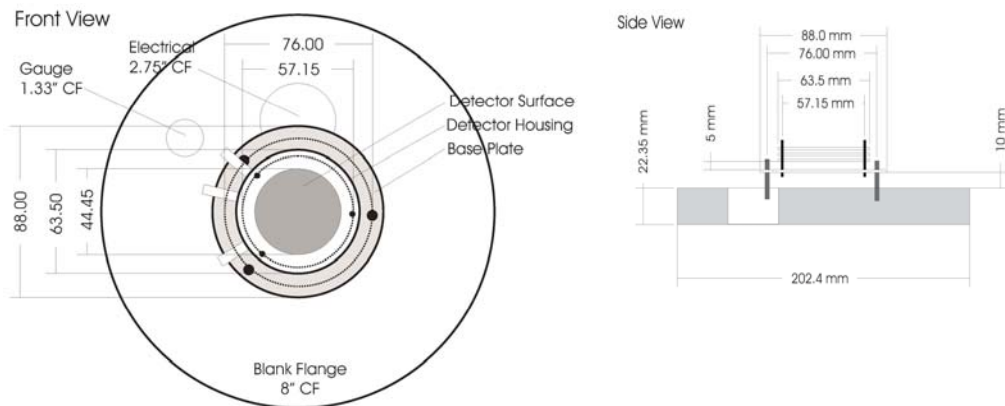


Figure 13 -Front and side view of photoelectron detector on 8" blank flange. Units are in mm unless otherwise stated

The photoelectron detector is mounted onto a stage which is then mounted onto the flange at the terminus of the photoelectron flight tube. In this way it can be detached when work is required, or replacement needed. In selecting the size of the stage, placement and size and width of threads to hold it down, it was necessary to consider the other inlets on the flange to ensure that no overlap occurred. The final design used by the workshop for construction is given in Figure 13.

From an electronics perspective, it is important to realise that the signal must be resolved i.e. signal from one burst of ions is not overlapped with a subsequent one. A basic view of the electronics at play is given in Figure 14. It is the choice of capacitor here which determines the resolution, as the capacitor charges and discharges according to the influx of electrons from the chevron plates, its value must be chosen so that a burst of ions/electrons does discharge the capacitor, yet not too frequently so that it does not discharge and charge during a single burst of signal. The ratio of values for the resistors between the anode and back face, and the back and front face have been selected so that the voltage at the back face is 2/3 that of the anode. The voltage divider relationship between voltages and resistor choice is:

$$V_B = V_A \cdot \Omega_{BF} / (\Omega_{BF} + \Omega_{AB}) \quad (9)$$

Thus for the back face to have a voltage that is 2/3 of the anode, the Ω_{BF} is half the value of the Ω_{AB}

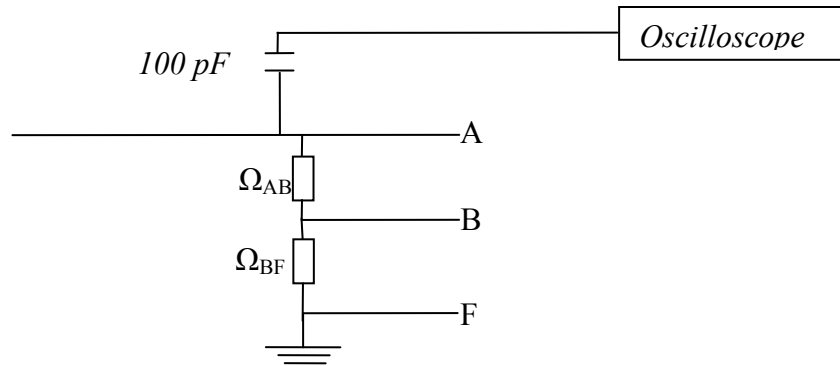


Figure 14 – Voltage divider set up for the microchannel plate detectors

2.9 The Construction

The first concern to be encountered was a consideration of how and what to mount the apparatus on. The use of a general purpose shelving material Dexion was employed, after initial designs were constructed so as to individually compartmentalise and support each chamber/section and ensure that the 900 mm high diffusion pumps had enough clearance from ground. Accordingly, the required lengths of standard non-galvanised steel Dexion were ordered and cut to size using workshop facilities. The schematic of the scaffold is given in Figure 15.

While the Dexion is capable of keeping the apparatus at a consistent working height, by itself it cannot allow for a level plane as the chamber sizes and connectors are not the same size. For this reason, and to ensure overall stability of the apparatus mounted on the Dexion, stainless steel supports are incorporated into the scaffolding of the machine. By

drilling through the Dexion and inserting a threaded rod through both it and the Dexion,

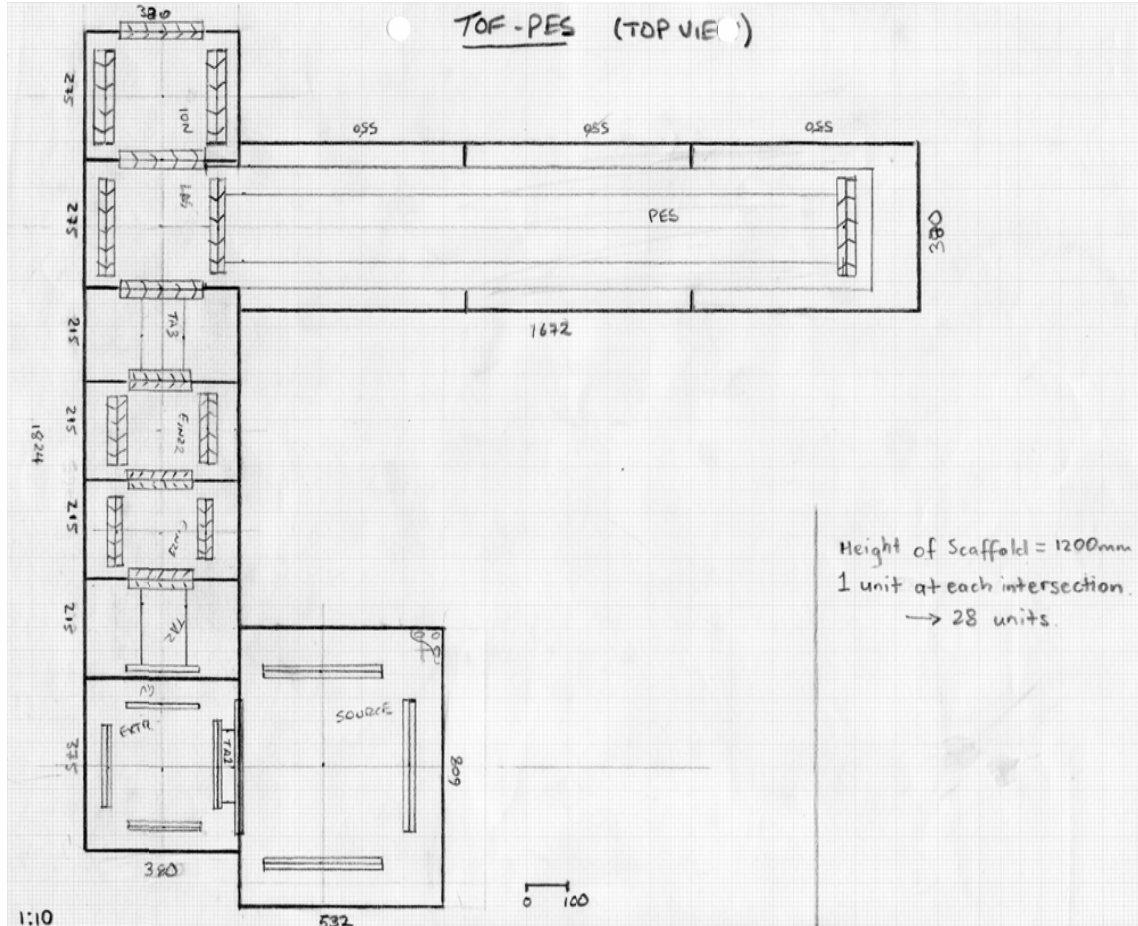


Figure 15 – Schematic of apparatus scaffolding. Darker print indicates Dexion, with fairer print showing chamber flanges and positioning

the level of each individual support can be altered so as to better support each chamber. The source chamber (ISO260) is the largest and is therefore mounted onto a support which is directly mounted on the Dexion, whilst the Einzel Lens chambers (CF150) are the smallest and require the greatest distance between Dexion and support (100 mm). To ensure that there is no undue stress on the chambers due to a harsh metal on metal single point of contact, the supports are covered by a strip of nitrile rubber on the region where it contacts each chamber. In this way, there is a plane of contact and the chambers are properly cushioned to avoid undue stress.

Both diffusion pumps used in the apparatus are second hand,⁷⁹ and therefore required cleaning to remove any cracked oil from the large interior surface. In this way, any porosities and volatile substances trapped were removed, allowing for a better quality vacuum to be achieved. The difference between their initial and final states is shown in Figure 16.



Figure 16 – Before and after comparison of internal component of DiffStak diffusion pump

Perhaps the biggest problem found during the construction of the TOF-PES was the lack of a satisfactory level when the Einzel lenses were attached. If either time of flight axis is not in line, then there is a much greater risk of the beam clipping any one of the components within; making a quality signal virtually unachievable. A significant uneven level was found when the second Einzel lens was attached. It appears that a manufacturing fault had occurred in the production of a five-way cross stainless steel chamber. Rather than presenting five individual pipes to one another, the manufacturers

have most likely taken a standard four-way cross chamber and welded another tubular entry in the bottom. This welding process has caused stress at the joint where it connects, which has extended to the four entry points and caused them to bow downwards. The actual lenses inside the chamber have been aligned linearly at their meeting point which is the mid-point of the two chambers in series, but the outer ports which connect to tubular adaptors two and three sagged downwards. To combat this severe problem, stainless steel spacing flanges were purchased and made into wedges by the workshop staff as Figure 17 shows. In this way, the bowing was corrected and the level of the machine is flat. In order to calculate the amount the width of the flange should differ from top to bottom, the mid flange of each Einzel lens chamber was placed upright on an extremely flat table. The height from the reference mid point flange to the opposite side was measured at various points around the top entry point. Due to the bowing the height will be greater at one end and the slope of the chamber inlet is calculated to be assimilated by the wedge.

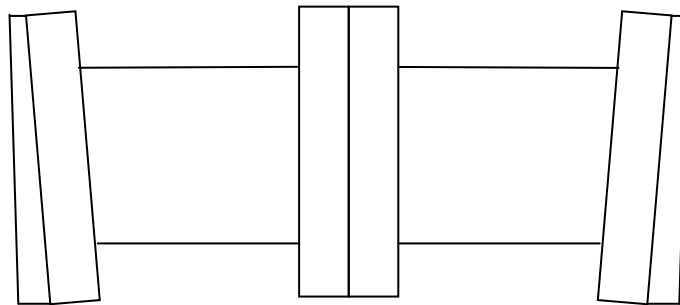


Figure 17 – Einzel lens chamber correction scheme.

2.10 Net Progress

The TOF-PES is operational and experimenting is in its testing stages. The search for a mass spectrum utilising methyl iodide has yielded hopeful results (see Figure 18). The sharp feature occurs approximately 25 μs after the TOF plate pulse which is in good agreement with the predicted value of 24 μs . Furthermore, the signal is found to vary in intensity with the pulse width and energy; vary temporally for changes in pulse time and TOF plate energy, suggesting that all the components of the TOF-PES, and the signal is due to a charged species that is traversing the layout of a typical experiment. The Einzel lenses and X-Y deflection plates both offer fine control of the temporal position of the signal which is also encouraging. The mass gate and deceleration still remain to be tested, and the laser arrangement of mirrors and lenses still needs to be completed. These two advances shall be implemented as soon as consistency of signal can be gained for the mass spectrum, as for unknown reasons the signal fluctuates randomly with time.

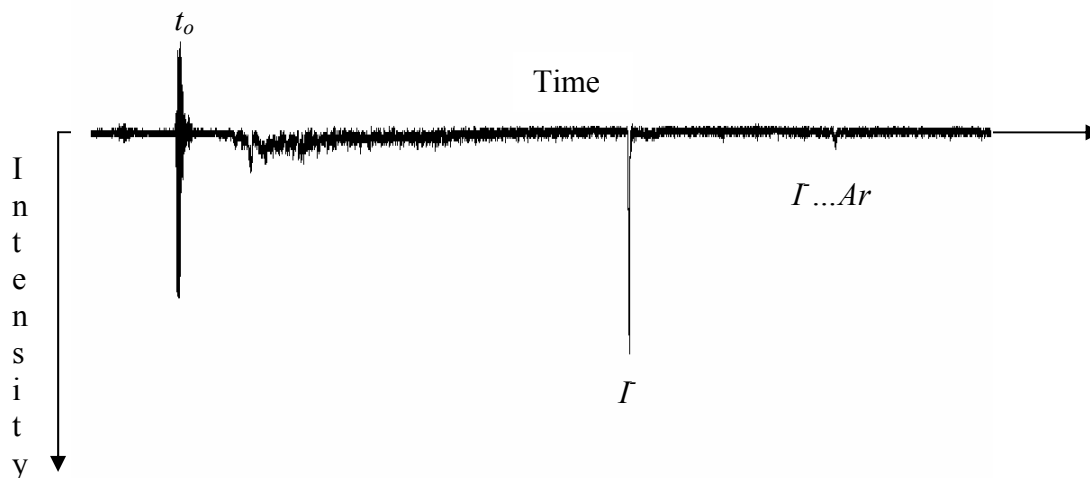


Figure 18 – Mass spectrum obtained for methyl iodide with argon buffering gas

3 *ab Initio* Calculations

3.1 *Computational Methods*

While there has been recent work on the halide hydrogen sulfide cluster's predicted infrared spectrum, the photoelectron spectrum has not been treated. It should be noted that some of the preliminary steps involved in the prediction of both spectra are the same, yet for completeness sake, computational familiarity and to ensure consistency between results, some of these were duplicated. The first common step is the need to optimise the geometry of the complex. Irrespective of the level of theory or basis set/s used in these calculations, the fundamental procedure of how this is done remains constant. The energy of the system is calculated (this is where methodology is variant), and the gradient of this energy sampled by slightly modifying the geometry to see if an extremum or saddle point has been located. When the gradient has been minimised to some input threshold value the system is then checked via vibrational analysis to verify if a minimum has been located. The vibrational analysis verifies whether a minimum has been located according to the following. The force experienced by nuclei in any cluster is approximated by a harmonic potential analogous to a ball on a spring:

$$F = -kx \quad (10)$$

Where x is the displacement from the minimum energy value, k is the spring constant and F is the force experienced. From classical mechanics it is noted that the potential energy is the negative integral of this force with respect to the displacement coordinate:

$$E_v = \frac{1}{2}kx^2 \quad (11)$$

When the gradient is sampled by the optimisation methods of any computational software, the force on the cluster at that particular geometry is sampled. To verify if the geometry with zero force is in fact a minimum, the gradient of the force with respect to the x coordinate is taken:

$$\frac{\delta^2 E_V}{\delta x^2} = -\frac{\delta F}{\delta x} = k \quad (12)$$

If the value of this second derivative k is negative, a maximum has been located, with the converse true for the alternate case. This k value is essential when determining the harmonic vibrational energy levels according to the classical equation for harmonic frequency:

$$f = \frac{1}{2\pi} \sqrt{\frac{k}{m}} \quad (13)$$

Where f is the harmonic frequency, k is the calculated spring constant, and m is the reduced mass. If k is positive (i.e. the second derivative test is positive), then real frequencies are obtained, and a minimum has been located on the system's potential energy surface. If however, the value of k is negative, then the frequency calculation has to take the square root of a negative number which yields an imaginary frequency, corresponding to a transition state or saddle point on the system's potential energy surface. The frequency values quoted may not be reliable due to the harmonic approximation of a Morse-like potential (especially at the higher energy vibrational levels). However, in terms of determining if an optimum geometry has been located, the only concern is the real or imaginary nature of the value given. The method given above is for the simplest of cases – potential energy depending on one dimension. For the cluster under investigation: [X...(H₂S)]⁻ there are six dimensions to vary, five of which

are shown graphically in Figure 19; so the problem is somewhat more tedious. In most *ab initio* software packages available, a Hessian matrix is constructed. This is an $n \times n$ second derivative matrix of the potential energy with respect to all the co-ordinates being optimised. Before the frequency values can be quoted, this matrix must first be diagonalised so that only the leading entries (corresponding to the second derivative with respect to only one coordinate) have non-zero values. The algorithms used vary for different software packages.

The halide hydrogen sulfide clusters have been optimised using Möller Plesset 2nd order perturbation theory, as well as Density Functional Theory (using BHandHLYP functional) with Dunning's augmented correlation consistent polarised valence double, triple and quadruple zeta (aug-cc-pVxZ x=D and T) basis sets for the anion, and the non-augmented basis sets for the neutral (cc-pVxZ x=D, T)⁸⁰ using GAUSSIAN98.⁸¹ As the anions have an excess charge, the augmented basis set allows for more diffuse functions to describe it, but is not essential for the neutral daughter clusters. The BHandHLYP functional has been recommended for this cluster system,⁸² based on its effectiveness in producing accurate potential energy barriers in previous work.

The formation of a cluster is seen to reduce the energy of the system relative to the sum of the fragment energies. The energy at the optimised geometry of the fragments at infinite distance from one another is subtracted from the optimised structure energies

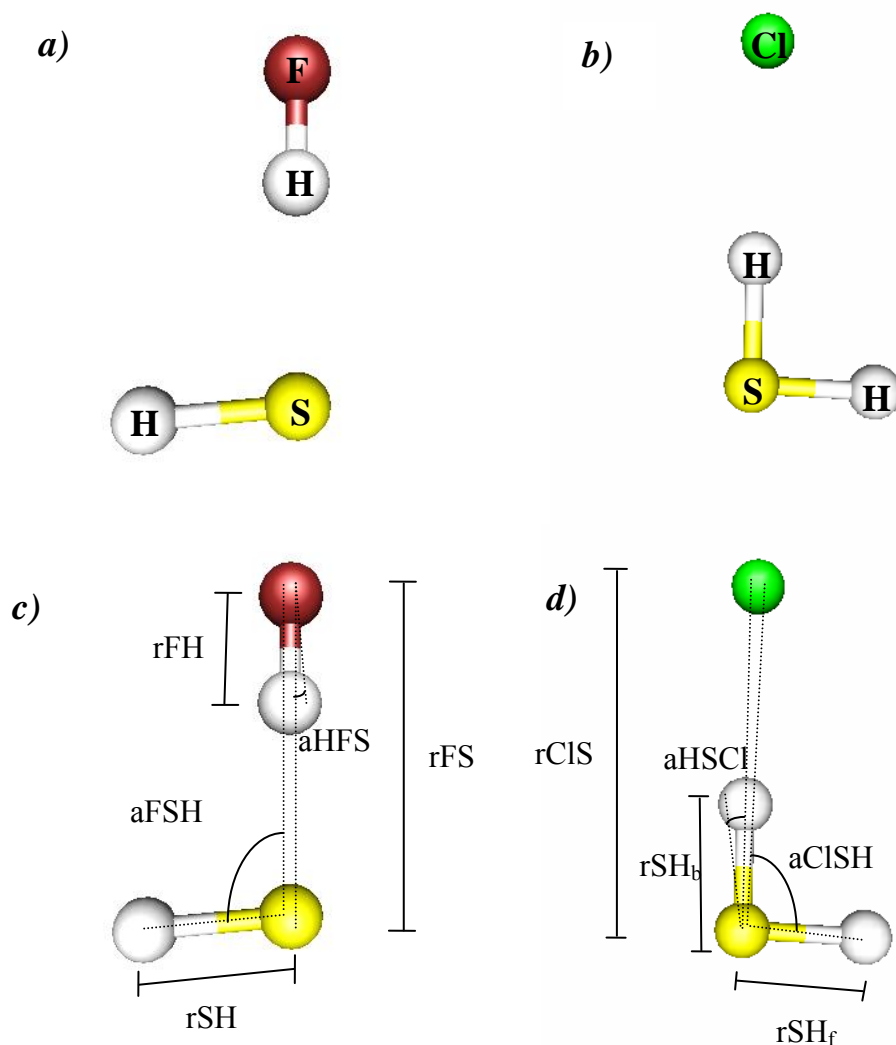


Figure 19 – Optimised geometries of clusters under study: a) Fluorine and b) Chlorine with five of the six variables c) and d) that affect the potential energy. Dihedral angle not shown for clarity

with and without zero point energy included to provide the zero point energy stabilisation as well as electronic stabilisation respectively. The two energies are provided to explore any differences allowed by the lowest energy vibrational state of the clusters and/or fragments with respect to the zero Kelvin energies. In accompaniment with these rudimentary calculations is the enthalpy of formation for both clusters according to the methods outlined by Del Bene et. al.⁸³. The stabilisation energy of the excess electron in

the solvated anion relative to the neutral has also been calculated by subtracting the electron affinity of the naked anion from the vertical detachment energy; both of which needed to be calculated. Ideally the vertical binding energy would be used in this calculation,⁷⁰ (i.e. the difference between the excess electron's kinetic energy and the vertical detachment energy), but the electron kinetic energy cannot be obtained until experiment has been performed. This stabilisation energy has therefore been approximated by the VDE, due to the relative size of the e^- kinetic energy, which is particularly low in the extremely stable halide systems.⁷⁰ The key assumption necessary for this difference to reflect the stabilisation energy of the excess electron is that the neutral cluster provides negligible stabilisation through solute-solvent interaction, which has also been explored in reference to the anionic species.

As a means of quantifying the stabilisation through cluster formation, Natural Bond Order (NBO) analyses have been performed.⁸⁴ Following methodology found in the literature along with chemical intuition, the aim has been to corroborate ionic hydrogen bond formation.⁵⁷ NBO offers a means to achieve this by calculating the population of electrons in particular orbital types. In order to quantify hydrogen bond formation, electron donation must occur from one fragment's lone pair electrons to the antibonding orbital of the corresponding fragment.⁵⁹ This suggests bond elongation of the acceptor fragment due to the reduction in bonding character, along with bond force constant reduction and a corresponding red-shift in the IR spectrum relative to the unperturbed state. In this investigation, agreement between aforementioned geometry changes and NBO analyses is considered sufficient to indicate the presence of ionic hydrogen bonds.

While it is of interest to explore the stabilisation energy of a cluster, the goal of *ab initio* photoelectron studies is to probe the stability of the anion and predict the photoelectron spectrum. In accompaniment with previously mentioned excess electron stabilisation calculations, rudimentary predictions of photoelectron spectra have been made for both halide clusters. Rather than focus solely on the anion's potential energy surface, as IR studies do, the photoelectron spectrum demands an investigation of the less stable neutral potential energy surface also. In order to infer which state of the neutral species will be accessed by photodetachment, the nature of the neutral cluster's potential energy surface must be explored, beginning with an optimisation. As the neutral cluster exists in a doublet state, (i.e. it has an unpaired electron), it is necessary to perform all the optimisation and energy calculations using an Unrestricted Hartree Fock (UHF) approximation as opposed to Restricted Hartree Fock (RHF), thereby removing the degeneracy of electrons with antiparallel spin functions in the same spatial orbital.⁸⁵

The major step in predicting a photoelectron spectrum involves comparing local portions of the anion and neutral's calculated potential energy surfaces. Using the optimised structure as a starting point, the dimensions of interest are varied and the energy calculated at each point. The key considerations here are the size of the range to be scanned, and the distance between adjacent points, or how well resolved the surface shall be. A key factor in this decision making is the computational cost; while it is useful to scan as much of the surface as possible, it is not feasible to do this at an infinite level of accuracy. One way in which the computational cost was significantly reduced was to freeze two dimensions at their optimum geometry. The FH_b and SH_f (and H_bS and SH_f

for chlorine) bond lengths were selected to remain fixed due to the low probability that their vibrational modes will be significant in the photoelectron spectrum. This assumption was made after comparison between the neutral and anion energies were made, and it was realised that the laser energy used for photodetachment is only ~5% greater than the vertical detachment energy. Due to the higher energy associated with intramolecular/intracluster vibrations, it has been hypothesised that the experimental spectrum will not in fact probe these particular modes making them unnecessary in the spectral prediction. Thus, four-dimensional hypersurfaces have been constructed which scan the bond angles and dihedral angles over a 90 degree range, whilst varying the halogen – sulfur distance 4 or 5 angstroms for the neutral and anionic cluster respectively using the same basis sets and level of theory as the optimisations for the fluoride system, but only using the MP2 theory level for the chloride system as the BHandHLYP could not locate a potential minimum on the neutral cluster's potential energy surface.

The four-dimensional surfaces have been constructed so as to aid any future advanced theoretical work aimed at predicting spectra based on a more complete hypersurface. At present this remains a challenge, with the literature straying away from four atom systems that have less than three hydrogen atoms involved.³ They can, however, act as a qualitative tool in assessing how the energy of the system is affected by the four coordinates varied. This hypersurface cannot be viewed in its entirety, but three dimensional surfaces can be constructed by fixing two variables at their equilibrium values while varying the other two and viewing the energy on the vertical axis. The surface scan data produced during the computational chemistry job are not given in such

a format so a data-extraction script needed to be developed. The Unix script which necessitates user input of the specific variables to be held constant and their values, is given in the appendix. Essentially, the names of the variables given by a user are utilised to name the output file where the data is inserted, and the values also given by the user are searched for as strings in the GAUSSIAN 98 text file output.

In order to make predictions of photoelectron spectra, and noting that the four dimensional surfaces could not be used for this purpose; highly resolved one dimensional slices of the larger hypersurface were produced for both the anionic and neutral species. By approximating the complex as a pseudo diatomic with the FH collapsed on the F and SH collapsed on the S (and the H₂S collapsed on the S for the chlorine system), photoelectron spectra have been predicted. LeRoy's LEVEL software package⁸⁶ uses one dimensional potential energy surfaces to calculate vibrational wavefunctions by solving the radial Schrödinger equation. By also inputting the neutral potential energy surface, the vibrational wavefunctions for both surfaces can be used to calculate overlap integrals or Franck-Condon factors which directly reflect the probability of a transition. In performing this calculation, only the first two vibrational energy levels of the anion are occupied, therefore allowing for only one 'hot-band' assumption that in the actual experimental setup, the pulsed nozzle in conjunction with the argon buffer gas will sufficiently cool the vibrational temperature⁵⁷ of the cluster so that it occupies low energy states.

The Franck-Condon factors have been subject to a vibrational partition function calibration⁴ to reflect the population of the $\nu=0$ and $\nu=1$ vibrational energy levels at 50 K, which is noted as the conventional temperature accessed by supersonic expansion.⁸⁷ In this way the predicted spectra also account for the thermal population of the vibrational energy levels in the anion during a typical experiment.

One-dimensional potential energy slices of the bending potentials have also been constructed with one degree resolution over a 360° and 320° range for the fluoride and chloride complexes respectively. A lower range has been sampled for the chloride, to avoid the high potential of two extremely close protons in H_2S . These bending potentials could not be used to predict photoelectron spectra by the same method as the intermolecular stretching potential energy surface, as the LEVEL software package is used to solve the radial Schrödinger equation (i.e. not the angular).

3.2 Cluster Geometries, NBO analyses and Energies

3.2.1 FH...SH

The optimised geometry of the fluoride hydrogen sulfide dimer along with absolute energy, dissociation energy and enthalpy of formation is presented in Table 1 with the structure shown graphically in Figure 19. It is clear that both the anionic and neutral fluoride cluster exist in a charge transfer state, where the proton has donated from the H_2S moiety to the fluoride ion as well as the fluorine atom. The results for the anion at the MP2 level of theory have been noted previously,⁵⁹ but not with additional information

from DFT studies, as well as the extra data pertinent to the neutral cluster at both MP2 and DFT levels of theory. It can be seen that the DFT methodology gives similar dimensions to MP2 with bond distances varying by at most 0.025 Å and angles by 2° making it an attractive alternative due to its computational efficiency. The triple zeta basis set is acknowledged as allowing the cluster more flexibility in terms of calculating the wavefunction and energy of the state, but for this cluster the double zeta basis set provides acceptable results comparable to the TZ basis, based on low maximal bond length and angle discrepancies (0.07 Å and 3.2°).

The fragment data allows a direct comparison with the cluster subunit geometries and vibrational characteristics. For both the anionic and neutral cluster, at all levels of theory for all basis sets used, the rFH bond length is seen to increase upon complexation with the SH. This elongation is much less for the neutral, relative to the anion (c.f. 0.072 Å and 0.009 Å at MP2/pVTZ), reflecting the greater stability afforded to the anion. This argument is consolidated when considering the difference in formation enthalpy for the anion and neutral (-132 vs. -18.4 kJ.mol⁻¹ respectively at MP2/pVTZ). This can be attributed to the stabilisation of the anion fragment's excess charge by the FH moiety through an ionic hydrogen bond, compared to the reactive charge neutral radical. These bonding differences have been quantified in Table 2, which offers the results of NBO analyses. It can be seen that in the anion, the FH has 118 millielectrons in its antibonding orbital, indicative of an ionic bond formed with the anionic SH moiety. This is considerably less in the neutral cluster (14 me), reflecting the lower stability afforded by this weak (and not ionic) hydrogen bond. The subsequent results in Table 2 show that the

	MP2	BHandHLYP	[MP2-DFT]		uMP2	uBHandHLYP	[MP2-DFT]
ANIONS				NEUTRALS			
FH_b...SH_f⁻				FH_b...SH_f			
rFS	2.954 (0.013)	2.979 (0.007)	0.025	rFS	3.247 (0.072)	3.243 (0.001)	0.004
rFH _b	0.990	0.968 (0.003)	0.022	rFH _b	0.927 (0.002)	0.919 (0.002)	0.008
rSH _f	1.340 (0.01)	1.337 (0.11)	0.003	rSH _f	1.340 (0.01)	1.339 (0.012)	0.001
aH _b FS	0.5 (0.1)	0.6	0.1	aH _b FS	93.5 (2.6)	93.6 (2.8)	0.1
aFSH _f	94.6 (0.7)	96.6(0.2)	2	aFSH _f	3.1 (3)	2.9 (3.2)	0.2
dH	0	0	0	dH	0	0	0
ω ₁	2833 3014 a'	3059 2794 a'		ω ₁	3980 677 a'	4059 743 a'	
ω ₂	2737 69 a'	2739 51 a'		ω ₂	2759 0.9 a'	2759 0.2 a'	
ω ₃	990 25 a'	947 36 a'		ω ₃	537 77 a'	539 82 a'	
ω ₄	304 11 a'	305 11 a'		ω ₄	172 40 a'	174 41 a'	
ω ₅	247 29 a'	238 25 a'		ω ₅	136 0.9 a'	139 0.9 a'	
ω ₆	884 23 a"	867 34 a"		ω ₆	364 112 a"	355 120 a"	
E _e	-498.724857	-499.325265		E _e	-498.595551	-499.213083	
ZPE	0.018212	0.018643		ZPE	0.020229	0.018283	
D _e	-31.2	-26.5		D _e	-4.6	-4.7	
D _e + ZPE	-29.6	-24.8		D _e + ZPE	-3.1	-3.3	
ΔH _{0→1}	-31.4	-26.6			-4.4	-4.6	
SH⁻				SH			
rSH	1.3423 (0.014)	1.3384 (0.011)	0.004	rSH	1.339 (0.013)	1.338 (0.013)	
ω ₁	2717 65 σ _g	2722 71 σ _g		ω ₁	2764 0 σ _g	2763 1 σ _g	
E _e	-398.345321	-398.839536		E _e	-398.258440	-398.762080	
ZPE	0.006189	0.006200		ZPE	0.008402	0.006294	
HF							
rHF	0.918	0.910	0.008				
ω ₁	4179 113 σ _g	4277 128 σ _g					
E _e	-100.329786	-100.443460					
ZPE	0.009521	0.009743					
Cl⁻...H_bSH_f				Cl...H_bSH_f			
rClS	3.397 (0.008)			rClS	4.2902 (0.106)		
rSH _b	1.407 (0.005)			rSH _b	1.3357 (0.011)		
rSH _f	1.336 (0.013)			rSH _f	1.3352 (0.012)		
aH _b SCI	0.8 (0.2)			aH _b SCI	93.5 (2.2)		
aClSH _f	91.5 (0.2)			aClSH _f	1.2		
dH	0			dH	0		
ω ₁	2777 3.1 a'			ω ₁	2797 4 a'		
ω ₂	1941 2938 a'			ω ₂	2778 5 a'		
ω ₃	1194 6 a'			ω ₃	1212 1 a'		
ω ₄	328 6 a'			ω ₄	42 0 a'		
ω ₅	169 100 a'			ω ₅	17 14.4 a'		
ω ₆	626 0.9 a"			ω ₆	51 15 a"		
E _e	-858.712218			E _e	-858.549982		
ZPE	0.016027			ZPE	0.017597		
D _e	-17.4			D _e	-0.7		
D _e + ZPE	-17.1			D _e + ZPE	0.7		
ΔH _{0→1}	-17.8			ΔH _{0→1}	0.8		
Cl⁻				Cl			
E _e	-459.780792			E _e	-459.645241		
H₂S							
rSH	1.3352						
aHSH	92.2						
ω ₁	2780 0 a1						
ω ₂	1211 1 a1						
ω ₃	2799 0 b2						
E _e	-398.903648						
ZPE	0.015467						

Table 1 – Optimised structures and energies for F and Cl clusters and fragments. Subscripts of b and f indicate hydrogen bound and free hydrogen respectively. Bond distances are in angstroms, angles in degrees. Structures are given at the pVTZ level of theory, with pVDZ values in brackets. Electronic and zero point energies (ZPE) are given in Hartree. Dissociation energies and enthalpy of formation (at 298 K) are given in kJ.mol⁻¹. Vibrational frequencies are quoted in wavenumbers, with the bold indicating intensity in km.mol⁻¹.

population in the antibonding orbital is not a naturally occurring effect for the FH at the cluster geometry, nor a polarisation effect due to an excess charge.

	MP2/uMP2		BHandHLYP/uBHandHLYP	
	pVDZ (me)	pVTZ (me)	pVDZ (me)	pVTZ (me)
FH_b σ* occupancy				
FH...SH ⁻	121	118	123	116
FH...SH	12	14	18	16
FH (a-geometry)	0	0	0	0
FH...q	0	0	0	0
FH (n-geometry)	0	0	0	0
H_bS σ* occupancy				
Cl ⁻ ...H _b SH _f	95	101		
Cl...H _b SH _f	1	2		
H ₂ S (a-geometry)	1	2		
H ₂ S...q	1	2		
H ₂ S (n-geometry)	1	2		
H_fS σ* occupancy				
Cl-...H _b SH _f	1	1.3		
Cl...H _b SH _f	1	1		
H ₂ S (a-geometry)	1	2		
H ₂ S...q	1	1		
H ₂ S (n-geometry)	1	2		

Table 2 – Natural bond order values for the F and Cl clusters and fragments in milli electrons (me) to verify hydrogen bond formation. To ensure it is an effect of cluster formation and not charge polarisation, analysis of fragments in the presence of a charge q have also been performed.

Provided in Table 3 are system energetic values hoped to be verified by experimental photoelectron spectroscopy. It is fortunate that the VDE at all the levels of theory is less than the laser energy (345 kJ/mol at MP2/pVTZ compared to 450 kJ/mol or 266 nm), allowing the neutral state to actually be accessed in experiment. Based on the low dissociation energy of the neutral, as mentioned in the computational methods section, the net electrostatic stabilisation energy of the solvated halide has been calculated and found to be on the same order as the enthalpy of formation (130 kJ/mol)

Spectral Data			
	MP2	BHandHLYP	 MP2-DFT
FH...SH	pVTZ	pVTZ	
VDE	345	295	50
EA_a	359	305	54
EA(SH)	234	204	30
E(stab)	130	101	29
Cl...HSH			
VDE	426		
EA_a	462		
EA(Cl)	356		
E(stab)	106		

Table 3 – Some energetic data in kJ/mol to be verified experimentally

3.2.2 Cl...HSH

The optimised geometry of the chloride hydrogen sulfide dimer along with absolute energy, dissociation energy and enthalpy of formation is presented in Table 1 with the structure shown graphically in Figure 19. BHandHLYP methods could not converge at a minimum for the chlorine neutral and based on this result have not been considered for subsequent energetic calculations and spectral predictions. In the case of the anion, the DZ basis set provides little variation from that of the TZ (max 0.013 Å and 0.2°), and calculations may be made at this level. The neutral possesses a higher variation of 0.1 Å and 2°, but this is also considered acceptable based on the relative amount of variation.

For both the anionic and neutral cluster, at all levels of theory for all basis sets used, the r_{SH_b} bond length is seen to increase upon complexation with the Cl. This elongation is much less for the neutral, relative to the anion (c.f. 0.072 and 0.001 Å at MP2/pVTZ), reflecting the greater stability of the anion. This argument is affirmed when considering the difference in formation enthalpy for the anion and neutral (-74.5 vs. 3.4 kJ.mol⁻¹ respectively at MP2/pVTZ). The neutral cluster formation is actually an endothermic process at this level of theory! The formation enthalpy of the anion can be attributed to the stabilisation of the chloride fragment's excess charge by the HSH molecule through an ionic hydrogen bond, compared to the extremely unstable neutral radical. These bonding differences have been quantified in Table 2, which offers the results of NBO analyses. It can be seen that in the anion, the SH_b has 101 *me* in its antibonding orbital, indicative of an ionic bond formed with the anionic Cl moiety. This is extremely reduced in the neutral cluster (1 *me*), reflecting the lower stability afforded by this extremely

weak (and not ionic) hydrogen bond. The subsequent results in Table 2 show that the population in the antibonding orbital is not a naturally occurring effect for the Cl^- at the cluster geometry, nor a polarisation effect due to an excess charge.

Provided in Table 3 are system energetic values hoped to be verified by experimental photoelectron spectroscopy. For the chloride cluster the VDE using both bases is just less than the laser energy (426 kJ/mol at MP2/pVTZ compared to 450 kJ/mol or 266nm), allowing the neutral state to just be accessed in experiment. Based on the low dissociation energy of the neutral, as mentioned in the computational methods section, the net electrostatic stabilisation energy of the solvated halide has been calculated and found to be of much greater significance to the chlorinated system than it was for fluorine (106 kJ.mol⁻¹ c.f. enthalpy of formation of 74.5 kJ.mol⁻¹)

3.3 Four Dimensional Potential Energy Scans

3.3.1 FH....SH

The six possible two dimensional plots for the FH...SH system at the pVDZ/pVTZ and MP2/BHandHLYP levels of theory can be found in the electronic supplementary information. As noted in the computational methods, their use in the context of this study is to qualitatively assess the effect that particular variables have on the potential energy, as well as allowing for a comparison of the effectiveness of the levels of theory and basis sets employed.

The anionic cluster potential energy surfaces are quite aesthetically pleasing, each clearly showing the smooth progressions that particular variables have on the cluster energy. It is important to note that the dihedral angle is seen to have no effect on the potential energy surface even as one other variable is altered, except in the case of the aHFS angle where the equilibrium dihedral becomes repulsive as the ionic hydrogen bond angle is varied. This is to be contrasted with the neutral cluster's potential surfaces which are not nearly as smooth, only when the dihedral angle is being varied as the two plots of rFS vs. dH show in Figure 20. The influence of the dihedral angle is therefore much greater in the unstable neutral, and may be contributing to the energy converging on an excited state potential surface which could account for the discontinuities in the neutral surface shown. This tendency to converge on an excited state surface is not as significant an issue for the anionic state,¹ which in turn accounts for the continuities of its surfaces.

In comparing levels of theory, at a qualitative level the anion is modelled well using density functional methods in accompaniment with the lowest double zeta basis set. This is not the case for the neutral however, as all the surfaces constructed with the double zeta basis set lack any consistent structure or intuitive variation in potential energy. In fact, for the BHandHLYP/pVDZ and MP2/pVDZ potential surfaces of aFSH vs. rFS, the lowest state energy is not consistent with the optimised geometry. This anomalous result is not present in the analogous MP2/pVTZ and BHandHLYP/pVTZ surfaces (see Figure 21), suggesting that the problem is an artefact of basis set choice. Following this logic it is possible that the problematic surfaces at pVTZ basis set level could be repaired by higher level basis sets (e.g. pVQZ or pV5Z). Based on qualitatively comparable results

between the BHandHLYP and MP2 levels of theory, it seems that DFT studies act as a suitable alternative to the computationally taxing higher levels of theory.

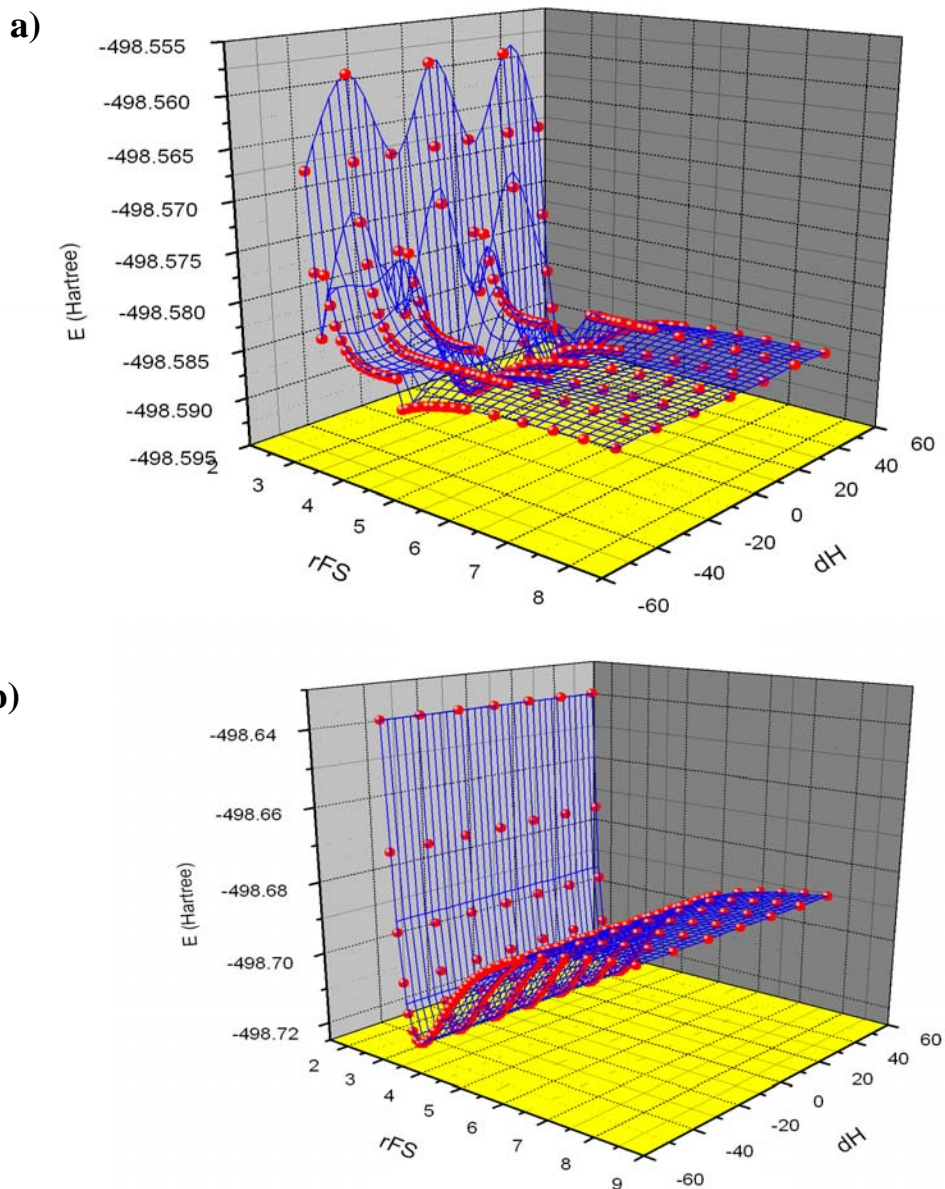


Figure 20 – a) neutral compared to b) anion potential surface for the intermolecular distance versus dihedral angle of $FH...SH$ at the MP2/pVTZ level of theory

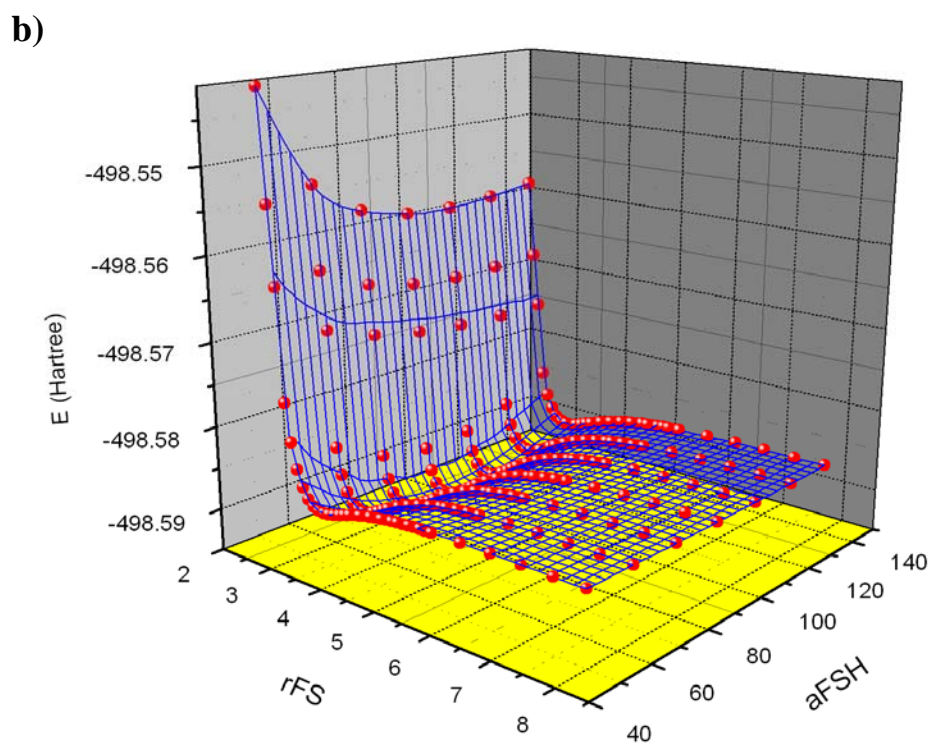
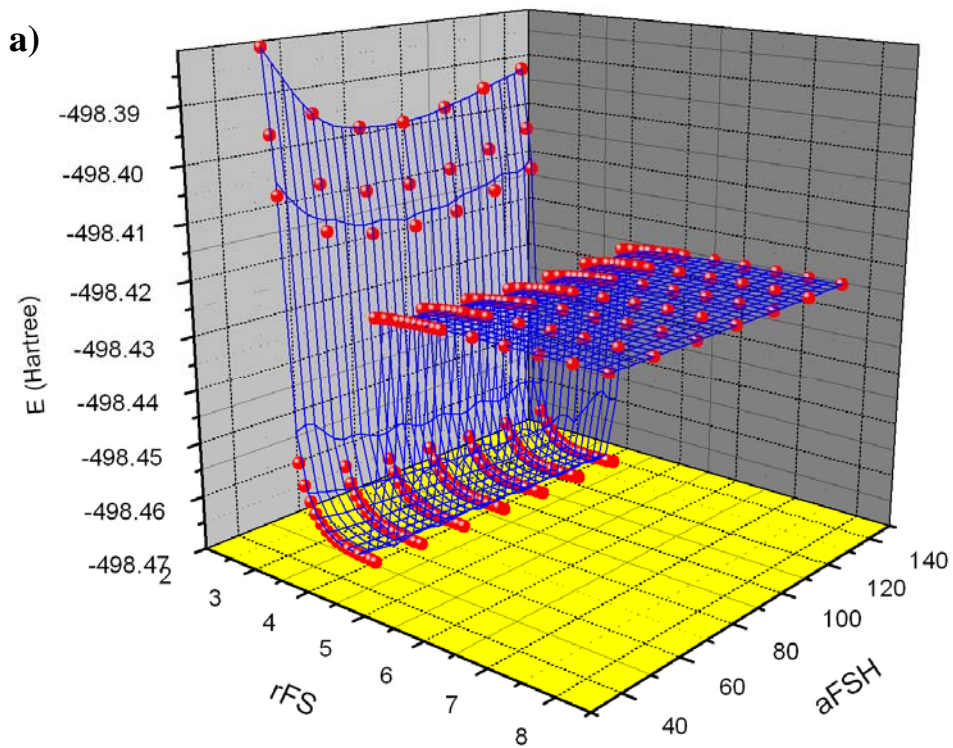


Figure 21 – Improvement in potential surface achieved in going from using the a) pVDZ basis set to b) pVTZ for the FH...SH system

3.3.2 Cl...HSH

As with the fluorinated cluster, the four dimensional plots provide a general qualitative insight into the variation of the potential energy of the cluster with respect to its dimensions. For the chloride anion the qualitative variation is seen to be analogous to that of the fluoride. Also like the fluorine cluster, the neutral chlorine complex produced anomalous energies that do not fit the functional form of the remaining potential energy surface. It is interesting and counter intuitive that in all instances the pVDZ basis set provides better or comparable potential surface quality than the pVTZ (see Figure 22). The anomalous points on the pVTZ surface have a continuity about them, which suggests they may form part of an excited state surface. However, given that this occurs in the pVTZ surface, not the pVDZ, this cannot be confirmed with any certainty. A feature of the surface which contradicts this suggestion is the fact that the high energy values occur at lower rClS separations. It is therefore also possible that the higher energy region is in fact the repulsive wall of the intermolecular stretch. There is clearly a need for further investigations of this surface at higher basis set levels, or at least the same basis set with better resolution.

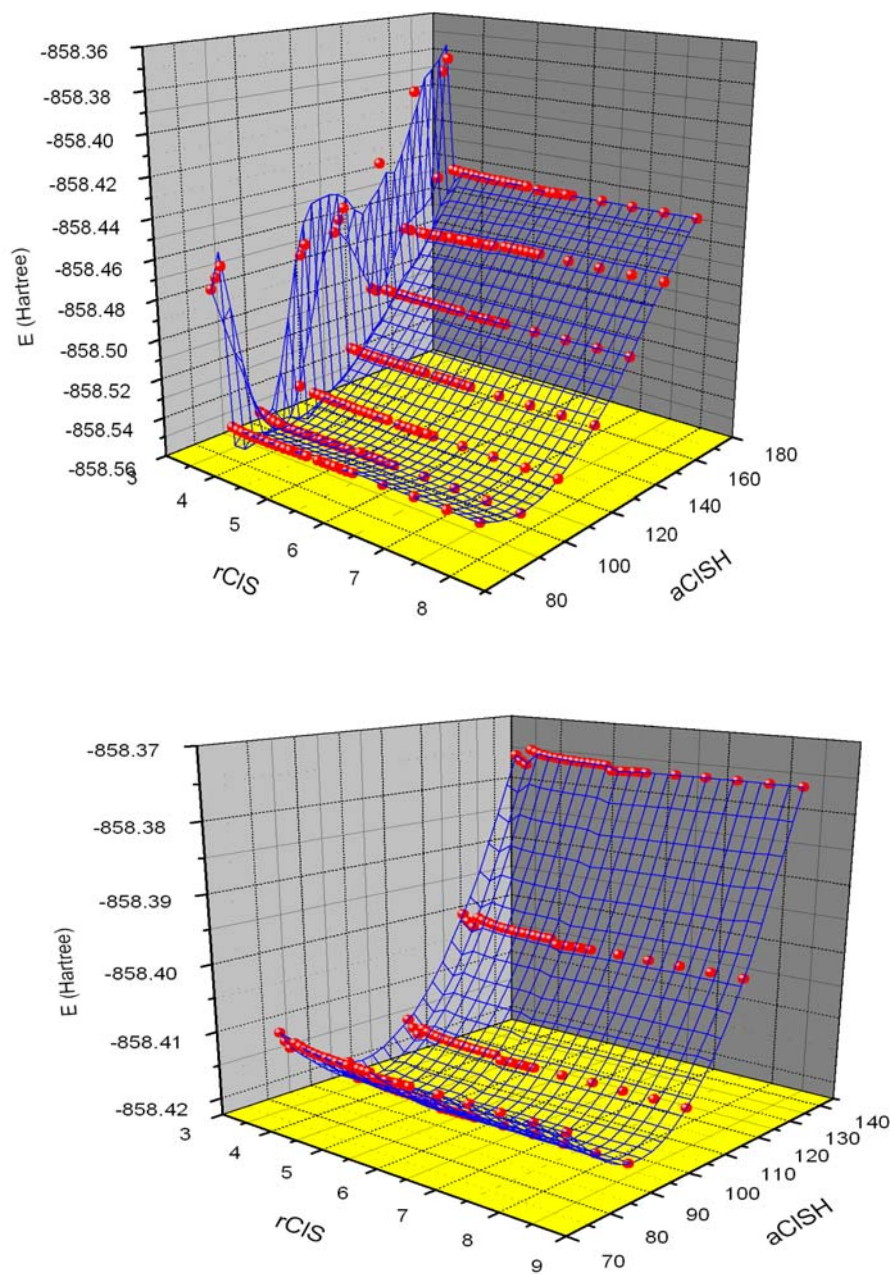


Figure 22 – Comparing the quality of neutral Cl...HSH potential surfaces produced from a) cc-pVTZ and b) cc-pVDZ basis sets

3.4 One Dimensional Potential Energy Slices

3.4.1 FH...SH

One dimensional slices of the six dimensional hypersurface at improved resolution of 0.01Å and 1° for intermolecular stretches and bending potentials respectively have been calculated for both clusters, and are available in the electronic supplementary information. They provide perhaps a more detailed understanding of how altering but one variable affects the potential energy of the system. In the variation of the angle of the bridging proton, aHFS, there exists a clear minimum at the equilibrium geometry as intuition would suggest. For the other proton however, the potential appears more like a double well, due to the near linear FH...S component of the molecule, making the analogous reflected state of aFSH a minimum also as Figure shows. Note also the high potential at zero degrees which corresponds to the linear repulsion from the two protons. The one dimensional dihedral variation is in agreement with the four dimensional data in that it show very little variation of energy with dH in the anion state, and a slightly greater energy dependence in the case of the neutral as Figure 24 shows.

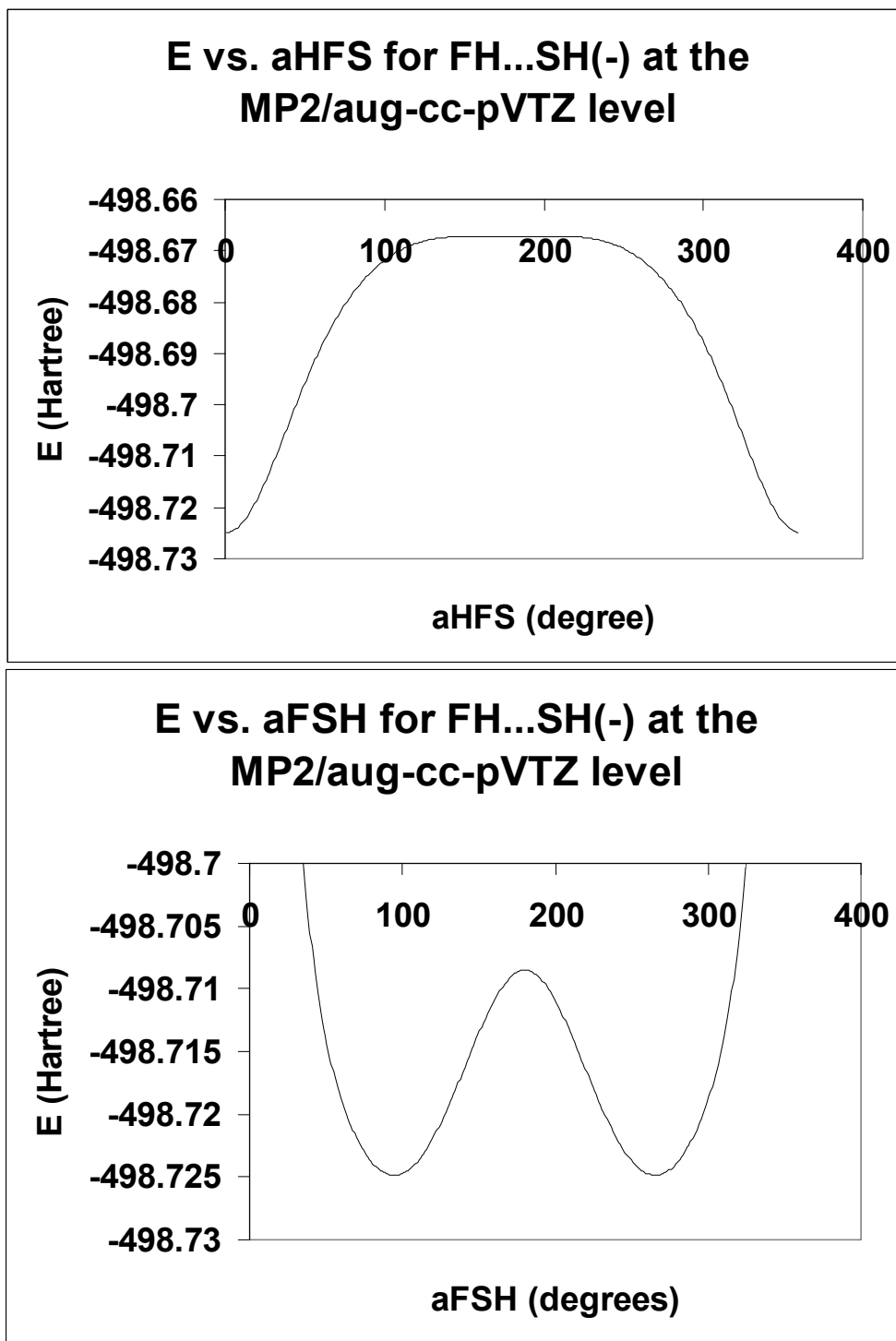


Figure 23 – One dimensional slices of the FH...SH hypersurface illustrating a) aHFS and b) aFSH effects

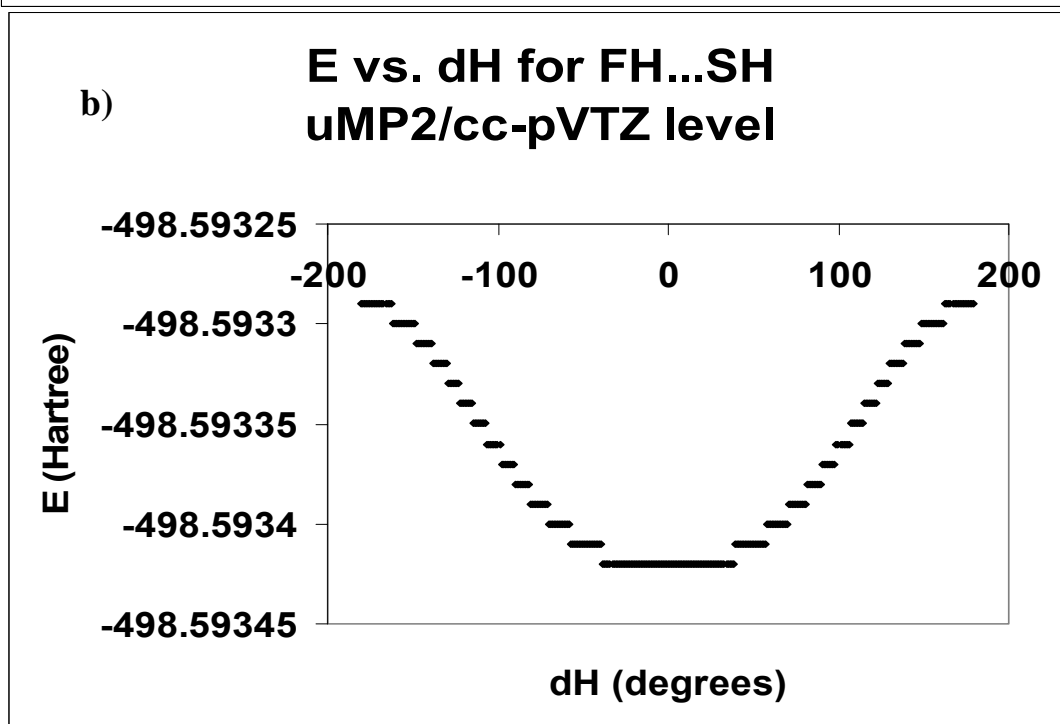
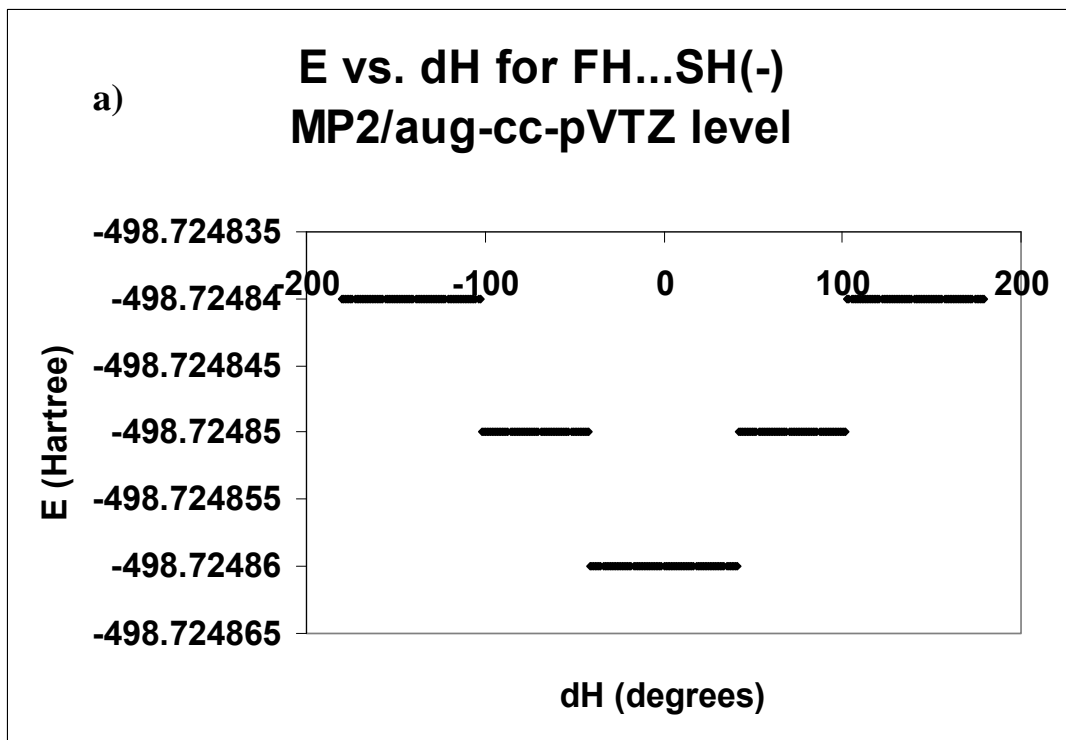


Figure 24 – Dihedral angle affects the energy of the FH...SH system less in the a) anion as opposed to b) neutral

3.4.2 Cl...HSH

In near perfect analogy to the FH...SH system, the Chlorine system's free proton forms a double potential well as Figure 25 shows for the neutral cluster at the pVDZ level. A curious difference is noted in the potential with respect to the bridging proton at this same theory level, in which there exists another double potential. This supports the low interaction of the chlorine system's cluster fragments in the neutral case. The extra minimum can be attributed to the stability the H₂S moiety obtains from a bent geometry that is a reflection of its optimised state. The tendency to infinity at approximately 90° is due to the proximity of the two protons in the H₂S.

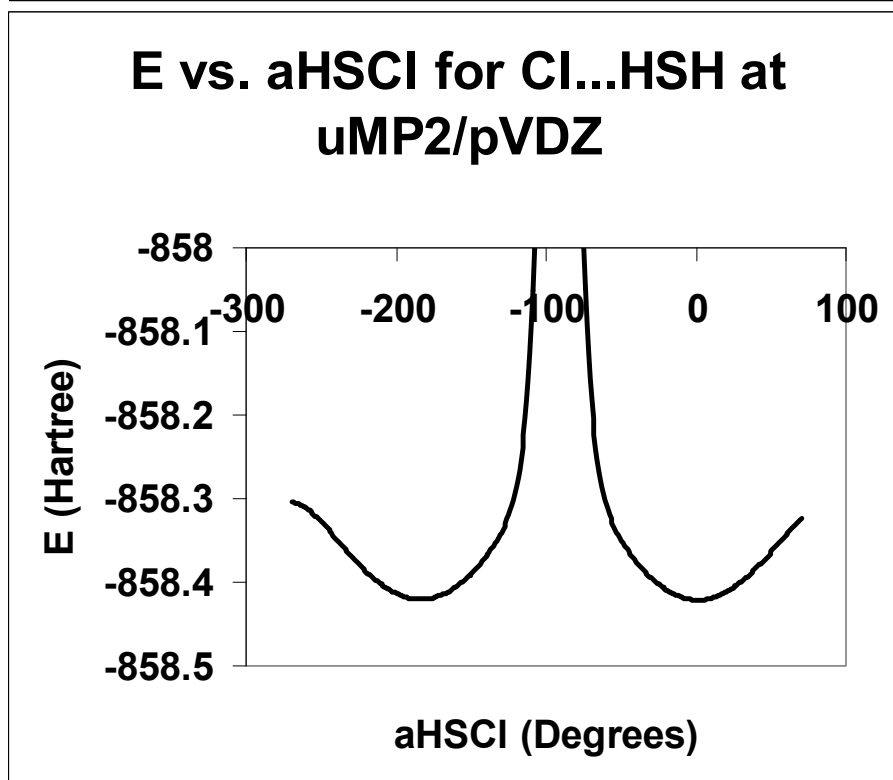
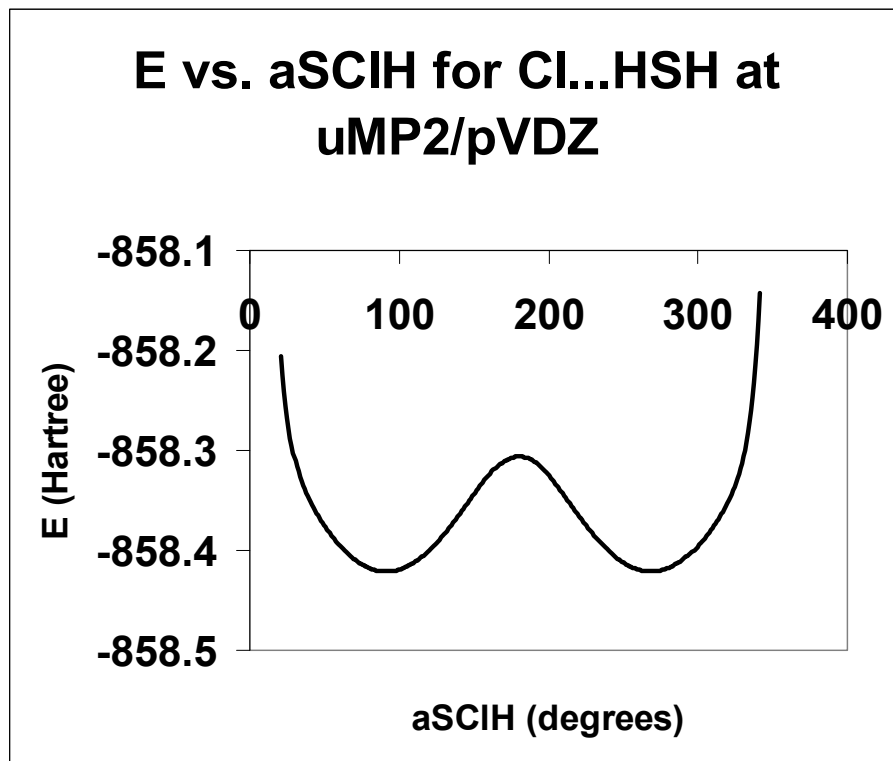


Figure 25 - One dimensional slices of the Cl...HSH hypersurface illustrating
a) aHSCI and b) aSCIH effects

3.5 Predicted Spectra

3.5.1 FH...SH

The particular one dimensional slice used for the photoelectron spectrum prediction is the intermolecular stretch r_{XS} , which depends on the solution of the vibrational wavefunction for the anion and neutral clusters so that their functional overlap or Franck-Condon factor can be calculated. The vibrational wavefunctions for the anionic and neutral clusters at the MP2/pVTZ theory with one dimensional potential energy slices are presented in Figure 26. The reduced energies of the neutral cluster's vibrational levels are in agreement with the energetic data from section 3.2 that the potential of the neutral is shallow relative to the anion, i.e. its dissociation energy is less. To reinforce that there will not be a perfect overlap between these functions, the anion and neutral intermolecular stretch potentials have been presented together in Figure 27. The resulting predicted spectrum with thermal vibration partition correction for the MP2/pVDZ and MP2/pVTZ basis sets are given in Figure 28. All figures and tables of values for both theory levels and basis sets used are available in the electronic supplementary information.

The actual energies of the x-axis are not necessarily as important as the structure of the spectrum. In fact, the absolute energies of transition do not correlate exactly between different theory levels or basis sets, yet what should be consistent is the most probable transition. At the MP2 theory level, pVDZ basis set usage suggests the $3 \leftarrow 0$ transition, while pVTZ shows $4 \leftarrow 0$; both calculate these two transitions collectively as the most probable, but with order reversed. The DFT spectra both concur with a $2 \leftarrow 0$ transition

primarily, followed by $3 \leftarrow 0$. All results show a degree of spectral agreement visually, but based on these results a conclusive suggestion as to which transition is most probable cannot be given. Nonetheless, these results do suggest that a spectrum should be obtained that shows maximum signals for electron binding energies in the range $2 \leftarrow 0$ through to $4 \leftarrow 0$.

It is interesting to note that for the hot band progression from the $v=1$ vibrational level, the progression is not of the same structure, owing to the different functional form of its wavefunction. To contrast, the $4 \leftarrow 1$ transition is least likely for the MP2/pVTZ spectrum compared to third most prominent for the $v=0$ transitions.

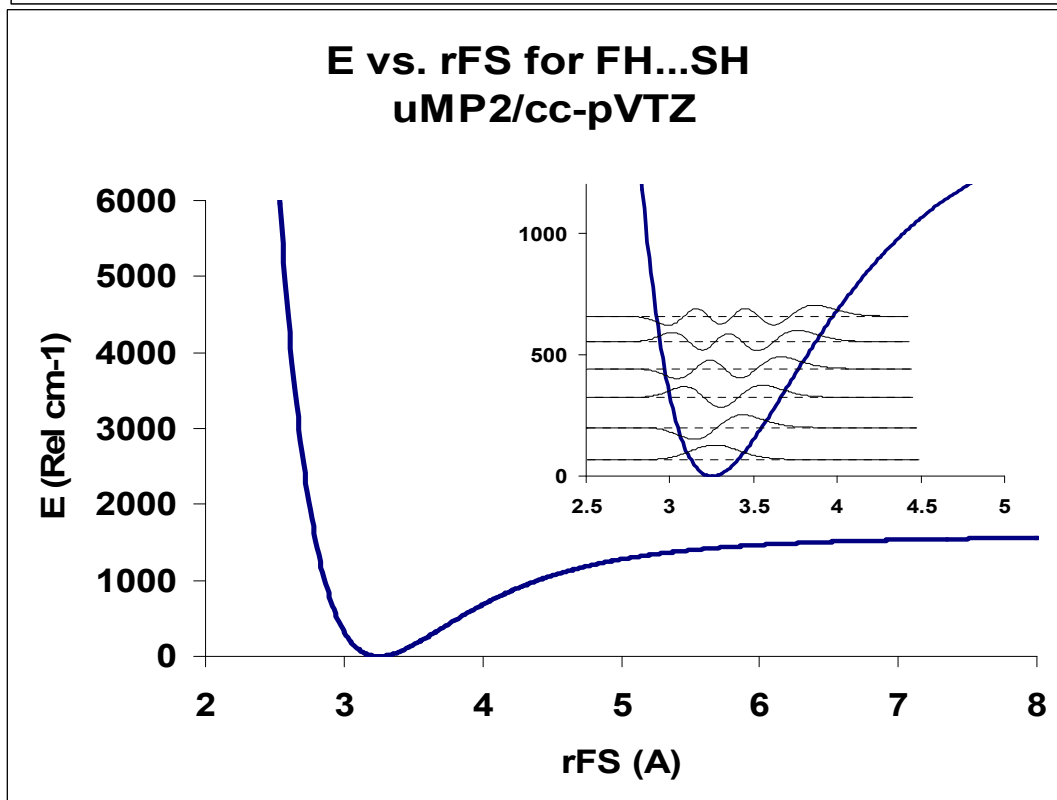
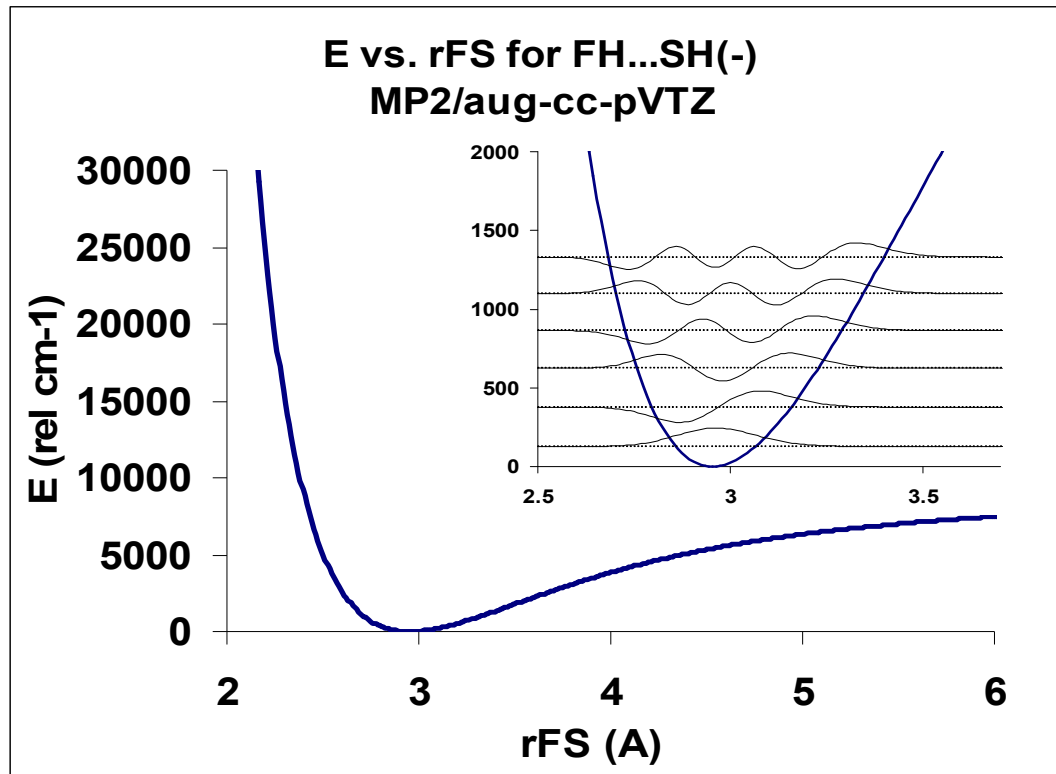


Figure 26 – One dimensional potential energy slices for FH...SH system at MP2/pVTZ level of theory, with vibrational wavefunctions in the inset

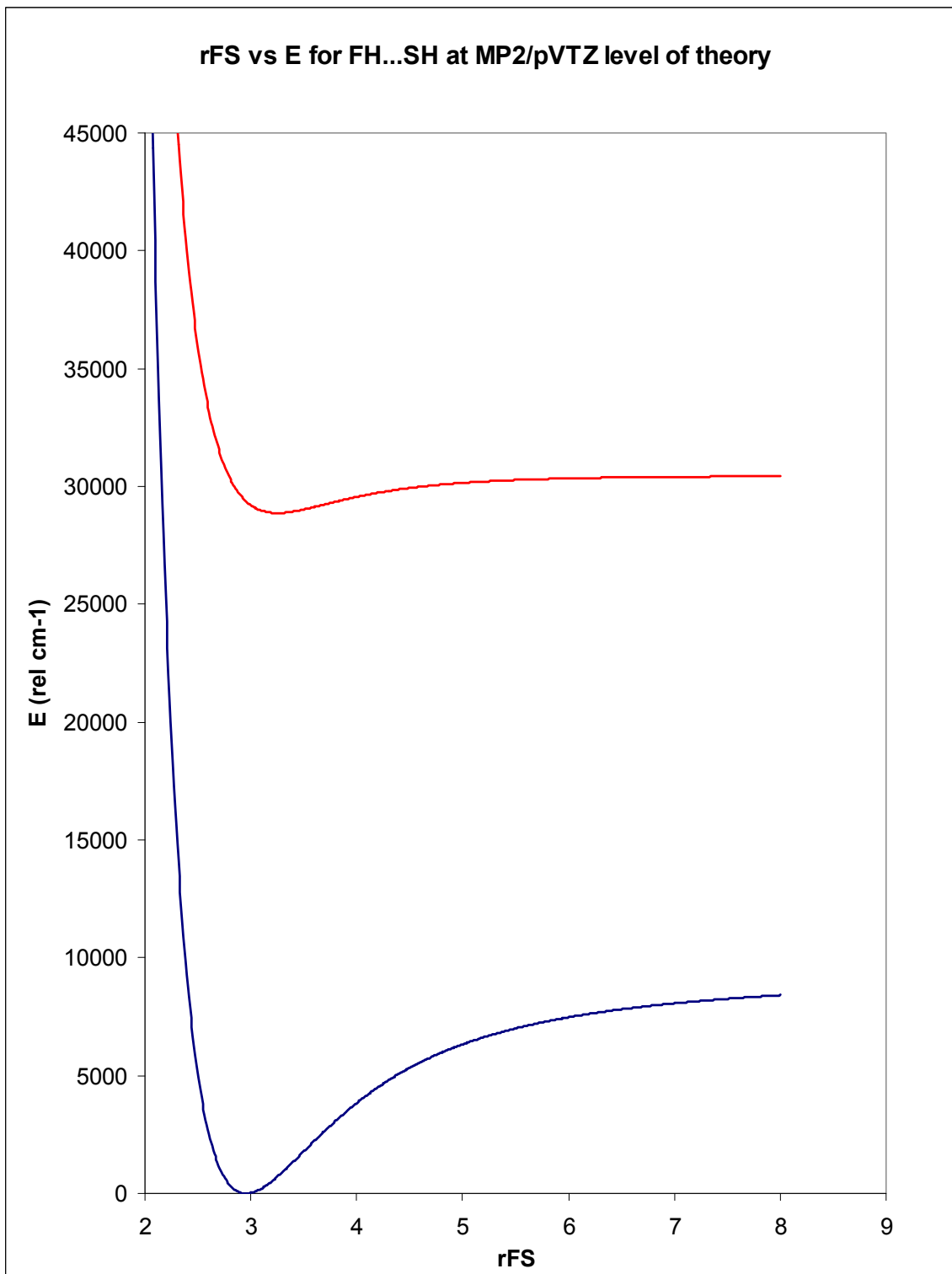


Figure 27 – One dimensional potential energy slices for the FH...SH cluster at the MP2/pVTZ level of theory

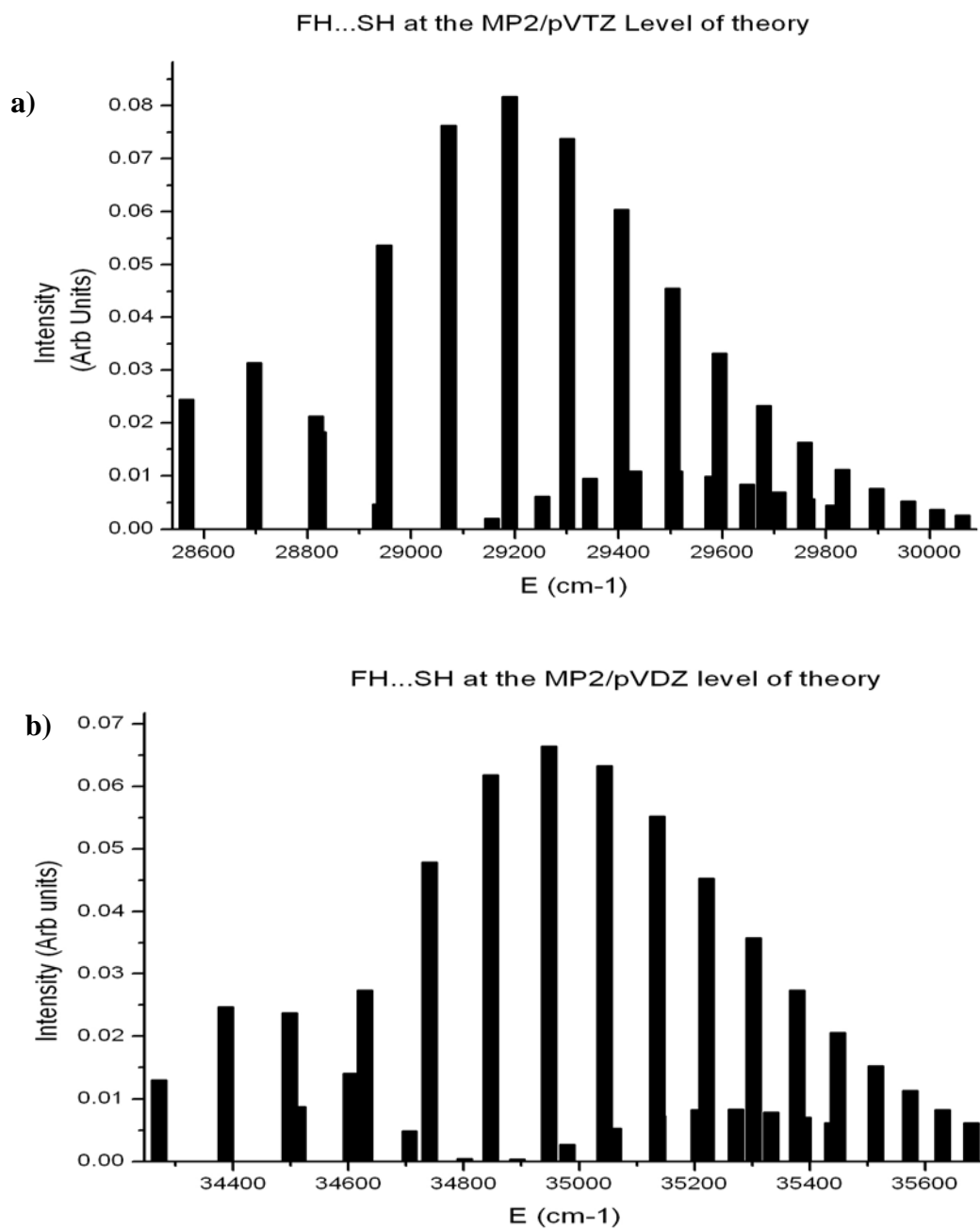


Figure 28 – Predicted photoelectron system for FH...SH using a) pVTZ and b) pVDZ basis sets

3.5.2 Cl...HSH

The vibrational wavefunctions for the chlorine clusters at the MP2/pVTZ theory in conjunction with their one dimensional scans are presented in Figure 29. The lower energies of the neutral cluster's vibrational levels are also in agreement with energetic data from section 3.2 that the potential of the neutral is shallow relative to the anion, i.e. its dissociation energy is less. In direct comparison with the fluorine system, it is realised that both the chloride and chlorine have more shallow potentials which also concurs with the energetic data that the formation enthalpy is less exothermic for the Cl...HSH clusters. The chlorine neutral in particular is especially shallow, with a $v=0$ energy of approximately 18 cm^{-1} . This particularly shallow potential is perhaps one of the key reasons why the BHandHLYP functional could not locate a minimum. It is probable that transition states were more easily located due to their relative energetic environment being less flat.

Compared to the fluorine system, the chlorine cluster suggests even less overlap between the same states in the anion and neutral, as intuited from Figure 30. Like the fluorine, this figure shows an offset to greater intermolecular distance for the neutral's minimum, but to a much greater extent. The predicted spectrum with thermal vibration partition correction for the MP2/pVDZ and MP2/pVTZ basis sets are given in Figure 31. All figures and tables of values for both basis sets used are available in the electronic supplementary information.

In this instance, the absolute energies of transition again do not correlate exactly between different basis sets, yet what should be consistent is the most probable transition. Due to the greater extent of geometrical difference at equilibrium, the trend is towards higher energy states compared to fluorine. The other interesting feature to note is that it is the hot band from $v=1$ which provides the greatest intensity of transition. The pVDZ basis set suggests the greatest overlap for the $6\leftarrow 1$ and $7\leftarrow 1$ transitions, whereas the pVTZ shows very slight discrepancy, favouring $7\leftarrow 1$ and $8\leftarrow 1$. These results have a beautiful spectral agreement, with the form nearing exact overlap. An exact transition cannot be predicted for this spectrum either, but it is suggested that high intensity signals for the hot band electron binding energies $6\leftarrow 1$ through to $8\leftarrow 1$ should be obtained.

It is particularly fascinating to compare the transitions from the first vibrational energy level for the fluorine and chlorine systems. Those transitions which were most favourable in the fluorine spectrum provide some of the lowest signals for the chlorine. This difference clearly highlights the influence of equilibrium structure variation between two highly analogous systems. Irrespective of the same qualitative types of interactions at play, the greater quantitative variation in equilibrium intermolecular distance for the chlorine system ensures that their respective photoelectron spectra are particularly different.

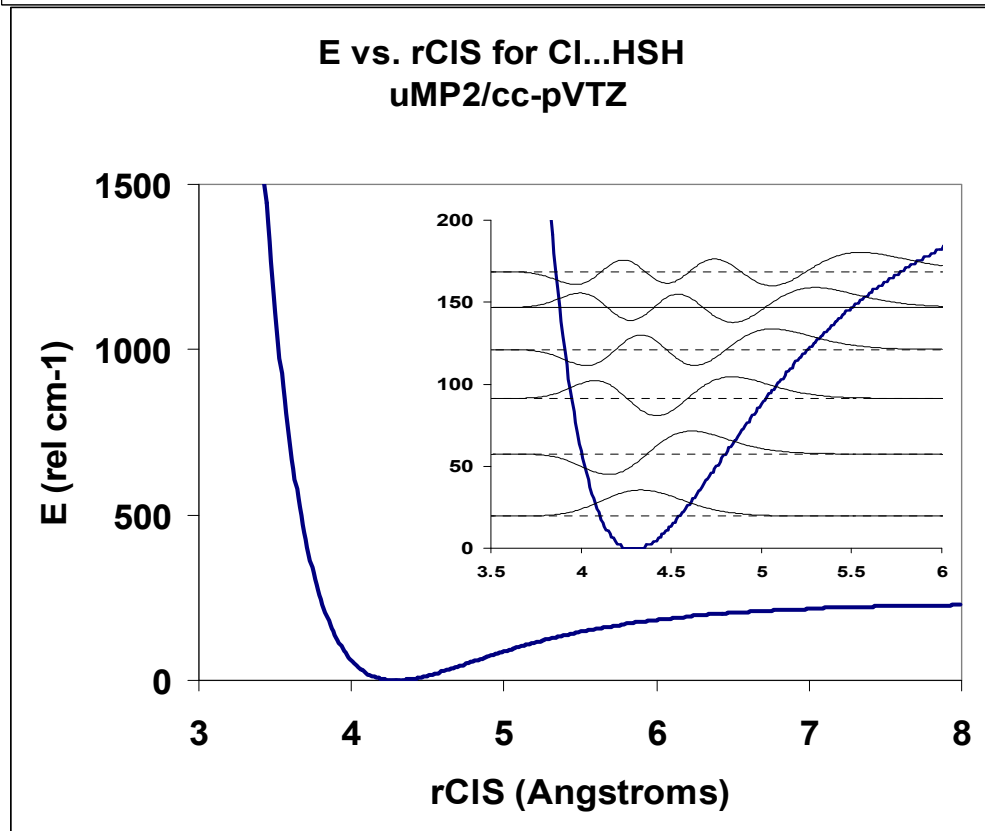
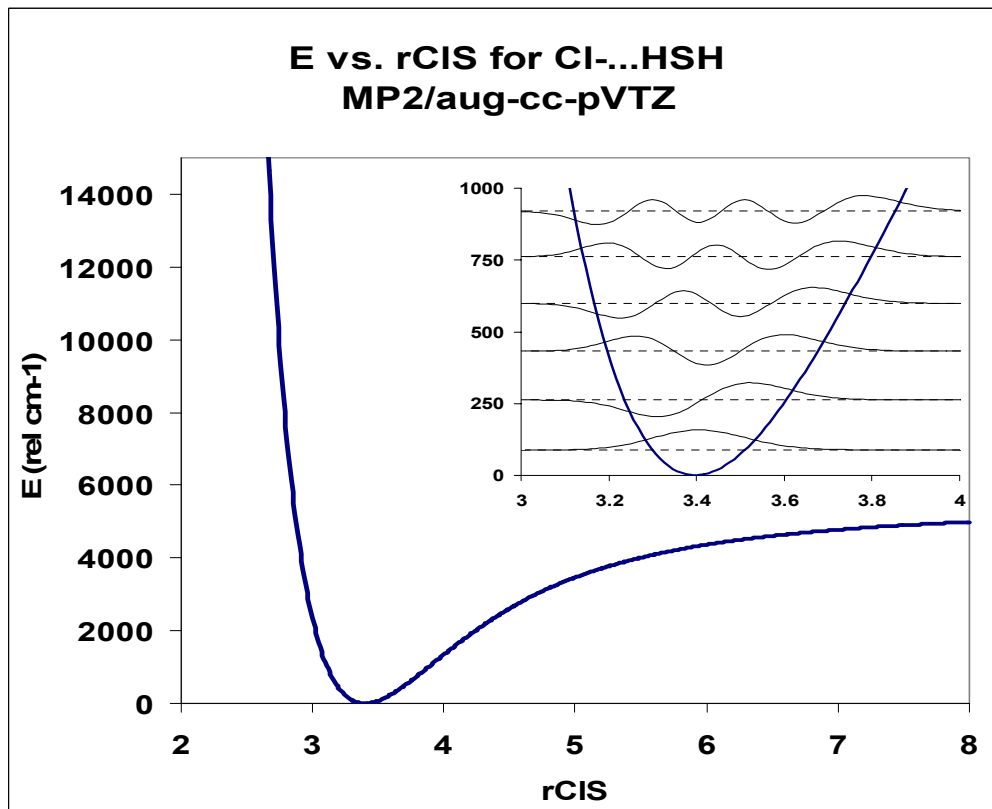


Figure 29 – One dimensional potential energy slices for Cl...HSH system at MP2/pVTZ level of theory, with vibrational wavefunctions in the inset

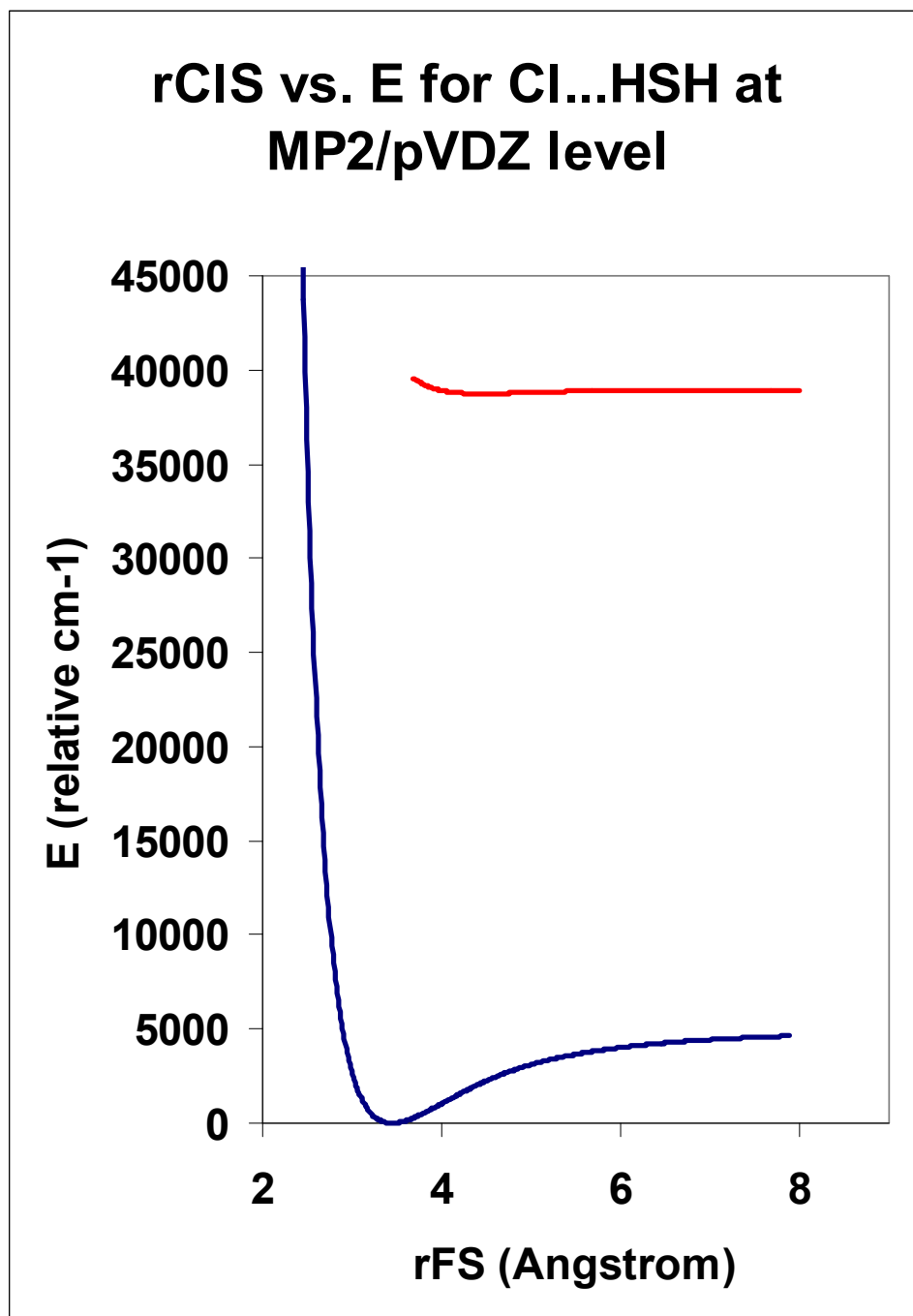


Figure 30 – One dimensional potential energy slices for the Cl...HSH cluster at the MP2/pVTZ level of theory

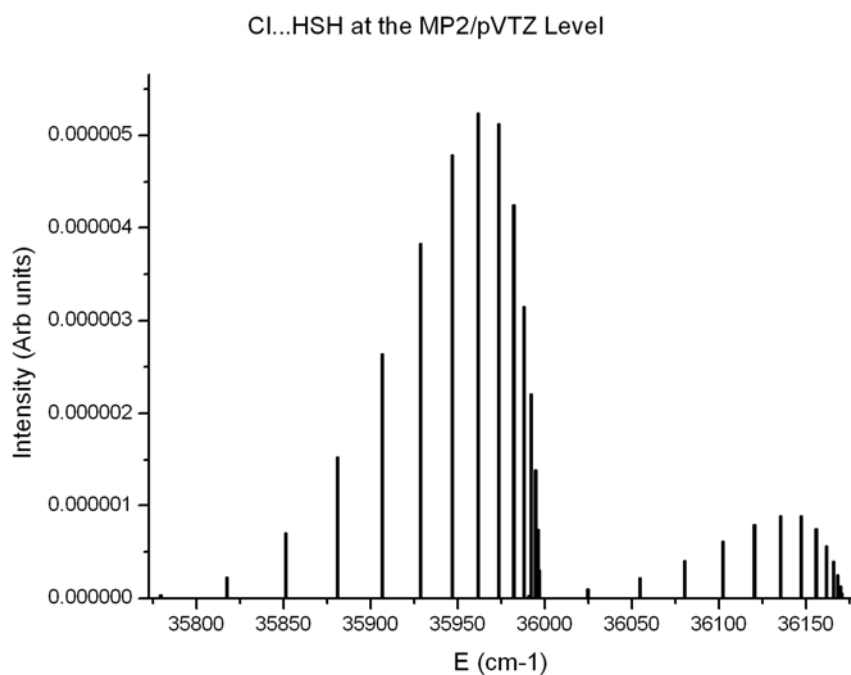
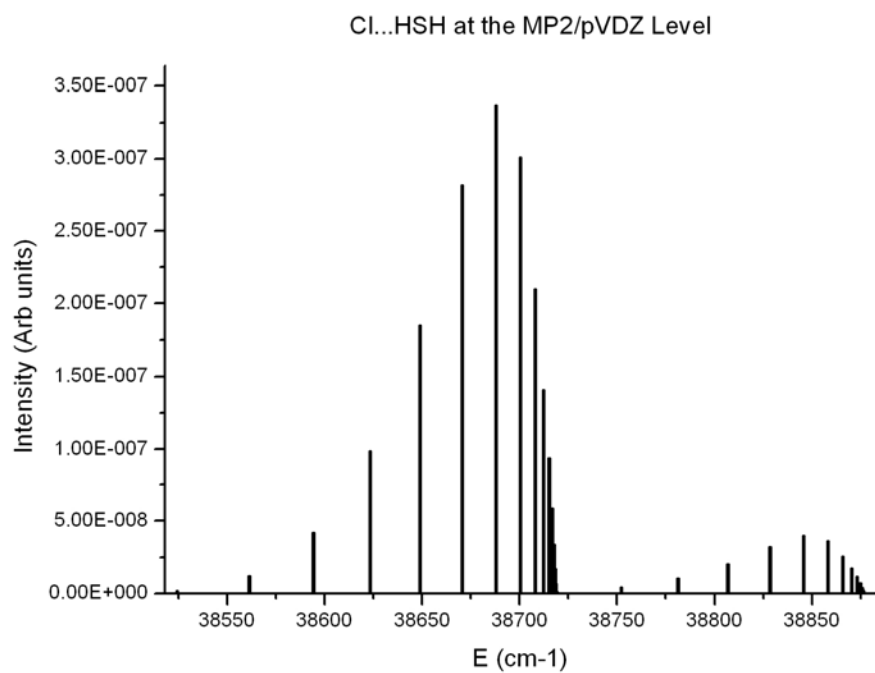


Figure 31 – Predicted photoelectron system for Cl...HSH using a) pVDZ and b) pVTZ basis sets

4 Conclusions and Future Work

The work detailed herein provides the essential work needed to construct a mass spectrometer with tandem anion photoelectron spectrometer. The ultra high levels of vacuum reached, combined with the success proved for each individual component in regards to obtaining test mass spectra is pleasing and promising. Upon successful verification that the mass spectrometric measurements are satisfactory, the optical assembly needs to be constructed and the mass gate/deceleration plates as well as photoelectron focusing apparatus need to be tested. Once a preliminary photoelectron spectrum can be obtained, the apparatus opens itself to a world of scientific endeavours. First and foremost among these is the halide hydrogen sulfide clusters, which can be directly compared to the predicted spectra reported herein.

While predicted spectra have been put forward in this work, they are by no means a full representation of the multidimensional hypersurfaces. In utilising the higher theory level four dimensional potential surfaces, better approximations to the full vibrational wavefunctions and Franck-Condon factors can be made, which obviously reflect better approximations to experimental spectra.

Future systems to be explored are near endless, yet a focus on the halide solvated systems through varying solvent molecules (e.g. NH_3 , PH_3 , etc.) seems an appealing target based on the lack of anion photoelectron studies to date compared to IR investigations.

5 Appendix

5.1 Anion Photoelectron Data Tables

Table A1: Solvation clusters studied using anion photoelectron spectroscopy

Cluster:	Notes:	Reference:
$\text{H}(\text{NH}_3)_1$	H^- spectrum solvated by NH_3 . Shift in agreement with theoretical results	18
$(\text{N}_2\text{O})_{1-2}^-$	Partial Vibrational Resolution	88
O^- , O_2^- , O_4^-	Confirm constructed spectrometer is operational	89
$(\text{NO})^-(\text{N}_2\text{O})_{1-2}$	NO^- signal shift; $\text{EA}_a(\text{N}_2\text{O})_2 > \text{EA}_a(\text{N}_2\text{O})_1$ as expected	90
$\text{H}(\text{NH}_3)_2$	Greater shift than $\text{H}(\text{NH}_3)_1$	91
$(\text{SO}_2)_2^-$	$\text{EA}_a(\text{SO}_2)_2^- > \text{EA}_a(\text{SO}_2)^-$ by 0.8eV	92
N_2O_2^-	Three species observed: $\text{O}_2^-(\text{N}_2)$; $\text{O}^-(\text{N}_2\text{O})$ and $\text{NO}^-(\text{NO})$	93
$(\text{CO}_2)_{n(2-13)}^-$	VDE discontinuities at $n=2$ and $n=6$ indicating structural change	94
$\Gamma(\text{CO}_2)_{1-13}$	Vibrational progression; 1 st solvation shell at $n(\text{CO}_2)=9$	95
$\Gamma(\text{H}_2\text{O})_n$	Initial disagreement with experiment suggesting central iodide, and theory reporting a surface iodide tethered to a water cluster. The latter was experimentally proven and attributed to the stability of the hydrogen bonding network	96
$\text{X}^-(\text{H}_2\text{O})_n$	Γ shell closure at $n=6$, halide on surface (see above). e^- BE increases with n . $\text{X} = \text{Br}, \text{I}$	97
$\text{NH}_2^-(\text{NH}_3)_{1,2}$	Vibrational progression owing to distorted ammonia	98
$\Gamma(\text{CH}_3\text{CN})_{1,2}$	Dipole bound anions; 2 dipole states for trimer	99
$\text{Br}^-(\text{CO}_2)_n$	Vibrational progression analogous to $\Gamma(\text{CO}_2)_n$	100
$\Gamma(\text{N}_2\text{O})_{1-12}$	Vibrational progression not observed – low quadrupole moment in N_2O (c.f. CO_2)	100
$\text{O}^-(\text{Ar})_{n(1-26,34)}$	Solvation shell at $n=12$; icosahedral structure. Capped icosahedron at $n=18$	101
$\text{O}^-(\text{Rg})$ $\text{O}^-(\text{N}_2)$	Electronic states assigned and dissociation energies calculated.	102
$\text{NO}^-(\text{Y})_n$	$\text{Y} = \text{N}_2\text{O} < \text{H}_2\text{S} < \text{NH}_3 < \text{H}_2\text{O} < \text{C}_2\text{H}_4(\text{OH})_2$ in terms of solvent stabilisation	103
$\text{NO}^-(\text{Rg})_n$	$\text{Rg} = \text{Ar}_{1-14}, \text{Kr}_1, \text{Xe}_{1-4}$ Stabilisation increase for larger Rg atoms owing to greater polarisability, or larger molecular framework to stabilise the excess electron	103

$(\text{NH}_3)_{n=41-1100}^-$	Largest anion = 4.3 nm, vertical detachment energy decreases linearly with $n^{-1/3}$	104
$(\text{H}_2\text{O})_n^-; (\text{D}_2\text{O})_n^-$	$n < 201$. Found lower VDE than previous experiment, suggesting unique conditions herein have produced surface, or dipole bound e^-	22
$(\text{MeOH})_{70-460}^-$	Two classes of VBE found: 2-2.5eV (internal e^-) and 0.2-0.5eV (surface e^-). VBEs both depend on $n^{-1/3}$ with nearly the same slopes	105
$(\text{H}_2\text{O})_{n=2-69}^-;$ $(\text{D}_2\text{O})_{2-23}^-$	Three classes of anion found, $n=2-16$: dipole-bound; $n=6-16$: intermediate states; $n=11-69$ bulk embryons (internalised e^-)	20

Table A2 – Select examples of dipole bound anions

Cluster:	Reference:
CH_3CN^-	23, 106
$(\text{H}_2\text{O})_2^-; (\text{H}_2\text{O})_2^- \text{Ar}_{n=1,2,3}; (\text{D}_2\text{O})_2^-; (\text{D}_2\text{O})_2^- \text{Ar}_{n=1,2,3}$	107
$\text{C}_3\text{H}_4\text{O}_3^-; \text{C}_3\text{H}_2\text{O}_3^-$ [prepared using Rydberg electron transfer)	108
$(\text{H}_2\text{O} \dots \text{NH}_3)^-$	27
(p,m-dinitrobenzene) $^-$	109
$(\text{HF})_2^-$	33
CH_3NO_2 ; both dipole- and valence-bound anion	110

Table A3 – Anionic metal and semiconductor clusters studied using anion photoelectron spectroscopy

Cluster:	Notes:	Reference:
Cu_n^-	Cu_{6-41} explored. 8, 20 and 40 correspond to closed shells, and have low EAs. Vibrational resolution for $n=2$	111,112
Al_n^-	$N=1-22$, energy dependence on cluster size and properties vary greatly from bulk spectra	113
Au_n^-	$n=1-233$; Shell closure at $n=58$ as predicted by ellipsoidal model $n=1-5$, vibrational resolution at $n=2$	111,114
Nb_n^-	$N=8$; very little geometry change; EA is $1.513 \pm 0.008\text{eV}$	115
$\text{NaK}^-; \text{KRb}^-;$ $\text{KCs}^-; \text{RbCs}^-;$ $\text{Na}_2\text{K}^-; \text{K}_2\text{Cs}^-$	Electronic transitions assigned as well as VDEs, EA_a s and dimer dissociation energies	116
Al_xP_y^-	($x,y < 5$), some states vibrationally resolved. Detailed assignments for $\text{AlP}_2^-; \text{Al}_2\text{P}^-; \text{and Al}_2\text{P}_2^-$	117
B_2N^-	Vibrationally resolved, some electronic assignment; EA =	118

	3.098±0.005eV	
C _n ⁻	N=5, vibrationally resolved with preliminary assignments	119
Sn _n ⁻	N=1-22, energy dependence on cluster size and properties vary greatly from bulk spectra	113
Pd _n ⁻	n=1-21, threshold energies increase smoothly with n. No even odd oscillation owing to localised d electrons	120
Ag _n ⁻	n=1-60 Shell closure at n=58 as predicted by ellipsoidal model. Even-odd oscillation: delocalised electron Fermi-gas within ellipsoidal deformed cluster n=1-10, vibrational resolution at n=2	111,121
Fe _n ⁻	N=2, simply interpreted as electron detachment from antibonding orbital	122
Na _n ⁻ ,	N=2-5. Both adiabatic electron affinity and vertical detachment energies reported.	123
Rb _n ⁻	n=2-7. Both adiabatic electron affinity and vertical detachment energies reported.	123
K _n ⁻	n=2-3. Both adiabatic electron affinity and vertical detachment energies reported.	123
Cs _n ⁻	n=2-3. Both adiabatic electron affinity and vertical detachment energies reported.	123
Co _n (benzene) _m	n=1, m=2: Adopts sandwich structure n>m=1: Cobalt cluster anions solvent stabilised by interaction with single benzene	124
Co _n (pyridine) _m	Ground state predicts Co insertion into C-H bond, but insertion barrier is too high – Co resides above pyridine plane.	125
GaX ₂ ⁻ , Ga ₂ X ⁻ , Ga ₂ X ₂ ⁻ , Ga ₂ X ₃ ⁻ (X=P, As)	Vibrational progression in all except Ga ₂ X ₂ ⁻ . EAs, term symbols and vibrational frequencies reported and compared to theory.	126
GaO ⁻ , GaO ₂ ⁻	EA of GaO given, vibrational frequency of GaO ⁻ and partial term allocation	127
Ga ₂ N ⁻	Ground state electronic transition assigned, EA obtained, and partial vibrational resolution observed	128
LiH ⁻	EA _a and dissociation values reported with electronic transitions	129
SeO ⁻	EA _a and dissociation energy reported	18
SiN ⁻	EA _a and dissociation energy reported. D ₀ quoted herein is calculated without discarding the dissociation energy of the neutral	130
ZnO ⁻	EA _a reported. Electronic states used to explain higher dissociation energy of the anion (unexpected as the excess electron is in an antibonding orbital)	39

5.2 TOF-PES Safety System

#rem

This is version 3 of the Safety System programming for the TOF PES
 Created by Duncan A. Wild and Rob LaMacchia 2008

Version History

V1: First attempt, with less detail in descriptions and also less subroutines

V2: Inserted a missing return statement

V3: Change to make the signal diodes flash, by introducing flash routine

 New goodtogo routine that ensures that the relays are not switched back on after a power outage

Here's a fairly detailed description of the inputs and outputs

Input Pin assignments

Analogue:

ADC0 = AIG1

ADC1 = AIG2

ADC2 = AIG3

ADC3 = APG1

ADC5 = APG2

ADC6 = APG3

ADC7 = not used

Digital:

input0 = hfs1 switch (Normally Closed = NC)

input1 = hfs2 switch (NC)

input2 = wfs1 (NC)

input3 = wfs2 (NC)

For ADC channels the range 0-255 equates to 0-12V DC, which is the output of the Edwards Active gauges

Which?	Pressure	Voltage	Digital	How?
AIG1trip	1x10 ⁻³	7.0	149	(7.0 X (255/12))
AIG2trip	1x10 ⁻⁶	4.0	85	(4.0 X (255/12))
AIG3trip	1x10 ⁻⁶	4.0	85	(4.0 X (255/12))
APG1trip	1x10 ⁻¹	5.0	107	(5.0 X (255/12))
APG2trip	1x10 ⁻¹	5.0	107	(5.0 X (255/12))
APG3trip	1x10 ⁻¹	5.0	107	(5.0 X (255/12))

Output pins assignments;

Port a

0 = Turbo1 (Single AC relay switching off power to Edwards EXT255)

1 = Turbo2 (Single DC relay, not a AC 240 Volts power shut off)

2 = Power 1 (Single AC relay supplying power to TOFplates, Electron, Nozzle, X-Y Def)

3 = Power 2 (Single AC relay supplying power to Detectors, Mass Gate, Ion Decel)
 4 = Pneumatic 1 (Single AC relay supplying power to 5/2 way solenoid valve)
 5 = Pneumatic 2 (Single AC relay supplying power to 5/2 way solenoid valve)
 6 = Diff pump 2 (Single AC relay supplying power to the Diffstak)
 7 = Diff pump 1 (Single AC relay supplying power to the Speedivac)

Port c

c0 = LED for AIG1 fail
 c1 = LED for AIG2 fail
 c2 = LED for AIG3 fail
 c3 = LED for APG1 fail
 c4 = 1 phase pumps power and 2 KF25 solenoid valves
 c5 = 3 phase E2M40 and 1 KF40 solenoid valve
 c6 = LED for APG2 fail
 c7 = LED for APG3 fail

#endrem

#rem

start by setting up outputs and defining some symbols

#endrem

```
let dirsc = %11111111      ' This sets the portc pins to be outputs
let pinsc = %00000000      ' This initialises all port c outputs to
1
let pins  = %00000000      ' This initialises all port a outputs to
1
symbol hfs1 = pin0         ' Set heater switch 1 to be input pin 0
symbol hfs2 = pin1         ' Set heater switch 2 to be input pin 1
symbol wfs1 = pin2         ' Set water flow switch 1 to be input pin
2
symbol wfs2 = pin3         ' Set water flow switch 2 to be input pin
3
symbol gtgs = pin4         ' Set the good to go switch to be input
pin 4
symbol AIG1trip = 149      ' The following are the trip values for
the analogue inputs
symbol AIG2trip = 85       ' See above for the origin of the values,
in terms of pressures & voltages
symbol AIG3trip = 85
symbol APG1trip = 107
symbol APG2trip = 107
symbol APG3trip = 107
symbol AIG1 = 0            ' Active Ion gauge 1 is ADC0
symbol AIG1Val = b2        ' It's value is set to variable b1
(byte2)
symbol AIG2 = 1            ' So on for the other two ion gauges
symbol AIG2Val = b3
symbol AIG3 = 2
symbol AIG3Val = b4
symbol APG1 = 3            ' Active Pirani gauge 1 is ADC3
```

```

symbol APG1Val = b5          ' It's value is set to variable b4
(byte5)
symbol APG2 = 5             ' So on for the other two Pirani gauges
symbol APG2Val = b6
symbol APG3 = 6
symbol APG3Val = b7
symbol diffk = bit1        ' Assigning symbol diffk to a binary
variable
symbol turbk = bit2        ' Assigning symbol turbk to a binary
variable
symbol AIG1fail = bit3     ' Assigning the AIG and APG's values to
binary variable
symbol AIG2fail = bit4
symbol AIG3fail = bit5
symbol APG1fail = bit6
symbol APG2fail = bit7
symbol APG3fail = bit8
diffk=1
turbk=1
AIG1fail=1
AIG2fail=1
AIG3fail=1
APG1fail=1
APG2fail=1
APG3fail=1

#rem
The good to go routine will ensure that if there is a power failure,
and the chip restarts
that the relays controlling the pumps etc will not restart

#endrem

goodtogo:

if gtgs = 0 then           ' If the gtg switch has not been
depressed, then all the LEDs will blink
let pinsc = %11001111
pause 500
let pinsc = %00000000
pause 500
else                       ' If the gtg switch has been depressed,
then turn all outputs on and head down to the main routine
let pinsc = %11111111     ' This initialises all port c outputs to
1
let pins = %11111111      ' This initialises all port a outputs to
1
goto main
endif

goto goodtogo

#rem
Here is the main loop of the program.

```

It will test if the diffk or turbk variables have been set to 0 which means that this part of the machine has been deactivated due to a fault

If diffk or turbk are = 1, then the programme will head to the subroutines that check the inputs for the two sides of the machine

On chip reset the turbk, diffk, and AxG#fail variables are all set to 1

```
#endrem
```

```
main:
```

```
if AIG1fail=0 OR APG1fail=0 then gosub flashdiff
```

```
if diffk = 1 then gosub diffcheck
```

```
if AIG2fail=0 OR AIG3fail=0 OR APG2fail=0 OR APG3fail=0 then gosub  
flashturb
```

```
if turbk = 1 then gosub turbcheck
```

```
#rem
```

The next part allows you to reset the system while it is running...
This is above the normal reset switch

This is important if for example one side of the machine goes down, and you want to be able to reset it without having to shut down the other side!

```
#endrem
```

```
if gtgs = 0 then          ' If the gtg switch has not been  
depressed, then nothing will happen  
else                      ' If the gtg switch has been depressed,  
then turn all outputs on again  
let pinsc = %11111111    ' This initialises all port c outputs to  
1  
let pins = %11111111     ' This initialises all port a outputs to  
1  
turbk=1  
diffk=1  
AIG1fail=1              ' The next six will reset the AxGxfail  
variables to 1  
AIG2fail=1  
AIG3fail=1  
APG1fail=1  
APG2fail=1  
APG3fail=1  
endif
```

```
goto main
```

```
#rem
```

Next are the checking sub routines that will read the inputs etc.

```
#endrem
```

```

diffcheck:

#rem
This will check the inputs from the diffusion pumps
#endrem

readadc AIG1,AIG1Val      ' Check the ion gauge voltage
readadc APG1,APG1Val      ' Check the pirani gauge voltage

if AIG1Val>AIG1trip then low portc 0 AIG1fail=0 ' Light up the fault
diode of AIG1

endif

if APG1Val>APG1trip then low portc 3 APG1fail=0 ' Light up the fault
diode of APG1

endif

if AIG1Val>AIG1trip OR APG1Val>APG1trip OR hfs1 = 0 OR wfs1 = 0 then
gosub diffoff ' if the ADC values are too high, or the heater/flow
switches are

        ' tripped then go to the diff off subroutine

return

turbcheck:

#rem
This sub routine will check the inputs from the turbo pumps
#endrem

readadc AIG2,AIG2Val      ' Check Ion gauge 2
readadc AIG3,AIG3Val      ' Check Ion gauge 3
readadc APG2,APG2Val      ' Check Pirani gauge 2
readadc APG3,APG3Val      ' Check Pirani gauge 3

if AIG2Val>AIG2trip then low portc 1 AIG2fail=0 ' Light up the fault
diode of AIG2

endif

if AIG3Val>AIG3trip then low portc 2 AIG3fail=0 ' Light up the fault
diode of AIG3

endif

if APG2Val>APG2trip then low portc 6 APG2fail=0 ' Light up the fault
diode of APG2

endif

if APG3Val>APG3trip then low portc 7 APG3fail=0 ' Light up the fault
diode of APG3

endif

```



```

if AIG2Val>AIG2trip OR AIG3Val>AIG3trip OR APG2Val>APG2trip OR
APG3Val>APG3trip OR hfs2 = 0 OR wfs2 = 0 then gosub turboff

return

diffoff:

#rem
The following is the diffoff subroutine
Actions: Turn off the diffusion pumps, close the butterfly valves,
after 30 mins shut down the E2M40 and it's solenoid valve
This routine will also call on the turbcheck subroutine every second to
ensure that there is nothing wrong with the turbo end
#endrem

diffk = 0
w12 = 0

if turbk = 0 AND diffk = 0 then gosub alloff

low 7          ' This will make the output pins low
hence turn off breakers
low 6          ' for the diffusion pumps, the solenoid
gas valves that drive
low 5          ' the butterfly valves and also the power
supplies for the TOF
low 4          ' plates, X-Y deflection, Gas nozzle
driver and electron filaments
low 3

do             ' This loop will wait 15 mins before
turning off E2M40
gosub turbcheck      ' This part ensures that the turbos are
still monitored
gosub flashdiff      ' Go to the flashdiff subroutine which
will make the failed input's LED flash
inc w12
loop while w12 < 30   ' During testing this is set to 60
seconds, change to 1800 when completed testing

low portc 5        ' This will turn off E2M40 pump, and it's
solenoid valve

return

turboff:

#rem
The following is the Turbo off sub routine
Actions: Turn off turbo pump supplies and electronics
(De1,De2,MassGate,IonDecel,Einzelland2)
and after 30 mins turn off the small rotary pumps and close solenoid
valves
This routine will also call on the diffcheck routine every second
#endrem

```

```

turbk=0          ' This sets the turbk value to 0, so when
the programme returns to main, it doesn't bother checking the turbo
inputs
w13=0           ' anymore

low 2          ' This will turn off the breakers for the
turbo side
low 1
low 0

if turbk=0 AND diffk=0 then gosub alloff

do             ' This loop will wait 15 mins before
turning off E2M40
gosub diffcheck ' This part ensures that the diffusion
pumps are still monitored
gosub flashturb ' Go to the flashturb subroutine which
will make the failed input's LED flash
inc w13
loop while w13 < 30 ' During testing this is set to 60
seconds, change to 1800 when completed testing

low portc 4    ' This will turn off the small rotary
pumps, and their solenoid valves

return         ' NEW in v2, this return was missing from
v1 and may be the reason that the programme switched off all outputs

#rem
The following is the alloff routine

Actions: Switch off all power breakers, wait half an hour and switch
off rotary pumps and associated solenoid
#endrem

alloff:

w11=0
low 7          ' This will turn off the breakers for the
diff pump side 7-->3
low 6
low 5
low 4
low 3
low 2          ' This will turn off the breakers for the
turbo side 2-->0
low 1
low 0

do             ' This will wait 30 mins before switching
off rotary pumps
gosub flashdiff ' Go to the flashdiff subroutine which
will make the failed input's LED flash
gosub flashturb ' Go to the flashturb subroutine which
will make the failed input's LED flash
inc w11

```

```

loop while w11 < 60          ' During testing this is set to 60
seconds, change to 1800 when completed testing

low portc 5                 ' This turns off the E2M40 and associated
solenoid valve
low portc 4                 ' This turns off the small rotary pumps
and associated solenoid valves

return                      ' This will return to the main program,
which will just loop until a reset!

#rem
The following two routines will make the output LEDs flash showing a
failure on the ADC channels
#endrem

flashdiff:                  ' This is the flashdiff subroutine. It
will check the status of the AxG#fail bit variables
                            ' and then make the corresponding LED

flash
if AIG1fail=0 then
low portc 0
pause 500
high portc 0
pause 500
else
endif

if APG1fail=0 then
low portc 3
pause 500
high portc 3
pause 500
else
endif

return

flashturb:                  ' This is the flashturb subroutine. It
will check the status of the AxG#fail bit variables
                            ' and then make the corresponding LED

flash
if AIG2fail=0 then
low portc 1
pause 500
high portc 1
pause 500
else
endif

if AIG3fail=0 then
low portc 2
pause 500
high portc 2
pause 500
else

```

```

endif

if APG2fail=0 then
low portc 6
pause 500
high portc 6
pause 500
else
endif

if APG3fail=0 then
low portc 7
pause 500
high portc 7
pause 500
else
endif

return

```

5.3 UNIX *dataextraction.sh* Script

```

#!/usr/bin/sh
#This is V1 of the script to extract 2 dimensional data from a 4
dimensional set.
#It is highly specific, and requires heavy code alteration for
differnet jobs

echo "What is the name of the output file? "
read name
echo "Please enter the first dimension to be constant: "
read var1
echo "Please enter the second dimension to be constant (not $var1): "
read var2
echo "Please enter the equilibrium value for one of the constants: "
read num1
echo "And the second one (not $num1): "
read num2

grep -w $num1 $name > TEMP;
grep -w $num2 TEMP > $var1$var2.txt;
echo "Check" $var1$var2".txt for results";

```

6 References:

- (1) Simons, J. J. *Phys. Chem. A* **2008**, *112*, 6401.
- (2) Stillinger, F. H; Rahman, A. *J. Chem. Phys* **1978**, *68*, 666.
- (3) Neumark, D. M. *Phys. Chem. Chem. Phys.* **2005**, *7*, 433.
- (4) Atkins, P.; DePaula, J. Atkins' Physical Chemistry; Oxford Press: Oxford, 2006.
- (5) Arshadi, M.; Kabarle, P. *J. Phys. Chem.* **1970**, *74*, 1483.
- (6) Kebarle, P.; Arshadi, M.; Scarborough, J. *J. Chem. Phys.* **1968**, *49*, 817.
- (7) Keesee, R. G.; Lee, N.; Castleman, A. W. *J. Am. Chem. Soc.* **1979**, *101*, 2599.
- (8) Keesee, R. G.; Lee, N.; Castleman, A. W. *J. Geophys. Res.* **1979**, *84*, 3719.
- (9) Lee, N.; Keesee, R. G.; Castleman, A. W. *J. Chem. Phys.* **1980**, *72*, 1089.
- (10) Payzant, J. D.; Yamdagni, R.; Kebarle, P. *Can. J. Chem.* **1971**, *49*, 3308.
- (11) Yamdagni, R.; Kebarle, P. *J. Am. Chem. Soc.* **1971**, *93*, 7139.
- (12) Yamdagni, R.; Kebarle, P. *Can. J. Chem.* **1974**, *52*, 2449.
- (13) Davidson, J. A.; Fehsenfeld, F. C.; Howard, C. J. *Int. J. Chem. Kinet.* **1977**, *9*, 17.
- (14) Riveros, J. M. *Adv. Mass Spectrom.* **1975**, *33*, 362.
- (15) Depaz, M.; Giardini, A. G.; Friedman, L. *J. Chem. Phys.* **1970**, *52*, 687.
- (16) Castleman, A. W.; Bowen, K. H. *J. Phys Chem* **1996**, *100*, 12911.
- (17) Note: For Figure 3, this approximation would not be valid
- (18) Coe J. V; Snodgrass J. T; Freidhoff, C. B.; McHugh K. M; Bowen, K. H. *J. Chem. Phys.* **1985**, *83*, 3169.
- (19) Barnett, R. N.; Landman, U.; Cleveland, C. L.; Jortner, J. *Phys. Rev. Lett.* **1987**, *59*, 811.
- (20) Coe J. V; Williams S. M; Bowen, K. H. *Int. Rev. Phys. Chem.* **2008**, *27*, 27.

- (21) Haberland, H.; Schindler, H.-G.; Worsnop, D. R. *Ber. Bunsen-Ges. Phys. Chem.* **1984**, *88*, 270.
- (22) Verlet J. R. R; Bragg A. E; Kammrath A; Cheshnovsky O; Neumark, D. M. *Science* **2005**, *307*, 93.
- (23) Compton, R. N.; Reinhardt, P. W.; Cooper, C. D. *J. Chem. Phys.* **1978**, *91*, 4890.
- (24) Antoniewicz, P. R.; Bennett, G. T.; Thompson, J. C. *J. Chem. Phys.* **1982**, *77*, 4573.
- (25) Kestner, N. R.; Jortner, J. *J. Phys. Chem.* **1984**, *88*, 3818.
- (26) Wallqvist, A.; Thirumalai, D.; Berne, B. J. *J. Chem. Phys.* **1986**, *85*, 1583.
- (27) Desfrancois, C.; Baillon, B.; Schermann, J. P.; Arnold, S. T.; Hendricks, J. H. *Phys. Rev. Lett.* **1994**, *72*, 48.
- (28) A 'notes' section is not detailed as the Dipole-Bound anions all tend to display similar properties as expressed in text
- (29) Berdys, J.; Anusiewicz, I.; Skurski, P.; Simons, J. *J. Am. Chem. Soc.* **2004**, *2004*, 6441.
- (30) Dabkowska, I.; Rak, J.; Gutowski, M.; Nilles, J. M.; Stokes, S. T. *J. Chem. Phys.* **2004**, *120*, 6064.
- (31) Gutowski, M.; Dabkowska, I.; Rak, J.; Xu, S.-J.; Nilles, J. M.; Radisic, D. *Eur. Phys. J. D* **2002**, *20*, 431.
- (32) Haranczyk, M.; Gutowski, M.; Li, X. *J. Phys. Chem. B. Lett.* **2007**, *111*, 14073.
- (33) Hendricks, J. H.; de Clercq, H. L.; Lyapustina, S. A.; Bowen, K. H. *J. Chem. Phys.* **1997**, *107*, 2962.
- (34) Hendricks, J. H.; Lyapustina, S. A.; de Clercq, H. L. *J. Chem. Phys.* **1998**, *108*, 8.

- (35) Hendricks, J. H.; Lyapustina, S. A.; de Clercq, H. L.; Snodgrass, J. T.; Bowen, K. *H. J. Chem. Phys.* **1996**, *104*, 7788.
- (36) Mazurkiewics, K.; Haranczyk, M.; Storniak, P.; Gutowski, M.; Rak, J.; Radisic, D.; Eustis, S. N.; Wang, D. *Chem. Phys.* **2007**, *342*, 215.
- (37) Parsons, B. F.; Sheehan, S. M.; Yen, T. A.; Neumark, D.; Wehres, N. *Phys. Chem. Chem. Phys.* **2007**, *9*, 3291.
- (38) Schiedt, S.; Weinkauff, R.; Neumark, D. M. *Chem. Phys.* **1998**, *239*, 511.
- (39) Fancher, C.; de Clercq, H. L.; Thomas, O. C.; Robinson, D. W. *J. Chem. Phys.* **1998**, *109*, 8426.
- (40) Basuchlicher, C. W.; Langhoff, S. R. *Chem. Phys. Lett.* **1986**, *126*, 163.
- (41) Watson, C. W.; Partridge, H. *J. Chem. Phys.* **1998**, *109*, 8430.
- (42) Brewer, L.; Mastick, D. F. *J. Chem. Phys.* **1951**, *19*, 834.
- (43) Brewer, L. *Chem. Rev.* **1953**, *52*, 1.
- (44) Anthrop, D. F.; Searcy, A. W. *J. Phys. Chem.* **1964**, *68*, 2335.
- (45) Wicke, B. G. *J. Chem. Phys.* **1983**, *78*, 6036.
- (46) Watson, L. R.; Thiem, T. L.; Dressler, R. A.; Salter, R. H.; Murad, E. *J. Phys. Chem.* **1993**, *97*, 5577.
- (47) Thomas, O. C.; Zheng, W.-J. *J. Chem. Phys.* **2001**, *114*, 5514.
- (48) Zheng, W.-J.; Thomas, O. C.; Lippa, T. P.; Xu, S.-J. *J. Chem. Phys.* **2006**, *124*, 144304.
- (49) Knight, W. D.; Clemenger, W. A.; de Heer, W. A.; Saunders, W. A.; Chou, M. Y.; Cohen, M. L. *Phys Rev. Lett* **1984**, *52*, 2141.
- (50) Khanna, S. N.; Jena, P. *Chem. Phys. Lett.* **1994**, *219*, 479.

- (51) Leuchtner, R. E.; Harms, A. C.; Castleman, A. W. *J. Chem. Phys.* **1989**, *91*, 2753.
- (52) Li, X.; Wu, H.; Wang, X.-B.; Wang, L.-S. *Phys. Rev. Lett.* **1998**, *81*, 1909.
- (53) Hoshino, K.; Watanabe, K.; Konishi, Y.; Taguwa, T.; Nakajima, A.; Kaya, K. *Chem. Phys. Lett.* **1994**, *231*, 499.
- (54) Thomas, O. C.; Zheng, W.-J.; Lippa, T. P.; Xu, S.-J.; Lyapustina, S. A.; Bowen, K. H. *J. Chem. Phys.* **2001**, *114*, 9895.
- (55) Wang, L. S.; Wang, B. X. *J. Phys. Chem. A* **2000**, *104*, 1978
- (56) Wang L. S. *J. Phys. Chem. A* **2000**, *104*, 1978.
- (57) Johnson, M. A.; Robertson, W. H. *Annu. Rev. Phys. Chem.* **2003**, *54*, 173.
- (58) Wild, D. A.; Lenzer, T. *Phys. Chem. Chem. Phys.* **2007**, *9*, 5776.
- (59) Wild, D. A.; Lenzer, T. *Phys. Chem. Chem. Phys.* **2005**, *7*, 3793.
- (60) Ayotte, P.; Weddle, G.; Kim, J.; Kelley, J.; Johnson, M. *J. Phys. Chem.* **1999**, *103*, 443.
- (61) Wei, S.; Shi, Z. *J. Chem. Phys.* **1991**, *94*, 3268.
- (62) Jorgensen, W.; Severance, D. *J. Chem. Phys.* **1993**, *99*, 4233.
- (63) Coe, J. V.; Snodgrass, J. T.; Freidhoff, C. B.; McHugh, K. M.; Bowen, K. H. *J. Chem. Phys.* **1986**, *84*, 618.
- (64) Buck, U.; Ettischer, I.; Melzer, M.; Buch, V.; Sadlej, J. *Phys. Rev. Lett.* **1998**, *80*, 2578.
- (65) Ayotte, P.; Weddle, G. H.; Kim, J.; Johnson, M. A. *Chem. Phys.* **1998**, *239*, 485.
- (66) Bailey, C. G.; Dessent, C. E. H.; Johnson, M. A.; Bowen, K. H. *J. Chem. Phys.* **1996**, *104*, 6976.
- (67) Okumura, M.; Yeh, L. I.; Myers, J. D.; Lee, Y. T. *J. Chem. Phys.* **1986**, *85*, 2328.

- (68) Huisken, F.; Kaloudis, M.; Kulcke, A. *J. Chem. Phys.* **1996**, *104*, 17.
- (69) Ayotte, P.; Kelley, J.; Nielsen, S.; Johnson, M. *Chem. Phys Lett.* **2000**, *316*, 455.
- (70) Cheshnovsky, O.; Giniger, R.; Markovich, G.; Makov, G.; Nitzan, A.; Jortner, J. *J. Chem. Phys.* **1995**, *92*, 397.
- (71) Moore, J. H.; Davis, C. C.; Coplan, M. A. *Building Scientific Apparatus*; Addison-Wesley: Sydney, 1997.
- (72) Keesee, R. G.; Castleman, A. W. *J. Phys. Chem. Ref. Data*, **1986**, *15*, 1011.
- (73) Gibson, D.; Reilly, M. Pulse Valve Poppet Replacement Instructions; Parker Hannison: New Jersey, 2006.
- (74) Based on previous experience Dr. Wild has had with halide molecular beam systems
- (75) Wild, D.A.; Unpublished result for $F^-(NH_3)$
- (76) Wiley, W. C.; McLaren, I. H. *Rev. Sci. Instr.* **1955**, *26*, 1150.
- (77) Cheshnovsky, O.; Yang, S. H.; Pettiette, C. L.; Craycraft, M. J. *Rev. Sci. Instrum.* **1987**, *58*, 2131.
- (78) Many thanks to Allan McKinley
- (79) Appreciation extends to Professor Jim Williams from the School of Physics, UWA.
- (80) Xantheas, S. S.; Dunning, Jr. T.H.; *J. Phys. Chem.* **1994**, *98*, 13489.
- (81) M. J. Frisch, G. W. T., H.B. Schlegel, G. E. Scuseria, M. A.; Robb, J. R. C., J. A. Montgomery, Jr., T. Vreven, K. N.; Kudin, J. C. B., J. M. Millam, S. S. Iyengar, J. Tomasi, V.; Barone, B. M., M. Cossi, G. Scalmani, N. Rega, G. A.; Petersson, H. N., M. Hada, M. Ehara, K. Toyota, R.; Fukuda, J. H., M. Ishida, T. Nakajima, Y. Honda, O.;

Kitao, H. N., M. Klene, X. Li, J. E. Knox, H. P. Hratchian, J.; B. Cross, V. B., C. Adamo, J. Jaramillo, R. Gomperts, R. E.; Stratmann, O. Y., A. J. Austin, R. Cammi, C. Pomelli, J.; Ochterski, P. Y. A., K. Morokuma, G. A. Voth, P. Salvador, J.; J. Dannenberg, V. G. Z., S. Dapprich, A. D. Daniels, M.; C. Strain, O. F., D. K. Malick, A. D. Rabuck, K. Raghavachari,; J. B. Foresman, J. V. O., Q. Cui, A. G. Baboul, S.; Clifford, J. C., B. B. Stefanov, G. Liu, A. Liashenko, P.; Piskorz, I. K., R. L. Martin, D. J. Fox, T. Keith, M. A.; Al-Laham, C. Y. P., A. Nanayakkara, M. Challacombe, P. M.; W. Gill, B. G. J., W. Chen, M. W. Wong, C. Gonzalez and; J. A. Pople. GAUSSIAN 98 (Revision B.04), Gaussian, Inc., Wallingford, CT, 98.

(82) Suggested by A/Prof Graham Chandler

(83) Del Bene, J. E.; Mettee, H. D.; Frisch, M. J.; Luke, B. T.; Pople, J. A. *J. Phys. Chem.* **1983**, *87*, 3279.

(84) Reed, A. D.; Curtiss, L. A.; Weinhold, F. *Chem. Rev.* **1988**, *88*, 899.

(85) Szabo, A. *Modern Quantum Chemistry: Introduction to Advanced Electronic Structure Theory*; MacMillan: New York, 1982.

(86) LeRoy, R. J.; LEVEL University of Waterloo, Chem. Phys. Research, Report No. CP-655, 2002., 2005.

(87) Maris, A.; Favero, L. B.; Danieli, R.; Favero, F. G.; Caminati, W. *J. Chem. Phys.* **2000**, *113*, 8567.

(88) Coe, J. V.; Snodgrass, J. T.; Freidhoff, C. B.; McHugh, K. M.; Bowen, K. H. *Chem. Phys. Lett.* **1986**, *124*, 274.

(89) Posey, L. A.; Deluca, M. J.; Johnson, M. A. *Chem. Phys. Lett.* **1986**, *131*, 170.

- (90) Coe, J. V.; Snodgrass, J. T.; Freidhoff, C. B.; McHugh, K. M.; Bowen, K. H. *J. Chem. Phys.* **1987**, *87*, 4302.
- (91) Snodgrass, J. T.; Coe, J. V.; Freidhoff, C. B.; McHugh, K. M.; Bowen, K. H. *Faraday Discuss. Chem. Soc.* **1988**, *86*.
- (92) Snodgrass, J. T.; Coe, J. V.; Freidhoff, C. B.; McHugh, K. M.; Bowen, K. H. *J. Chem. Phys.* **1988**, *88* 8014.
- (93) Posey, L. A.; Johnson, M. A. *J. Chem. Phys.* **1988**, *88* 5383.
- (94) Deluca, M. J.; Liu, B.; Johnson, M. A. *J. Chem. Phys.* **1988**, *88*, 5857.
- (95) Arnold D. W.; Bradforth S. E.; Kim E. H.; D, N. *J. Chem. Phys.* **1992**, *97*.
- (96) Markovich, G.; Pollack, S.; Giniger, R.; Cheshnovsky, O. *Z. Phys. D* **1993**, *26*, 98.
- (97) Markovich, G.; Pollack, S.; Giniger, R.; Cheshnovsky, O. *J. Chem. Phys.* **1994**, *101*, 9344.
- (98) Snodgrass, J. T.; Coe, J. V.; Freidhoff, C. B.; McHugh, K. M.; Bowen, K. H. *J. Phys. Chem.* **1995**, *99*, 9675.
- (99) Dessent, C. E. H.; Bailey, C. G.; Johnson, M. A. *J. Chem. Phys.* **1995**, *103*, 2006.
- (100) Arnold, D. W.; Bradforth, S. E.; Kim, E. H.; Neumark, D. M. *J. Chem. Phys.* **1995**, *102*, 3510.
- (101) Arnold, S. T.; Hendricks, J. H.; Bowen, K. H. *J. Chem. Phys.* **1995**, *102*, 39.
- (102) de Clercq, H. L.; Hendricks, J. H.; Bowen, K. H. *J. Chem. Phys.* **2002**, *117*, 2619.
- (103) Hendricks, J. H.; de Clercq, H. L.; Freidhoff, C. B.; Arnold, S. T.; Eaton, J. G.; Fancher, C.; Lyapustina, S. A.; Snodgrass, J. T.; Bowen, K. H. *J. Chem. Phys.* **2002**, *116*, 7926.

- (104) Sarkas, H. W.; Arnold, S. T.; Eaton, J. G.; Lee, G. H.; Bowen, K. H. *J. Chem. Phys.* **2002**, *116*, 5731.
- (105) Kammrath, A.; Verlet, J. R. R.; Griffin, G. B.; Neumark, D. M. *J. Chem. Phys.* **2006**, *125*, 76101.
- (106) Bailey, C. G.; Dessent, C. E. H.; Johnson, M. A.; Bowen, K. H. *J. Chem. Phys.* **1996**, *104*, 6976.
- (107) Lee, G. H.; Arnold, S. T.; Eaton, J. G.; Bowen, K. H. *Chem. Phys. Lett.* **2000**, *321*, 333.
- (108) Hammer, N. I.; Hinde, R. J.; Compton, R. N.; Diri, K.; Jordan, K. D.; Radisic, D.; Stokes, S. T.; Bowen, K. H. *J. Chem. Phys.* **2004**, *120*, 685.
- (109) Desfrancois, C.; Periquet, V.; Lyapustina, S. A.; Lippa, T. P.; Robinson, D. W.; Bowen, K. H.; Nonake, H.; Compton, R. N. *J. Chem. Phys.* **1999**, *111*, 4569.
- (110) Compton, R. N.; Carman Jr., H. S.; Desfrancois, C.; Abdoul-Carmine, H.; Schermann, J. P.; Hendricks, J. H.; Lyapustina, S. A.; Bowen, K. H. *J. Chem. Phys.* **1996**, *105*, 3472.
- (111) Ho, J.; Erving, K. M.; Lineberger, W. C. *J. Chem. Phys.* **1990**, *93*, 6987.
- (112) Pettiette, C. L.; Yang, S. H.; Craycraft, M. J.; Conceicao, J.; Laaksonen, R. T.; Cheshnovsky, O.; Smalley, R. E. *J. Chem. Phys.* **1988**, *88*, 5377.
- (113) Gantefor, G. F.; Gausa, M.; Meiwes-Broer, K. H.; Lutz, H. O. *Faraday Discuss. Chem. Soc.* **1988**, *86*, 197.
- (114) Taylor, T. R.; Asmis, K. R.; Xu, C.; Neumark, D. M. *Chem. Phys. Lett.* **1998**, *297*, 133.
- (115) Marcy, T. P.; Leopold, D. G. *Int. J. Mass Spect.* **2000**, *195*, 653.

- (116) Eaton, J. G.; Sarkas, H. W.; Arnold, S. T.; McHugh, K. M.; Bowen, K. H. *Chem. Phys. Lett.* **1992**, *193*, 141.
- (117) Gomez, H.; Taylor, T. R.; Neumark, D. M. *J. Phys. Chem. A* **2001**, *105*, 6886.
- (118) Asmis, K. R.; Taylor, T. R.; Neumark, D. M. *J. Chem. Phys.* **1999**, *111*, 8838.
- (119) Kitsopoulos, T. N.; Chick, C. J.; Zhoo, Y.; Neumark, D. M. *J. Chem. Phys.* **1991**, *95*, 1941.
- (120) Gantefor, G. F.; Gausa, M.; Meiwes-Broer, K. H.; Lutz, H. O. *J. Chem. Soc. Faraday Trans.* **1990**, *86*, 2483.
- (121) Taylor, K. J.; Pettiette-Hall, C. L.; Cheshnovsky, O.; Smalley R.E. *J. Chem. Phys.* **1992**, *96*, 3319.
- (122) Leopold, D. G.; Almlöf, J.; Lineberger, W. C.; Taylor, P. R. *J. Chem. Phys.* **1988**, *88*, 3780.
- (123) McHugh, K. M.; Eaton, J. G.; Lee, G. H.; Sarkas, H. W.; Kidder, L. H.; Snodgrass, J. T.; Manaa, M. R.; Bowen, K. H.; *J. Chem. Phys.* **1989**, *91*, 3792.
- (124) Gerhards, M.; Thomas, O. C.; Nilles, J. M.; Zheng, W.-J.; Bowen, K. H. *J. Chem. Phys.* **2002**, *116*, 10247.
- (125) Edmonds, B. D.; Kandalam, A. K.; Khanna, S. N.; Li, X.; Grubisic, A.; Khanna, I.; Bowen, K. H. *J. Chem. Phys.* **2006**, *124*, 74316.
- (126) Taylor, T. R.; Gomez, H.; Asmis, K. R.; Neumark, D. M. *J. Chem. Phys.* **2001**, *115*, 4620.
- (127) Meloni, G.; Sheehan, S. M.; Neumark, D. M. *J. Chem. Phys.* **2005**, *122*, 74317.
- (128) Sheehan S. M; Meloni G; Parsons B. F; Wehres N; Neumark, D. M. *J. Chem. Phys.* **2006**, *124*, 64303.

(129) Sarkas H. W; Hendricks J. H; Arnold S. T; Bowen, K. H. *J. Chem. Phys.* **1994**, *100*, 1884.

(130) Meloni G; Sheehan S. M; Ferguson M. J; Neumark D. M. *J. Phys. Chem. A* **2004**, *108*, 9750.